

**Three-dimensional Density Structure of the Earth:  
Limits to Astrophysical and Seismological Approaches**

by

Chaincy Kuo

B.A. (University of California at Berkeley) 1991

A dissertation submitted in partial satisfaction of the  
requirements for the degree of  
Doctor of Philosophy

in

Geophysics

in the

GRADUATE DIVISION

of the

UNIVERSITY of CALIFORNIA at BERKELEY

Committee in charge:

Professor Barbara Romanowicz, Chair  
Professor Raymond Jeanloz  
Professor Gilbert Shapiro

1999

The dissertation of Chaincy Kuo is approved:

---

Chair

Date

---

Date

---

Date

University of California at Berkeley

1999

## **Abstract**

### **Three-dimensional Density Structure of the Earth: Limits to Astrophysical and Seismological Approaches**

by

**Chaincy Kuo**

**Doctor of Philosophy in Geophysics**

**University of California at Berkeley**

**Professor Barbara Romanowicz, Chair**

Large scale density structure of the Earth's interior is investigated. Two widely differing approaches to retrieving density structure are examined: through astrophysical and geophysical means. The theoretical framework of measuring the Earth's radial density profile from very high energy (TeV) neutrino attenuation measurements is presented. Celestial objects such as active galaxies and quasars are assumed to be sources of very high energy neutrinos, and theoretical fluxes are calculated. Using detector parameters, attenuation values of the very high neutrinos after they have traversed through the Earth are estimated. On the order of two decades' worth of measurements from the proposed neutrino sources would be required for a statistically significant observation of the Earth's core, given the current neutrino detector capabilities. Next, the more traditional approach of seismology is utilized. Earth normal mode theory is

presented and the linearization of the seismogram relation to Earth structure is formulated, including corrections for mode coupling. Inversions of normal mode spectra directly for Earth structure are performed. Earth models, parameterized in terms of seismic velocity and density perturbations and topography on the core-mantle boundary, are presented. Comparisons of the seismic velocity models with those derived from body wave studies show good agreement. The core-mantle boundary topography pattern indicates correspondence with PcP and PKPab analyses of undulations at this boundary. The resolution for density perturbations is analyzed carefully in the last chapter. Contamination effects between seismic velocity model parameters and density model parameters are examined by using resolution matrices computed from data kernels, and by inverting synthetic spectra computed from realistic input Earth models. These resolution tests indicate that density structure retrieved from normal mode data are not reliable, to date.

Approved:

---

Barbara Romanowicz, Chair

Date



In loving memory of my uncles,  
John S. Tsang and Paul J. Tsang,  
who celebrate this with me in my heart.

# Contents

## List of Figures

## List of Tables

## Acknowledgements

Barbara Romanowicz's expertise and guidance were essential for the Earth free oscillation studies, which comprise the bulk of this dissertation. Much of my code for this work has foundations from programs written by Xiang-Dong Li. Joseph Durek also provided me with guidance in the earlier stages of the normal mode research.

I extend my gratitude to Gil Shapiro and Raymond Jeanloz for serving on my dissertation committee.

Without Hank Crawford's continued faith in me since I was an undergraduate researcher under his supervision, my desire to engage in scientific research would not have been fulfilled. I am most grateful to him and Gil Shapiro for introducing me to and guiding me in high energy particle astrophysics, and for sending me to the work in the harsh environment of the experimental site for DUMAND ;-). The neutrino study resulted in a published article, and I'd like to thank the publisher, Elsevier Science, and my co-authors: Hank Crawford, Raymond Jeanloz, Barbara Romanowicz, Gil Shapiro and Lynn Stevenson. As co-authors, we thank Ralph Becker-Szendy, Mark Bukowski, John Learned, John Mitchell, and Victor Stenger for helpful discussions.

The particle physicists on the '5th' floor of Building 50, Lawrence Berkeley Lab, gave me valuable perspectives on my geophysics research by scrutinizing my results: Jack Engelage, Brian Fujikawa, Leo Greiner, Eleanor Judd, Maria

Perillo-Isaac, Collin Okada, Mou Roy, and Gil Shapiro. I thank Carl Penny-packer for first hiring me into my first research position as an undergraduate summer intern for the Center for Particle Astrophysics in 1989. I would never have made it this far without the support and friendships of Hank, Jack, and Leo, which they have been giving me since I began working with them that summer.

The course of my graduate studies at U.C. Berkeley was not devoid of difficult experiences. My warmest heartfelt thanks to my friends who were there for me, especially Patty Seifert, Matteo Melani, Jennie Cullen, Bettina Spillar, Bruno Kaelin, my parents and my brother Augie.

I am also extremely grateful to my friends with whom I could find distraction from science. Many stories were shared with Patty, and Maria P.-I. I will never forget mountain biking, climbing, and wind-surfing with Patty, Jennifer M., Marzio, and Alex P., getting lost in the snowy Sierras with Matteo, Paola M., and the Scout, ski trips year after year with the bellos, and Saturday morning coffee and pitstops with Erika. Glamour queens Florence and Tashi kept me on my toes.

Lastly, but perhaps the most importantly, I thank my mother, who has always encouraged me, and who believes that there are no limits to a woman's ability in any endeavor.

# Chapter 1

## Introduction

Knowledge of the Earth's density distribution is important for understanding many physical aspects of the Earth's interior, in terms of composition, geodynamics, and mineral physics. Relating radially symmetric density models with cosmic abundances has been instrumental in our early understanding of the bulk composition of the Earth's interior. Three-dimensional density variations cause the buoyancy forces which drive convection in the mantle and the core. Models of lateral variations in density could provide valuable information on properties of Earth materials by analyzing correlations of density perturbations with models of bulk velocity and/or shear velocity perturbations.

Estimation of the Earth's radial density distribution began with the measurements on the mass and moment of inertia of the Earth. The problem then proceeded to take into account the density equation of state by considering the seismic bulk velocity (*Williamson and Adams, 1923*) and the Earth's temperature gradient. In the 1960's, eigenfrequencies of fundamental terrestrial oscillations

tions were used to constrain the Earth’s radial density profile even further.

To date, inferences on the three-dimensional density structure have, on the most part, been made from seismic velocity observations, from which density variations have been extrapolated by assuming thermal relations to velocity perturbations. *Tanimoto, 1991* measured the density of the shallow upper mantle by waveform inversion of high order fundamental modes. Geodynamicists (*eg., Lithgow-Bertelloni and Richards, 1998; Ricard et al., 1994*) have been quite successful predicting the Earth’s gravitational potential field using forward models of tectonic plate motions and convection studies. An update of the radial density profile has been documented by *Kennett, 1998* by analyzing a number of normal mode central frequency estimates. More recently, *Ishii and Tromp, 1999* have reported their measurements of the three-dimensional density structure based on normal mode ‘splitting coefficients’ (*Giardini et al., 1988*), which are a processed form of normal mode spectra. Measurement techniques for the three-dimensional density structure of the Earth’s interior are explored in this thesis, by astrophysical and geophysical observations. Portions of the research in this thesis have been conducted contemporaneously with that of *Ishii and Tromp, 1999*, in which normal mode spectra are analyzed for three-dimensional density.

In Chapter 2, the feasibility of measuring density structure in the Earth by observations of extraterrestrial neutrinos is investigated. Attenuation of neutrinos as they pass through the Earth is examined theoretically. This method of



non-invasive imaging is analogous to medical X-ray computed tomography. Neutrinos are chargeless elementary particles with little mass which interact weakly with matter, and only very high energy neutrinos ( $\geq 10^{12}\text{TeV}$ ) are attenuated by the atomic densities relevant to the Earth's deep interior. Unfortunately, for neutrinos at these high energies, the construction of detectors is cost-limiting, and the probable count rate of measurements for these high energy neutrinos is deficient for making density measurements of the Earth in a reasonable lifetime of a geophysicist.

Next, we propose to take advantage of seismic data collected from digital broadband seismometers, with a large dynamic range, which were emplaced around the globe in the early 1990's. Two great seismic events in 1994, the Bolivia event on June 9, and Kurile event on October 4, incited seismologists to analyze the eigenfrequency perturbations of the Earth's free oscillations offered by the new data from the digital instruments. The eigenperiods of the Earth's oscillations have sensitivity to the Earth's density structure. This thesis will outline the investigation for three-dimensional density structure and seismic velocity structure from free-oscillation spectra. In Chapter 3 the theory of the Earth's normal modes and the method by which we expect to unravel density, as well as seismic velocity perturbations, from the data is defined. Chapter 4 outlines the inverse methods used in this analysis.

In Chapter 5, we describe in detail the process by which we extract our

models of seismic velocity perturbations and density perturbations, as derived from our normal mode spectral measurements. Our models are presented, and we find good agreement in our velocity models with other previously published work (*Li and Romanowicz, 1996; Dziewonski et al., 1997; Masters et al., 1996; Vasco and Johnson, 1997*). We also parameterize our models to investigate the topography of the core mantle boundary, and find that the pattern of boundary undulations are similar to results from PcP travel time studies (*Obayashi and Fukao, 1997; Rodgers and Wahr, 1993*). Density perturbations appear in almost all depths of the mantle which correspond to expected locations for slabs sinking in a non-layered, convecting mantle.

Finally, the stability and robustness of our models are assessed in Chapter 6. We compare and contrast three types of density models: 1) our density models derived from normal mode spectra, 2) the density model published in *Ishii and Tromp, 1999* derived from normal mode splitting coefficients, and 3) artifact density models computed from our resolution tests which result from contamination of compressional and shear velocity heterogeneity.

## Chapter 2

### Neutrino tomography for Earth structure

#### 2.1 Abstract

Astrophysical sources of very high-energy neutrinos may offer a novel means of imaging the Earth's internal structure. Likewise, occultation by our planet's core-mantle structure can help constrain the locations of extragalactic neutrino sources. Neutrino observations from the Earth's surface thus motivate new levels of collaboration between astrophysics and geophysics.

#### 2.2 Introduction

The Earth's internal structure is primarily defined by the seismologically observed variations in density and elastic-wave velocities at depth. Among the measured properties of the interior, density plays a special role because it is the most readily interpreted in terms of composition and state, the distinction between the Earth's silicate shell (mantle plus crust) and iron-alloy core being a case in point. In addition, it is the lateral variations in density that con-

trol the thermal and tectonic evolution of the interior. These represent the buoyancy forces driving mantle convection, plate tectonics and, indeed, most of the global-scale geological processes in the planet. At present, seismological determinations of the Earth's free-oscillation modes, complemented by geodetic measurements, provide the only means of obtaining the density distribution within the mantle and core [Dziewonski and Anderson, 1981]. In detail, this represents a complex inverse problem, and the radial density distribution is resolved to a fraction of one percent only when averaged over depth intervals of several hundred to 1000 kilometers or more [Gilbert *et al.*, 1973]. Because of its geophysical significance, however, there is considerable motivation to enhance determinations of the Earth's internal density structure. Improved spatial resolution, especially in lateral directions, and even a redundant measurement of internal densities obtained by independent, non-seismological methods would be of great value. Recent interest in observing very-high energy ( $\sim$ TeV-PeV) neutrinos emitted from Active Galactic Nuclei and other extraterrestrial sources suggests that astrophysical observations may provide independent constraints on the Earth's internal density structure [Wilson, 1984; Roberts, 1992; Berezhinski'i *et al.*, 1986]. Unlike the well-known solar or supernova neutrinos, which are much lower in energy ( $\sim$ keV-MeV) and pass through the Earth essentially unattenuated, the very-high energy (VHE) neutrinos are significantly absorbed by the planetary interior (Figure 2.1). Specifically, a muon-neutrino  $\nu_\mu$  is ab-

sorbed when it interacts with a nucleon  $N$  by charged-current interactions, and changes into a muon :

$$\nu_\mu + N^n \rightarrow \mu^- + X^{n+1} \quad (2.1)$$

where  $X$  represents the remaining products of the interaction, and  $n$  is the charge of the nucleon; a similar process yields electrons from interactions of electron-neutrinos with nucleons. Since the neutrino-nucleon scattering cross section, the probability of neutrino interaction with a nucleon, rises linearly with energy up to nearly 10 TeV [*Quigg et al., 1986*], the cross section is sufficiently high for neutrinos of TeV-PeV energies to be significantly absorbed within the Earth. The resulting absorption of VHE neutrinos is proportional to the nucleon number, hence the integrated mass density along the neutrino path through the Earth (Figure 2.1). In addition to the potential for an independent measurement of the Earth's density structure, recent developments motivate our analysis: the observation of candidate extraterrestrial sources of VHE neutrinos, the construction of detector arrays designed to observe these astrophysical neutrinos within the next few years, and updated neutrino-nucleon scattering cross sections [*Frichter et al., 1995*]. With these, we consider the determination of the internal density variations through the direct absorption of these natural VHE neutrinos. This approach distinguishes our study and Wilson's [*Wilson, 1984*] from other's [*De Rújula et al., 1983; Askar'yan, 1984; Borisov et al., 1986; Tsarev and Chechin, 1986*], in which the use of accelerator-produced neutrinos has been considered.

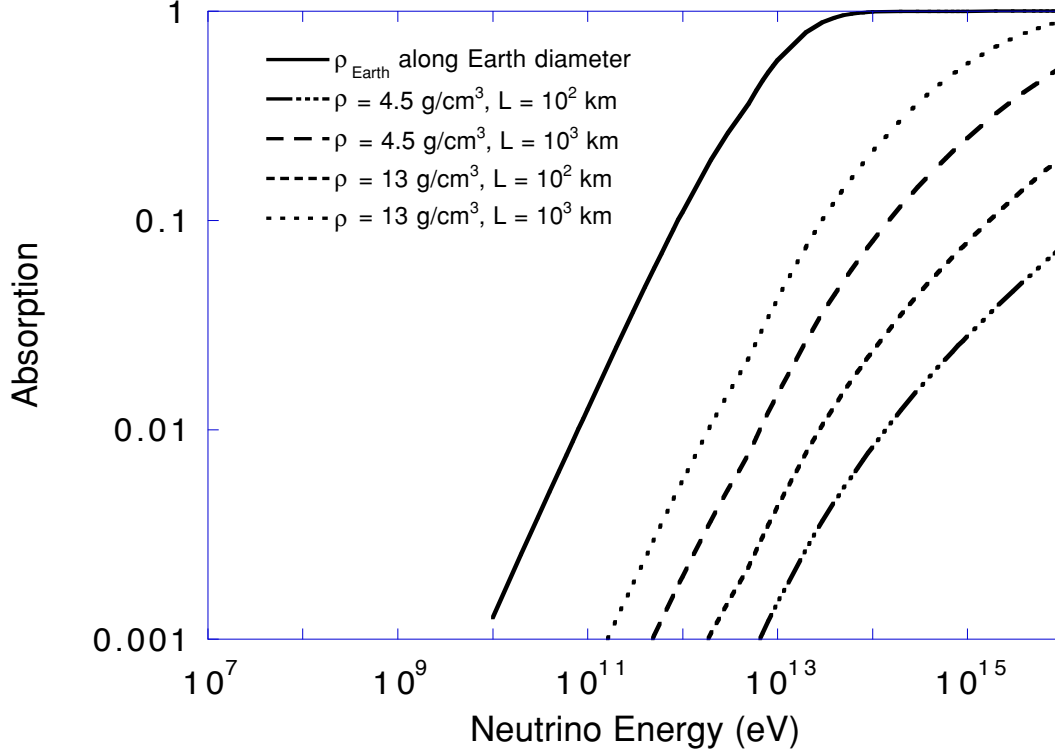
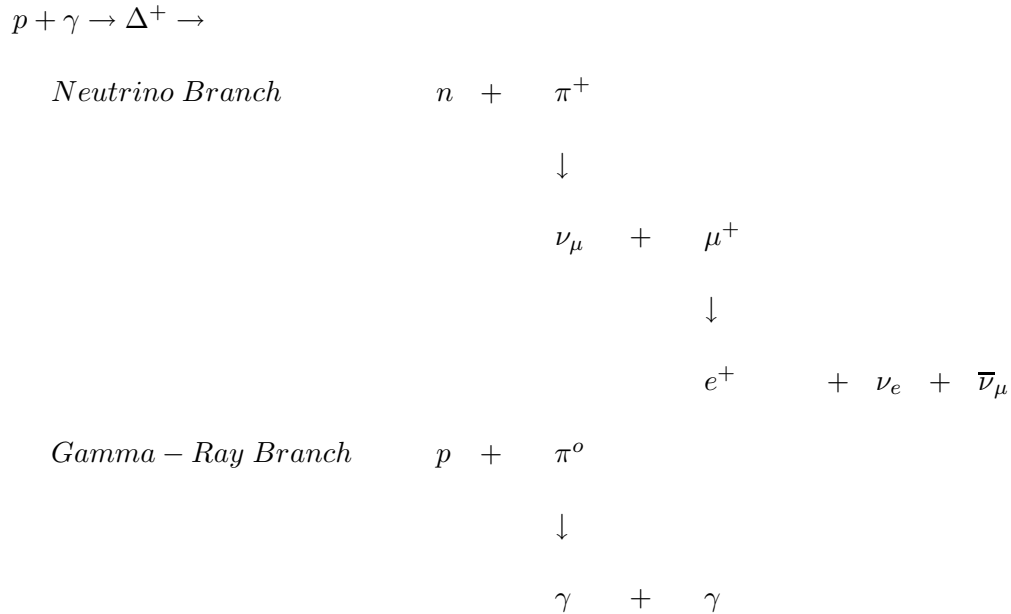


Figure 2.1: Calculated absorption as a function of energy for neutrinos passing through material of given density and thickness (Absorption = 1 indicates total absorption). The neutrino-nucleon scattering cross section [Frichter *et al.*, 1995] is used for this calculation. The solid line corresponds to a path directly through the center of the Earth, whereas dashed lines show the neutrino absorption for paths through regions of specified thicknesses and average densities:  $\rho = 4.5$  and  $13 \text{ g/cm}^3$  are typical densities for the Earth's mantle and core, respectively. The present study focuses on the very-high energy (VHE) range of  $\sim \text{TeV-PeV}$  ( $10^{12} - 10^{15}$  electron volts).

## 2.3 Neutrino Sources

The main sources of neutrinos considered here are thought to be associated with the highest known energy processes in the universe: Active Galactic Nuclei (AGNs), black holes, quasars, pulsars, and gamma-ray bursters. The primary mechanism creating the extragalactic neutrinos is one whereby protons are accelerated near the dense, matter-accreting cores of celestial objects [Stecker *et al*, 1992]. The high-energy protons ( $p$ ) collide with ultraviolet photons ( $\gamma$ ), exciting a baryon resonance ( $\Delta^+$ ) that decays into: i) a charged pi-meson ( $\pi^+$ ) plus a neutron ( $n$ ), ultimately creating neutrinos (Neutrino Branch); or ii) a neutral pi-meson ( $\pi^0$ ) plus a proton, finally decaying to gamma-rays ( $\gamma$ ) (Gamma-Ray Branch).



Decay via the Neutrino Branch, which occurs half as often as via the Gamma-

Ray Branch, results in a muon neutrino daughter and a muon antineutrino granddaughter product, as well as an electron neutrino ( $\nu_e$ ). Since this mechanism produces neutrinos and  $\gamma$ -rays at similar energies, strong  $\gamma$ -ray sources are considered as potentially strong sources of VHE neutrinos. The observation of VHE cosmic rays provides support for this VHE neutrino production model, the centers of active galaxies being the most probable sites in which cosmic rays could be accelerated to such high energies [*Cronin, 1990*]. New measurements obtained from the Compton Gamma Ray Observatory (GRO) reveal the existence of high-flux gamma-ray emitters, "blazars," that may be promising neutrino sources for our purposes [*Fichtel, 1994*]. Specifically, the gamma-ray spectrum has been found in a number of cases to decrease more slowly with energy than previously expected. Referring to the photon spectral index ( $\alpha$ ) (the negative of the logarithmic derivative of the gamma-ray flux  $F$  with respect to energy  $E$ ), sources with spectral indices as low as  $\alpha = -d\ln F/d\ln E = 1.5$  have now been found (Table 2.1). Previous values all lay above  $\alpha = 2$ , so the new data imply a larger flux at the higher energies pertinent to our study than had been estimated in the past. The neutrino fluxes from these sources are expected to be as much as 200 times higher than the gamma-ray fluxes at equivalent energies, since the neutrinos are not affected by the electromagnetic interactions attenuating the gamma-rays traversing photon fields and matter in the AGNs and in interstellar space [*Berezinsky and Learned, 1992; Bassani*



Table 2.1: <sup>a</sup> Sources identified by right ascension (h hours, m minutes) and declination (d tenths of degrees) as hhmmdd. [15] <sup>b</sup> The effective DUMAND area used for this calculation is 20,000  $m^2$ . <sup>c</sup> Assumed ratio of neutrino flux to gamma-ray flux emitted from the source (see text). <sup>d</sup> see *Stenger, 1992*.

#### Gamma-Ray Blazars as VHE Neutrino Sources

Source <sup>a</sup>	Gamma-Ray Flux for $E > 0.1 \text{ GeV}$ ( $10^{-6} \text{ cm}^{-2} \text{ s}^{-1}$ )	Photon Spectral In- dex ( $\alpha = -d \ln F / d \ln E$ )	Muon events per year at DUMAND <sup>b</sup> for $E_\mu > 10$ TeV ( $\nu/\gamma = 1$ ) <sup>c,d</sup>	Muon events per year at DUMAND <sup>b</sup> for $E_\mu > 10$ TeV ( $\nu/\gamma = 200$ ) <sup>c</sup>
0208-512	0.4 to 0.9	$1.7 \pm 0.1$		
0446+112	$1.0 \pm 0.2$	$1.8 \pm 0.3$		
0716+714	$0.20 \pm 0.06$	$1.8 \pm 0.2$		
1622-253	0.2 to 0.4	$1.9 \pm 0.5$		
2022-077	$0.7 \pm 0.1$	$1.5 \pm 0.2$		
1101+384 (Mrk 421)	$0.14 \pm 0.03$	$1.9 \pm 0.1$	0.67	137
1253-055 (3C 279)	$2.7 \pm 0.1$	$1.9 \pm 0.1$	4.2	840

and Dean, 1981; Jelley, 1966]. Although the new estimates of VHE neutrino fluxes are significantly higher than in the past, they remain well below the apparent upper limit set by measurements using the Irvine-Michigan-Brookhaven (IMB) detector [Becker-Szendy, 1991]. Still, being higher than Wilson's [Wilson, 1984], the recent estimates of neutrino fluxes yield a more optimistic prognosis for imaging the Earth's internal structure. The gamma-ray fluxes from the "blazars" have been observed to be variable. If the neutrino source intensity is proportional to these measured gamma-ray fluxes, then the neutrino fluxes may also vary with time. However, as long as the variation of neutrino source intensity does not have a significant Fourier component at a frequency of once per sidereal day, or exact multiples thereof, the source variability should cancel out when the transmission of neutrinos is averaged over many cycles of rotation of the Earth. As noted below, monitoring the gamma-ray fluxes and using more than one neutrino detector array can also serve to calibrate the neutrino fluxes as a function of time. Extragalactic neutrinos are not limited to coming from point sources. A diffuse spectrum of high-energy neutrinos emitted from AGNs and massive black holes spread quasi-uniformly over the sky could also serve to map the Earth's internal density structure; many of these sources may not be detectable optically [Stecker and Salamon, 1993]. The neutrinos would be incident at the detector from all directions, thus providing a volume scan of the Earth that is self-calibrating. That is, the patch of sky viewed when it is tangent

to the Earth is compared to observation when it is behind the Earth. Spatial resolution of the internal density structure is then limited only by the angular sensitivity of the detector array, typically  $\sim 1^\circ$  [Roberts, 1992]; for comparison, the core subtends  $\pm 30^\circ$  about the nadir as observed from the Earth's surface. In addition to the extragalactic sources, interactions of very-high energy cosmic rays with the atmosphere produce a diffuse flux of neutrinos [Wilson, 1984]. These neutrinos come mostly from the horizon, following a  $\secant(\theta)$  angular distribution [Flatté et al., 1971], but represent a source that is not self-calibrating. Moreover, the atmospheric neutrinos have a steep energy spectrum ( $\alpha > 2$ ), implying a diminished flux at the energies of interest here. Because the atmospheric neutrinos seem less promising for our application, and little is yet known about the spectrum and flux of the diffuse extragalactic source, we focus the remaining discussion onto point sources of VHE neutrinos.

## 2.4 Neutrino Detectors

Astrophysical interest in the extragalactic sources of neutrinos, further heightened by the recent gamma-ray observations, has motivated the construction of several neutrino observatories at the Earth's surface. At least four such detector arrays have been contemplated, planned or constructed: AMANDA [Barwick et al., 1993] in the ice of Antarctica, DUMAND II [Roberts, 1992] in the Pacific Ocean off the coast of Hawaii, NESTOR [Resvanis et al., 1992] in the Mediter-

ranean Sea off the coast of Greece, and the Neutrino Telescope [*Belolaptikov et al., 1994*] in Lake Baikal, Siberia. All of these detector arrays are designed to measure the incoming neutrino flux indirectly, by recording the muons created from muon-neutrinos interacting with terrestrial matter through the charged-current weak interactions (Equation 2.1). Each muon created in this manner continues along essentially the trajectory of the original neutrino. The muon either stops within the Earth or, if it has enough energy, escapes from the solid Earth out the opposite end of the chord where the neutrino entered (see inset, Figure 2.2). The muons eventually lose energy via electromagnetic interactions. For the energies of interest to this study, muons can travel many kilometers in solid or liquid matter before they are stopped: a 1 TeV muon travels 5 km through the crust, for example. It is the Cherenkov radiation produced in water or ice by the muons escaping the solid Earth that is recorded by the detector arrays. Muons traversing the effective area of the array in an upward direction are thus interpreted as originating from neutrino-nucleon interactions. Briefly, using the DUMAND II (Deep Underwater Muon and Neutrino Detector II) array as an example, nine 350 m long strings holding 24 photomultiplier tubes each were to be anchored at 4.8 km depth in the ocean [*Roberts, 1994*]. The water encompassed by the array acts as the detector for the neutrino-generated muons. Although DUMAND II would enclose a volume of  $2 \times 10^6 m^3$ , the effective volume of the detector reaches  $2 \times 10^8 m^3$ , depending on the energy of the

muon. From the arrival time of Cherenkov photons at the different photomultiplier tubes, the direction and, to a more limited extent, the energy of the original neutrino can be inferred. In its final configuration, the array was designed to have directional resolution of  $\leq 0.5 - 1^\circ$ , and to be sensitive to neutrinos having energies between 50 GeV and at least 100 TeV [*Roberts, 1992*].

## 2.5 Geophysical Application: Implementation and Resolution

As a consequence of the Earth's rotation, only one extraterrestrial source and one detector array at a single site are sufficient to sample the Earth's density profile. As the planet rotates, the neutrino source sweeps across the detector's downward field of view (through the Earth), with the neutrino beam intersecting the mantle and core in a continuous set of chord paths. Monitoring the neutrino flux as a function of time then reveals the variations in neutrino transmission due to the Earth's internal density structure. Results for sources at three representative declinations, as observed from the DUMAND array, are shown in Figure 2.2. The relative intensity of transmitted neutrinos,  $I/I_0$  ( $I_0$  is the incident intensity), is calculated assuming the spherically symmetric density distribution obtained from seismology [*Dziewonski and Anderson, 1981*]:  $I/I_0 = \exp(-\sigma n_N)$ , where  $\sigma$  is the neutrino-nucleon scattering cross section and  $n_N$  is the integrated nucleon number density along the neutrino path through the

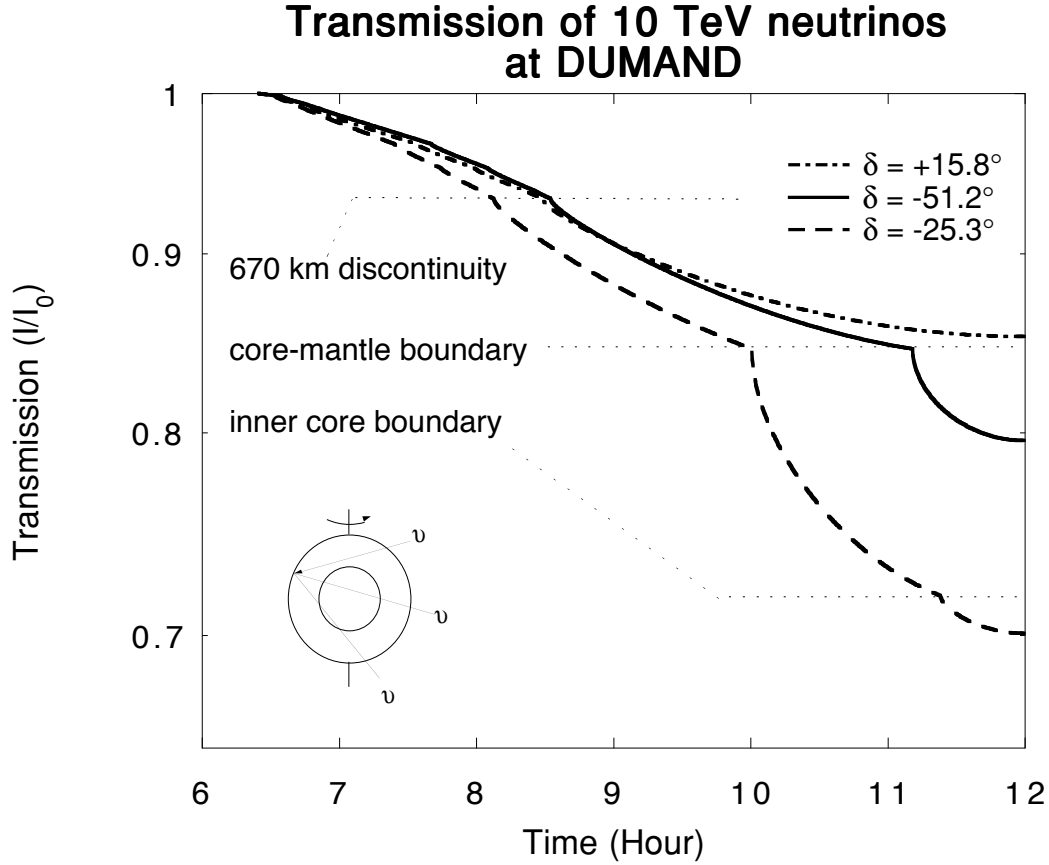


Figure 2.2: Calculated neutrino transmission as a function of sidereal time for sources observed from the DUMAND location (Hawaii) and located at declinations of  $\delta = +15.8^\circ$ ,  $-51.2^\circ$ , and  $-25.3^\circ$ .

Earth [Wilson, 1984]. The boundaries of large density contrast, such as the core-mantle boundary, are characterized by changes in the slope of each transmission curve versus time.

The curves illustrate the effects on the neutrino transmission of sources being occulted only by the upper and lower mantle ( $\delta = 15.8^\circ$ ,  $-25.3^\circ$  and  $-51.2^\circ$ ); by the mantle and outer core ( $\delta = -25.3^\circ$  and  $-51.2^\circ$ ); and by the mantle, outer core and inner core ( $\delta = -25.3^\circ$ ). The Earth's density profile is thus revealed

down to the depth of maximum penetration by the neutrino paths,

$$z_{max} = R_e(1 - \sin|\delta + \lambda|) \quad (2.2)$$

with  $\delta, \lambda$  and  $R_e$  being, respectively, the source declination, detector latitude and Earth's radius. Consequently, the spherically averaged density structure can in principle be fully determined from one detector-source pair with a path traversing the center of the planet; this requires  $\delta = -\lambda$ . Figures 2.3 through 2.5 summarize the locations, hence maximum penetration depths, of potential VHE neutrino sources as seen from the sites of the AMANDA, DUMAND and NESTOR arrays (cf. Table 2.1). Because of their low latitudes, the latter two sites are advantageous for mapping the deepest structure of the planet. If observed from both DUMAND and NESTOR, for example, source 1622-253 yields redundant determinations of inner-core density, whereas sources 1253-055, 2022-077 and 0208-512 provide independent measurements of outer-core densities (Figures 2.4, and 2.5). The AMANDA site, near the South Pole, offers complementary advantages due to its high latitude. First, because the sources just mentioned are not occulted by the Earth, the AMANDA array can monitor the temporal stability of their neutrino fluxes (Figure 2.3). A combination of redundant observations from several neutrino observatories and of gamma-ray measurements from satellite-borne detectors (e.g., GRO) can additionally serve as monitors of source stability. Second, because the transmission curves at AMANDA are essentially flat if density depends only on radius (Figure 2.6),

any deviations from constant transmission observed at this site can be directly ascribed to lateral variations in the Earth's density structure. Indeed, such measurements may provide the first clear indication of horizontal density structure at specific depths in the mantle and core. At the same time, neutrino determinations of average densities at these individual depths, given by the individual source declinations  $\delta$ , are best constrained by the (nearly) flat transmission curves obtained at AMANDA. Imaging the Earth's density structure can in principle be extended to three dimensions, if more than one detector array is used and if sources of high enough flux are found at a sufficient number of distinct locations. For example, a diffuse extragalactic source of neutrinos impinges on the Earth isotropically, and can thus provide the required source geometry for three-dimensional imaging. However, this approach is no doubt limited by the neutrino flux, as we next discuss. The spatial dimension and density contrast of internal structure that is resolved depends on the number of detected muons generated from neutrinos that pass through the regions or features of interest. As an example, we summarize current estimates of neutrino-generated muon event rates at DUMAND in Table 2.1; the neutrino fluxes on which these values are based are set at 1-200 times the gamma-ray fluxes emanating from the sources, as noted above [*Stenger, 1992*]. Thus, for the single source 1253-055 (3C 279), the number of  $>10$  TeV neutrino-generated muons detectable at the nine-string DUMAND array is estimated to lie between 4.2 and 840 per



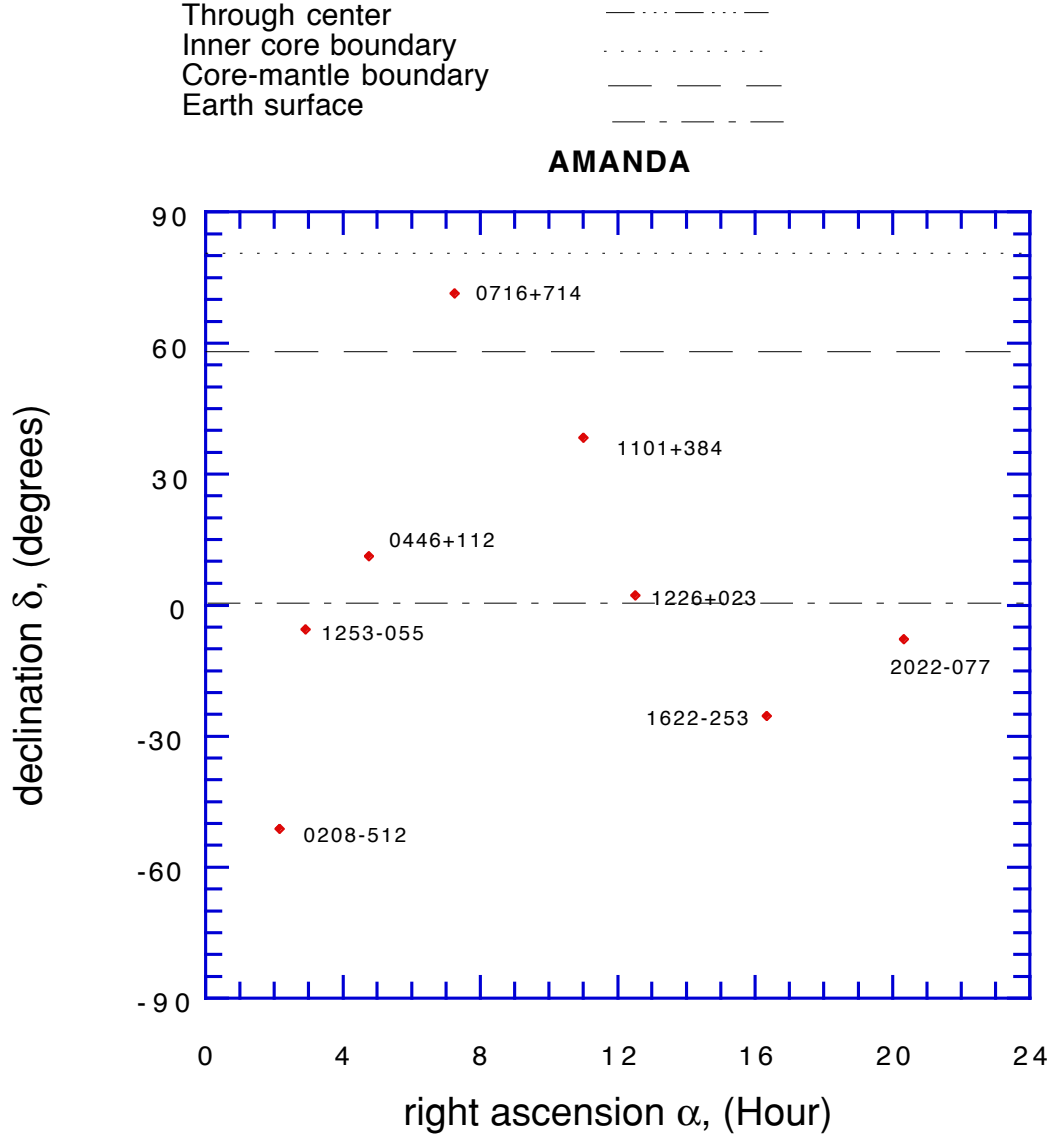


Figure 2.3: Sky maps of some potential VHE neutrino sources, as observed from the sites of the AMANDA array. For comparison, the main structural boundaries of the Earth are projected onto the maps according to Eq. (2.2). Sources located between boundary lines are occulted by the specified layer of the Earth.

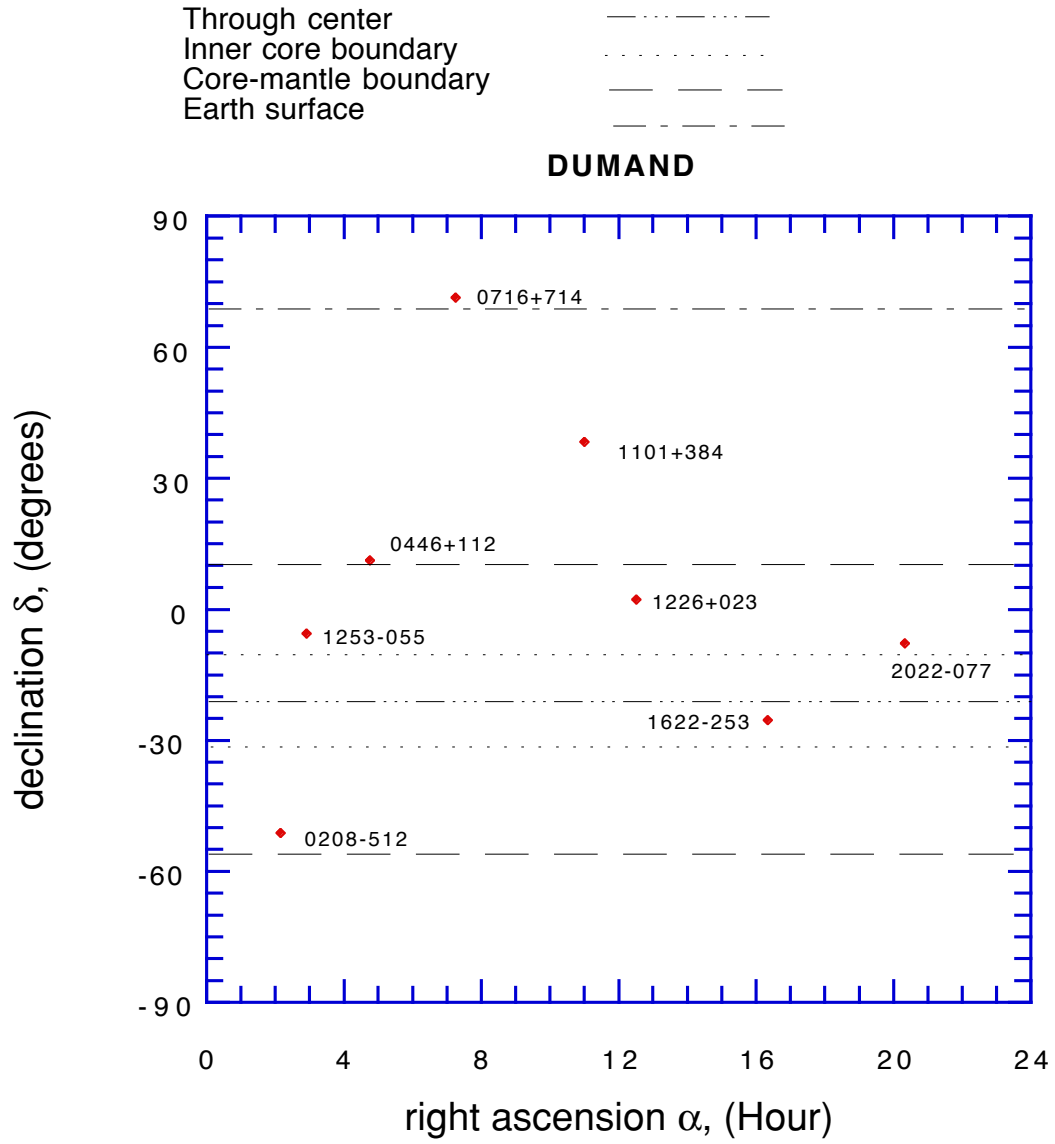


Figure 2.4: Same as for Figure 2.3 but for the DUMAND array.

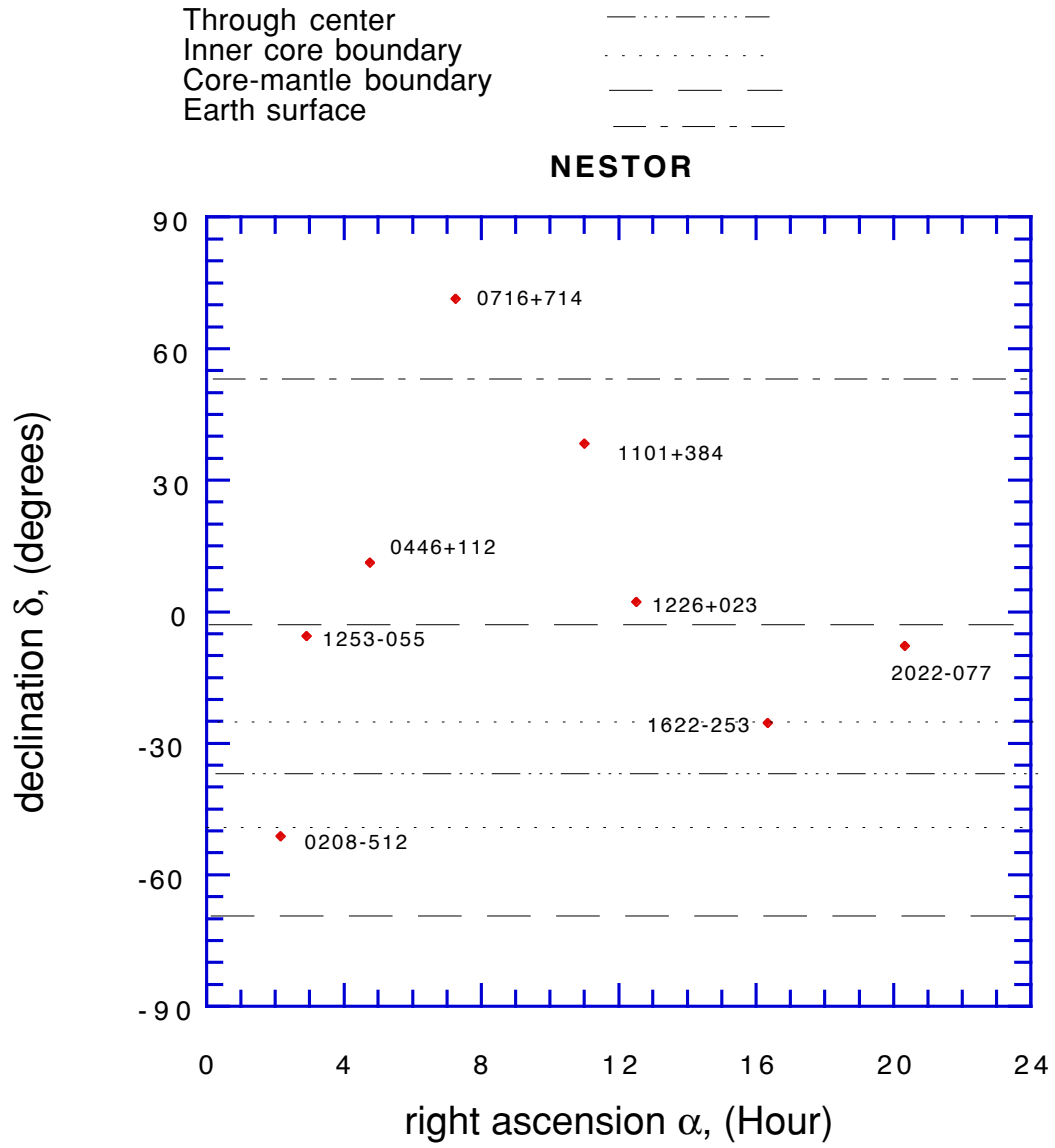


Figure 2.5: Same as for Figure 2.3 but for the NESTOR array.

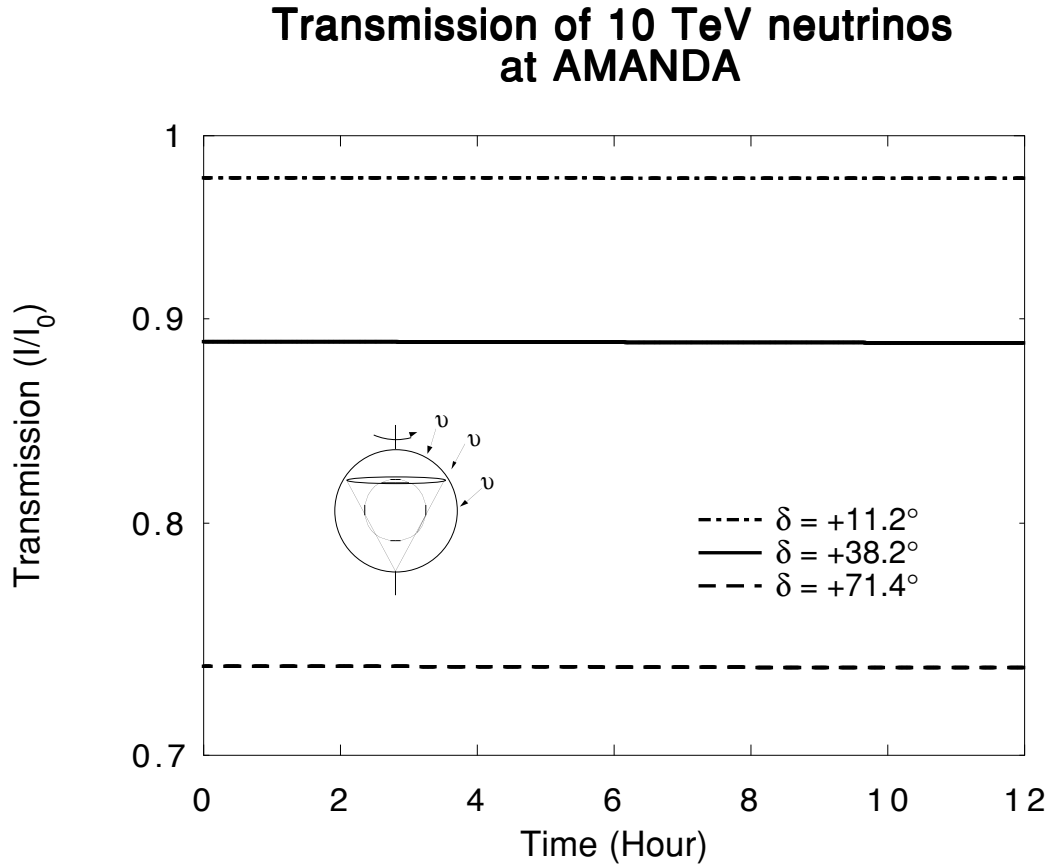


Figure 2.6: Neutrino transmission versus sidereal time for three sources observed from a site located near the South Pole (AMANDA). The curves are calculated as in Fig. 2.2, assuming the spherically symmetric (horizontally averaged) density structure obtained from seismology [Dziewonski and Anderson, 1981], and they are flat because of the constant path length of neutrinos coming from sources of declination  $\delta > 0$  (see inset). For source declinations of  $\delta = 11.2^\circ$ ,  $38.4^\circ$ , and  $71.4^\circ$ , respectively, neutrino paths pass through the upper mantle alone; through the upper mantle and lower mantle; and through the entire mantle and outer core, narrowly missing the inner core (cf. Fig. 2.2).

year (Table 2.1). Assuming the factor of 200 enhancement of neutrinos over gamma-rays, 10 years' observation of ten sources is expected to yield  $10^4 - 10^5$  recordable muon events having energies above 10 TeV. To determine the resolution of the density structure that can be measured by neutrino absorption, we imagine dividing the array field of view into bins of width equal to  $1/3$  the transit time required for the source point to traverse past the density feature. For instance, a source at  $\delta = -25^\circ$  is occulted by the 6980 km diameter core for roughly 4 hours out of the  $\sim 14$  hours each day it is in the DUMAND field of view. This gives 8 bins, 1.6 hours long each, during 3 of which only 75-80 out of 100 neutrinos can be observed, for 10 TeV neutrinos (20-25% absorption by the core: Figure 2.2). The statistical uncertainty corresponds to a standard deviation less than  $80^{1/2} = 8.9$ , indicating the core density is constrained to an accuracy of  $\sim 10\%$  with just 100 counts for paths going through this region. Evidently, such a count rate, hence resolution, is feasible in less than 1 year with one well-placed source (e.g., 1622-253) having sufficiently high flux (e.g., 1253-055). However, neither the number of neutrino sources nor the number of detector arrays is limited to one. Multiple observations of more than one source serve two important purposes: they can drastically reduce the number of years required to obtain density measurements with reduced uncertainties, and also can provide redundancy to the signal in the event that a particular time variable source is viewed during its minimum cycle. Figure 2.7 summarizes the

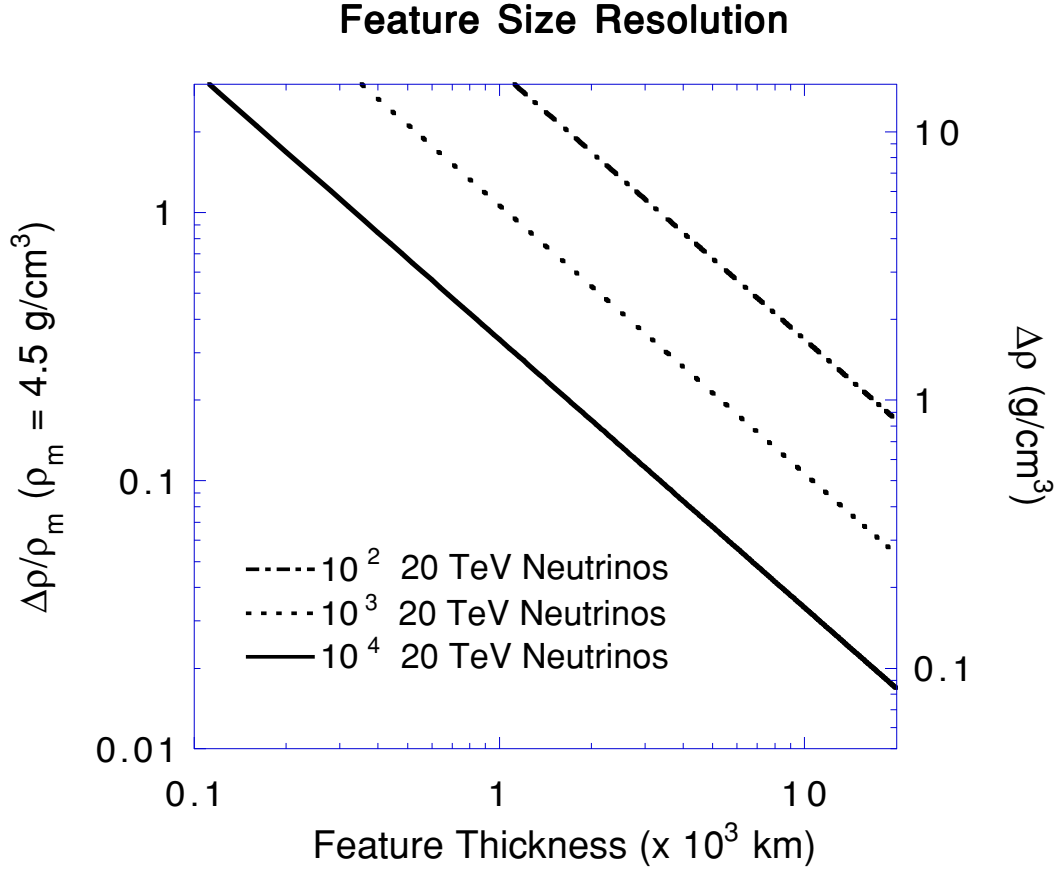


Figure 2.7: Number of neutrinos required to establish, to one standard deviation, the presence of a feature of given thickness and differential density ( $\Delta\rho$ ) with respect to surrounding material.

tradeoff between size and density contrast for features to be resolved to within one standard deviation by a given number of cross-cutting neutrinos. Fewer than 100 detected events due to core-traversing neutrinos suffice to establish the presence of this region, for example (radius  $r_{core} = 3480$  km and density  $\rho_{core} \cong 10.6 \text{ g cm}^{-3}$ , versus  $\rho_{mantle} \cong 4.5 \text{ g cm}^{-3}$ ), where the densities given are characteristic of the region. In contrast, constraining either the density jump across the inner core - outer core boundary ( $\Delta\rho \cong 0.6 \text{ g cm}^{-3}$ ,  $\rho_{IC} = 1220$  km)

or the possible density variations due to mantle-core intermixing in the D'' zone at the base of the mantle ( $\delta\rho \cong 6gcm^{-3}$ , thickness  $\leq 200$  km) requires about  $10^4 - 10^5$  events. This is prospectively achievable at more than one detector array over a decade's observations.

## 2.6 Location of Neutrino Sources by Core Occultation

In addition to the geophysical applications, neutrino absorption by the Earth's internal structure may serve the astrophysical community interested in precisely determining the locations of VHE neutrino point sources. Because the radius of the outer core is known to better than 0.1% from seismology [*Dziewonski and Anderson, 1981*], we can take advantage of occultation by the Earth's core to locate an extraterrestrial point source of neutrinos. First, the right ascension of the source is determined absolutely by the sidereal time of occultation in the transmission curve (e.g., Figure 2.2). Second, the source declination is obtained from the total amount of time spent behind the core, which varies with  $\delta$  (Figure 2.2). Clearly, the technique of using core occultation to locate neutrino point sources works best with detector arrays sited at low latitudes (cf. Figures 2.2 and 2.6). Furthermore, the occultation is most sensitive to declination when the source is located such that its neutrinos pass near the edge of the core:  $z_{max} \approx 2885km$ , the depth to the core-mantle boundary (Equation 2.2), rather than straight through the core. For example, it is easier at DUMAND to dis-

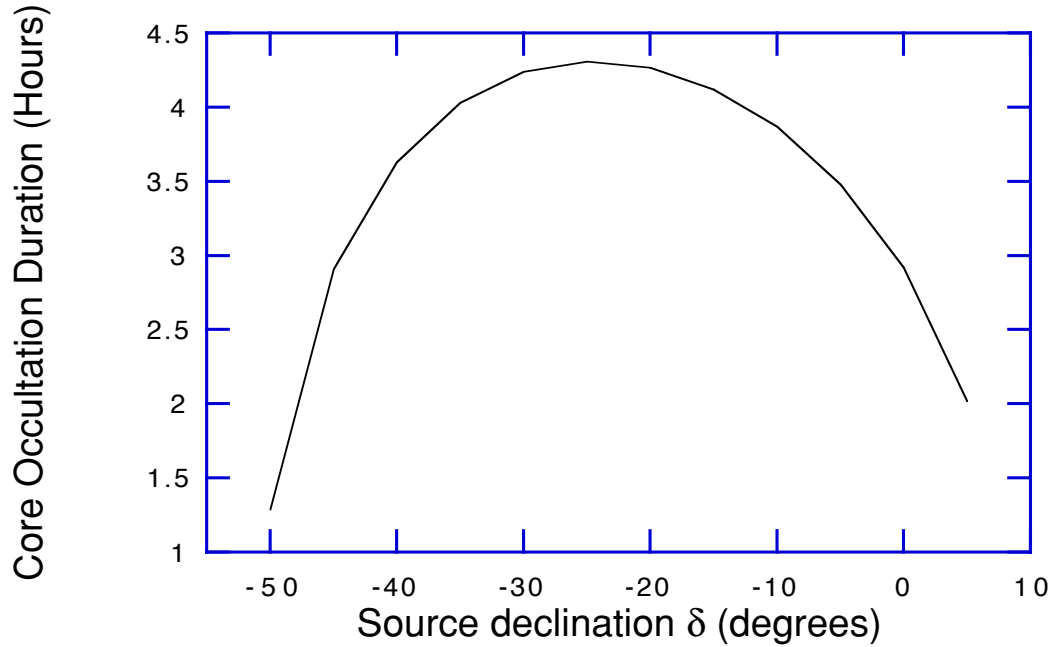


Figure 2.8: Core occultation duration as a function of source declination calculated for neutrinos detected at a site of latitude  $\lambda = 21^\circ$  (e.g., DUMAND). The occultation duration is highly sensitive to source declinations for  $\delta \approx -50^\circ$  and  $+5^\circ$ .

tinguish between sources of declination  $0^\circ$  and  $5^\circ$ , than between sources of  $-20^\circ$  and  $-25^\circ$  (Figure 2.8).

Thus, both DUMAND and NESTOR are most sensitive to locating sources at declinations near  $-5^\circ$  to  $+10^\circ$  and  $-55^\circ$  to  $-70^\circ$  through occultation by the core-mantle boundary (Figures 2.4 and 2.5). If the inner core-outer core boundary can be similarly used (Figure 2.2), source declinations near  $-10^\circ$  and  $-30^\circ$ , and near  $-25^\circ$  and  $-70^\circ$  are resolved by DUMAND and NESTOR, respectively.



## 2.7 Conclusion

Observations of astrophysically-produced Very High Energy ( $\sim$ TeV-PeV) neutrinos, using one or more detector arrays at the Earth's surface, may yield significant new constraints on the density structure of the planetary interior. Current estimates of VHE neutrino fluxes from extragalactic point sources suggest that geophysically interesting results can be obtained over time periods of years to decades (Table 2.1). At the same time, precise seismological information on the Earth's internal structure, such as the depth to the core-mantle boundary, can be used to obtain refined locations of neutrino point sources. Detector arrays now under construction will test the feasibility of these applications over the next few years.

## Chapter 3

### Normal Mode Theory

#### 3.1 Normal Modes of the Earth

Seismic waves radiated from a large earthquake source coherently interfere to produce standing waves in the Earth. The elastic Earth continues to deform hours to days after the excitation provided by a strong earthquake source has died out, in the form of free oscillations, or standing waves.

Seismologists generally work starting from a reference Earth model, which has the following properties:

1. spherically symmetric;
2. non-rotating ;
3. elastic ;
4. isotropic,

is given the nomenclature 'SNREI Earth model.' In such a model, the equation

of motion for displacement in the Earth is given by

$$\rho_0 \frac{d^2 \mathbf{x}}{dt^2} = \nabla \cdot \tau + \mathbf{F} \quad (3.1)$$

where  $\rho_0$  is the density of the reference Earth model,  $\mathbf{x}$  is the point displacement vector,  $\tau$  is the total stress tensor, and  $\mathbf{F}$  is the body force per unit volume. In the quiescent state,  $\mathbf{x}=0$ ,  $\mathbf{F}$  is the gravitational body force  $\mathbf{F} = \rho_0 \mathbf{g} = -\rho_0 \nabla \phi_0$ , and the stress distribution  $\tau$  is the hydrostatic pressure due to rock overburden  $\tau_0 = -p_0 \mathbf{I}$  where  $p_0$  is hydrostatic pressure, and  $\mathbf{I}$  is the identity tensor.

When  $\mathbf{F}$  includes an excitation term, the SNREI Earth undergoes infinitesimal time dependent deformations. A particulate of Earth material initially at position  $\mathbf{r}_0$  displaces to position  $\mathbf{r}$  by

$$\mathbf{r}(\mathbf{r}_0, t) = \mathbf{r}_0 + \mathbf{x}(\mathbf{r}_0, t). \quad (3.2)$$

Due to the elastic properties of the material, stresses will act on the deformation to restore the particulate back to its original position. For an isotropic Earth, the elastic stress tensor is

$$\tau_E = 2\mu\varepsilon + \lambda(\nabla \cdot \mathbf{x})\mathbf{I} \quad (3.3)$$

where  $\varepsilon$  is the elastic strain tensor given by

$$\varepsilon = 1/2(\nabla \mathbf{x} + (\nabla \mathbf{x})^T). \quad (3.4)$$

The density field and gravitational potential field are also perturbed by the

deformation:

$$\begin{aligned}\rho(\mathbf{r}_0, t) &= \rho_0(\mathbf{r}_0) + \delta\rho(\mathbf{r}_0, t) \\ \phi(\mathbf{r}_0, t) &= \phi_0(\mathbf{r}_0) + \delta\phi(\mathbf{r}_0, t)\end{aligned}$$

where  $\delta\rho$  and  $\delta\phi$  are small. Additionally, since the particulate is moving in a pressure gradient, the initial stress state is perturbed by the displacement  $-\mathbf{x}$  by

$$\delta\tau = -\mathbf{x} \cdot \nabla \tau_0(\mathbf{r}_0). \quad (3.5)$$

Substituting these terms into equation (3.1) and keeping only perturbations first order, we obtain:

$$\rho_0 \frac{\partial^2 \mathbf{x}}{\partial t^2} = \nabla \cdot (\tau_0 + \delta\tau + \tau_E) - \rho_0 \nabla \phi_0 - \delta\rho \nabla \phi_0 - \rho_0 \nabla \delta\phi + \mathbf{f} \quad (3.6)$$

where  $\mathbf{f}$  is the excitation body force. From equation (3.1), the initial condition that  $\mathbf{x}=0$  in the quiescent state requires that

$$\nabla \cdot \tau_0 - \rho_0 \nabla \phi_0 = 0. \quad (3.7)$$

Substituting  $\tau_0 = -p_0 \mathbf{I}$  into equation (3.5), we note that

$$\nabla \cdot \delta\tau = \nabla(\mathbf{x} \cdot \nabla p_0) = -\nabla(x_r g_0 \rho_0).$$

For the small quantities we are considering, the conservation of mass is

$$\frac{\partial \delta\rho}{\partial t} + \nabla \cdot \left( \rho \frac{\partial \mathbf{x}}{\partial t} \right) = 0,$$

and gives

$$\delta\rho = -\nabla \cdot (\rho_0 \mathbf{x}).$$

Equation (3.6) is then further simplified to

$$\rho_0 \frac{\partial^2 \mathbf{x}}{\partial t^2} = \nabla \cdot \tau_E - \rho_0 \nabla \delta \phi + \hat{\mathbf{r}} g_0 \nabla \cdot (\rho_0 \mathbf{x}) - \nabla (x_r g_0 \rho_0) + \mathbf{f}. \quad (3.8)$$

The gravitational potential satisfies Poisson's Equation, thus we have an additional equation defining  $\delta \phi$ ,

$$\nabla^2 \delta \phi = 4\pi G \delta \rho = -4\pi G \nabla \cdot (\rho_0 \mathbf{x}) \quad (3.9)$$

where  $G$  is the gravitational constant. Equations (3.8) and (3.9) are the fundamental equations governing the behavior of small deformations of the SNREI model.

At times after the excitation body force  $\mathbf{f}$  has ceased to act,  $\mathbf{f}=0$  in equation (3.8), which then becomes the equation of motion for free oscillations of the SNREI model. By seeking solutions for point displacement of the form

$$\mathbf{x}(\mathbf{r}, t) = \mathbf{x}_k e^{i\omega_k t},$$

equation (3.8) becomes an eigenproblem

$$-\rho_0 \omega_k^2 \mathbf{x}_k = \nabla \cdot \tau_E - \rho_0 \nabla \delta \phi + \hat{\mathbf{r}} g_0 \nabla \cdot (\rho_0 \mathbf{x}_k) - \nabla (x_{kr} g_0 \rho_0). \quad (3.10)$$

The free oscillations of an SNREI Earth model can be characterized by solving the eigenproblem written in symbolic form as

$$\mathcal{H}_0 \mathbf{x}_k^m = \rho_0 \omega_k^2 \mathbf{x}_k^m, \quad (3.11)$$

where  $\mathcal{H}_0$  is a Hermitian differential operator defined as the negative of the right hand side of equation (3.10),  $\omega_k^2$  is the squared eigenfrequency of a free

oscillation mode, and  $\mathbf{x}_k^m$  is a vector field of elastic displacement for the mode, and has the form

$$\begin{aligned} \mathbf{x}_k^m = |n\ q\ l\ m\rangle \equiv & {}_nU_l^q(r)Y_l^m(\theta, \phi)\hat{\mathbf{r}} + {}_nV_l^q(r)\nabla_1 Y_l^m(\theta, \phi) \\ & - {}_nW_l^q(r)\hat{\mathbf{r}} \times \nabla_1 Y_l^m(\theta, \phi). \end{aligned} \quad (3.12)$$

The bracket notation for an eigenmode  $|n\ q\ l\ m\rangle$  is adopted from quantum mechanics, where  $n$  is the overtone number,  $l$  is the angular order, and  $m$  is the azimuthal order of a type  $q$  (spheroidal or toroidal) mode. In an SNREI Earth model,  $2l + 1$  modes, or “singlets”, of different  $m$  but the same  $n, q$  and  $l$  oscillate at the same degenerate eigenfrequency  $\omega_k$ , and make up the ‘multiplet’  $k \equiv |n\ q\ l\rangle$ .  ${}_nU_l^q(r)$ ,  ${}_nV_l^q(r)$ , and  ${}_nW_l^q(r)$  are functions of radius  $r$ , are characteristic of each multiplet and can be computed from the explicit form of equation (3.11) for an SNREI Earth.  ${}_nU_l^q(r) = {}_nV_l^q(r) = 0$  for toroidal modes ( $q=T$ ), and  ${}_nW_l^q(r) = 0$  for spheroidal modes ( $q=S$ ).  $\nabla_1 \equiv \hat{\theta}\partial_\theta + \csc\theta\hat{\phi}\partial_\phi$ , and  $\hat{r}$ ,  $\hat{\theta}$  and  $\hat{\phi}$  are unit vectors in the spherical coordinate system.  $Y_l^m(\theta, \phi)$  are complex spherical harmonics, completely normalized following the convention in *Edmonds, 1960*:

$$\begin{aligned} Y_l^m(\theta, \phi) = & \frac{(-1)^{l+m}}{2^l l!} \left[ \frac{(2l+1)(l-m)!}{4\pi(l+m)!} \right]^{\frac{1}{2}} \\ & \cdot (\sin\theta)^m \left[ \frac{\partial}{\partial(\cos\theta)} \right]^{l+m} (\sin\theta)^{2l} e^{im\phi}. \end{aligned} \quad (3.13)$$

The inner product by which the eigenfunctions  $\mathbf{x}_m^k$  are normalized is defined by (*Woodhouse, 1980*)

$$\langle k' m' | \rho_0 | k m \rangle \equiv \int_V \rho_0 \mathbf{x}_{m'}^{k'*} \cdot \mathbf{x}_m^k dV = \delta_{kk'} \delta_{mm'} \quad (3.14)$$

where the integration is over the volume  $V$  of the Earth,  $\rho$  is the density distribution in the SNREI Earth, the  $*$  denotes complex conjugation and  $\delta_{kk'}$  and  $\delta_{mm'}$  are Kronecker deltas. Together, all the modes of Earth oscillation form a complete set, so that any vector field  $\mathbf{u}$  may be written as

$$\mathbf{u} = \sum_{k m} |k m\rangle \langle k m | \rho_0 | u \rangle \quad (3.15)$$

### 3.2 Normal Mode Splitting

When considering the realistic aspherical structure of the Earth, the degeneracy of the eigenfrequencies  $\omega_k$  is removed. Considering only first order perturbations to the SNREI Earth, (*Dahlen, 1969, 1974; Woodhouse and Dahlen, 1978; Woodhouse, 1980*), the eigenfunctions and eigenfrequencies of each singlet can be derived using perturbation theory. The perturbed eigenvalue equation to first order written in standard form is

$$[\mathcal{H}_0 + \epsilon \mathcal{H}_1 - (\rho_0 + \epsilon \rho_1) \varpi^2] \mathbf{u} = 0 \quad (3.16)$$

where  $\varpi^2$  is the eigenvalue of the perturbed system, and  $\mathbf{u}$  is the associated eigenfunction.  $\epsilon \mathcal{H}_1$  is the perturbing operator, and  $\epsilon \rho_1$  is the perturbation in density, for small factors  $\epsilon$ .  $\mathbf{u}$  can be expressed following equation (3.15) to obtain

$$\sum_{k m} [\epsilon(\mathcal{H}_1 - \rho_1 \varpi^2) + (\mathcal{H}_0 - \rho_0 \varpi^2)] |k m\rangle \langle k m | \rho_0 | u \rangle = 0 \quad (3.17)$$

By taking the product with  $|k' m'\rangle^*$  and using equation (3.11), we can then integrate over  $V$  for

$$\sum_{k m} \langle k' m' | [\epsilon(\mathcal{H}_1 - \rho_1 \varpi^2) |k m\rangle + \rho_0(\omega_k^2 - \varpi^2) \delta_{kk'} \delta_{mm'}] |k m\rangle \rho_0 |u\rangle = 0. \quad (3.18)$$

The eigenvalue of the perturbed system is approximately equal to that of the eigenvalue of the spherical system, and for multiplets which are well-separated in the frequency band, that is, uncoupled and deemed 'isolated', we can simply consider  $\varpi^2 = \omega_k^2 + \epsilon \omega_k^2$ . The first order terms of equation (3.18) are then

$$\sum_{k m} \langle k' m' | \epsilon(\mathcal{H}_1 - \rho_1 \omega_k^2) |k m\rangle + \rho_0(\omega_k^2 - \varpi^2) \delta_{kk'} \delta_{mm'} |k m\rangle \rho_0 |u\rangle = 0, \quad (3.19)$$

leading to the expression for the perturbation in eigenvalue

$$\epsilon \omega_{kmm'}^2 = \langle k m' | \epsilon(\mathcal{H}_1 - \rho_1 \omega_k^2) |k m\rangle. \quad (3.20)$$

The term on the left hand side of equation (3.20) refers to elements of a  $(2l+1)$  dimensional square matrix of perturbations in eigenvalue  $\omega_k^2$  resulting from the coupling, due to aspherical structure, of singlets  $m$  and  $m'$  belonging to multiplet  $k$ . Each singlet  $|k m\rangle$  in the multiplet  $k$  has an associated eigenvalue  $\omega_k^2 + \epsilon \omega_{kmm}^2$ , and thus the aspherical structure splits the reference degenerate eigenvalue  $\omega_k^2$  for multiplet  $k$  into  $(2l+1)$  eigenvalues associated with multiplet  $k$ .

Relating the small quantity  $\epsilon \rightarrow \delta$ ,  $\epsilon \omega^2 \rightarrow \delta(\omega^2) = 2\omega\delta\omega$ . Likewise,  $\epsilon \mathcal{H}_1$  and  $\epsilon \rho_1$  can be expressed as perturbations to the spherical operator  $\mathcal{H}_0$  and density  $\rho_0$  by  $\epsilon \mathcal{H}_1 \rightarrow \delta \mathcal{H}$  and  $\epsilon \rho_1 \rightarrow \delta \rho$ .

$$\delta \omega_{kmm'} = \langle k m' | \mathbf{H}_{kk} |k m\rangle \quad (3.21)$$



gives the  $(2l + 1)$  square matrix of eigenfrequency perturbations where

$$\mathbf{H}_{kk} \equiv \frac{\delta\mathcal{H} - \delta\rho\omega_k^2}{2\omega_k}. \quad (3.22)$$

### 3.2.1 Splitting of Coupled Multiplets

A set  $K$  of multiplets may couple in the aspherical Earth if the multiplets  $k \in K$  resonate at very similar eigenfrequencies, and if non-zero values of the eigenfunctions of  $k \in K$  overlap in depth (*Dahlen, 1969; Luh, 1973; Woodhouse, 1980*). Then, in the coupled oscillation, the  $k \in K$  multiplets share the same beat frequency  $\omega_K$ , where for each  $k \in K$ ,  $\omega_K^2 - \omega_k^2 = O(\epsilon)$ . In this case, we can write  $\varpi^2 = \omega_K^2 + \epsilon\omega^2$ . In this thesis, we only consider coupling between two modes, i.e.  $k, k' \in K$ , and a more general form of equation (3.20) is

$$\epsilon\omega_{kk'mm'}^2 = \langle k' m' | \epsilon(\mathcal{H}_1 - \rho_1\omega_K^2) | k m \rangle - (\omega_K^2 - \omega_k^2)\delta_{kk'}\delta_{mm'}, \quad (3.23)$$

where for  $k = k'$ , equation (3.23) is reduced to equation (3.20). Then

$$\delta\omega_{kk'mm'} = \langle k' m' | \mathbf{H}_{kk'} | k m \rangle - (\omega_K^2 - \omega_k^2)\delta_{kk'}\delta_{mm'}/2\omega_K \quad (3.24)$$

is the matrix of eigenfrequency perturbations for a coupled multiplet system

where

$$\mathbf{H}_{kk'} \equiv \frac{\delta\mathcal{H} - \delta\rho\omega_K^2}{2\omega_K}. \quad (3.25)$$

The dimension of matrices  $\delta\omega$  and  $\mathbf{H}_{kk'}$  is  $(2l' + 1) \times (2l + 1)$  where the rows are

labeled by  $-l \leq m \leq l$ , and the columns are labeled by  $-l' \leq m' \leq l'$ .

The second term on the right hand side of equation (3.24) is much less than  $O(\epsilon)$ , and therefore may be neglected. Aspherical Earth structure is then related to  $\delta\omega_{kk'mm'} \equiv \langle k' m' | \mathbf{H}_{kk'} | k m \rangle$  by (Woodhouse, 1980)

$$\begin{aligned} \langle k' m' | \mathbf{H}_{kk'} | k m \rangle &\equiv H_{kk'}^{mm'} \\ &= (\Omega m \beta \delta_{ll'} + \varepsilon) \delta_{mm'} + \sum_{s=|l-l'|}^{l+l'} \sum_{t=-s}^s \gamma_{ll's}^{mm't} c_{ll's}^t \end{aligned} \quad (3.26)$$

where

$$c_{ll's}^t = \int_0^a \mathbf{M}_s^{kk'}(r) \cdot \delta \mathbf{m}_s^t(r) r^2 dr - \sum_d H_{sd} \delta h_{sd}^t r^2. \quad (3.27)$$

The first term on the right-hand side of equation (3.26) is the shift due to Coriolis force;  $\Omega$  is the rotational angular velocity and  $\beta$  is the Coriolis splitting parameter.  $\varepsilon$  includes the contribution from the Earth's hydrostatic ellipticity. The coefficient

$$\gamma_{ll's}^{mm't} \equiv \int_0^{2\pi} \int_0^\pi Y_l^{m*}(\theta, \phi) Y_s^t(\theta, \phi) Y_{l'}^{m'}(\theta, \phi) \sin\theta d\theta d\phi, \quad (3.28)$$

where  $Y_l^m(\phi, \theta)$ ,  $Y_{l'}^{m'}(\phi, \theta)$ , and  $Y_s^t(\phi, \theta)$  are spherical harmonic functions. In equation (3.27),  $\delta \mathbf{m}_s^t$  represents the relative perturbation of structure  $\mathbf{m}$  with respect to the reference one-dimensional model.  $\mathbf{M}_s^{kk'}(r)$  represents sensitivity kernels for the modes  $(k, k')$  and  $a$  is the radius of the Earth. Topographical variations are represented by  $\delta h_{sd}^t$ , where the index  $d$  refers to discontinuities within the earth (in our case we consider the sea floor, Moho, 670 km discontinuity, and core-mantle boundary) and  $H_{sd}$  is the associated kernel for the undulation of boundary  $d$ . The extraction of structure variations  $\mathbf{m}$  and boundaries  $d$  in

the mantle from normal mode spectral observations is the motivation of this thesis, while the remaining variables in equation ( 3.26) are considered to be well understood.

The splitting due to Coriolis coupling and the aspherical structure of the Earth's ellipticity of figure are accurately known and can be computed theoretically (*Dahlen, 1968, 1976; Woodhouse and Dahlen, 1978; Woodhouse, 1980*). Eigenfrequency splitting by Coriolis coupling and the Earth's hydrostatic ellipticity of figure is computed to first order from an SNREI Earth model in this study. The expressions for  $\beta$  and  $\varepsilon$  in equation ( 3.26), generalized for coupled multiplets ( $k \neq k'$ ), can be found in *Woodhouse 1980*.

The product of the coefficient  $\gamma_{ll's}^{mm't}$ , and the weighted integral of structure heterogeneity contribute to the eigenfrequency perturbation in the second term in equation ( 3.26). The integral represented by  $\gamma_{ll's}^{mm't}$  (equation 3.28), may also be written in terms of Wigner 3- $j$  symbols (*Edmonds, 1960*, equation [4.6.3])

$$\gamma_{ll's}^{mm't} \equiv \left[ \frac{(2l+1)(2s+1)(2l'+1)}{4\pi} \right]^{1/2} \begin{pmatrix} l & s & l' \\ 0 & 0 & 0 \end{pmatrix} \begin{pmatrix} l & s & l' \\ -m & t & m \end{pmatrix}. \quad (3.29)$$

Symmetry properties of  $\gamma_{ll's}^{mm't}$ , commonly known as Clebsch-Gordon coefficients in quantum mechanics, are well-documented (*eg., Rose, 1957; Edmonds, 1960*). By virtue of the symmetry relation (equation [3.7.6], *Edmonds, 1960*)

$$\begin{pmatrix} l & s & l' \\ m & t & m' \end{pmatrix} = (-1)^{l+s+l'} \begin{pmatrix} l & s & l' \\ -m & -t & -m' \end{pmatrix}, \quad (3.30)$$

it is required that  $(-1)^{l+s+l'} = 1$  for  $m = t = m' = 0$  so that

$$\begin{pmatrix} l & s & l' \\ 0 & 0 & 0 \end{pmatrix} = 0 \quad \text{unless } l + s + l' \text{ is even.} \quad (3.31)$$

The  $\gamma_{ll's}^{mm't}$  coefficients represent the interaction strength between singlets  $|n q l m\rangle$  and  $|n' q' l' m'\rangle$ , coupled by heterogeneity size, which is represented by spherical harmonic coefficient of degree  $s$  and azimuthal order  $t$ . For coupled multiplets  $|n q l\rangle$  and  $|n' q' l'\rangle$ , the relation between  $l, s$ , and  $l'$  required by equation ( 3.31) and vector addition determine the selection rules:

$$|l - l'|, |l - l'| + 2, \dots \leq s \leq \dots, l + l' - 2, l + l'$$

and

$$-s \leq t \leq s.$$

This implies that isolated multiplets ( $k = k'$ ) coupling with themselves then are only sensitive to even harmonic degrees  $s$  of heterogeneity, where  $0 \leq s \leq 2l$ . On the other hand, for multiplets  $k \neq k'$  which resonate at nearly equivalent frequencies, the singlets couple within their own multiplet in addition to cross-coupling with singlets of the nearly resonant multiplet partner. Self-coupling ( $k = k, k' = k'$  within  $K$ ) provides sensitivity to even harmonic degrees  $s$ , and cross-multiplet coupling ( $k \neq k'$  within  $K$ ) may provide additional sensitivity to odd harmonic degrees  $s$  if  $l + l'$  or equivalently,  $|l - l'|$ , is odd.

### 3.3 Spectral Splitting

The contribution of a particular isolated multiplet  $k$  to the observed surface displacement can be written as (*Woodhouse and Girnius, 1982*)

$$u(t) = \Re[\exp(i\omega_k t) \mathbf{R}_k \cdot \exp(i\mathbf{H}t) \cdot \mathbf{S}_k] \quad (3.32)$$

where  $\mathbf{R}_k$  is the receiver vector and  $\mathbf{S}_k$  is the source vector, and  $\omega_k$  is the complex reference frequency of the mode with respect to an SNREI model of the Earth.  $\mathbf{R}_k$  describes the instrument response and location and  $\mathbf{S}_k$  characterizes the excitation of singlets evaluated at the source. These  $(2l+1)$  dimensional vectors may be expressed as

$$\mathbf{R}_k = R_k^m(\theta_r, \phi_r) = \sum_{N=-1}^1 R_{kN} Y_l^{Nm}(\theta_r, \phi_r) \quad (3.33)$$

$$\mathbf{S}_k = S_k^m(\theta_s, \phi_s) = \sum_{N=-2}^2 S_{kN} Y_l^{Nm*}(\theta_s, \phi_s) \quad (3.34)$$

where  $Y_l^{Nm}$  are generalized spherical harmonics (*Phinney and Burridge, 1973*), where  $l$  is the angular order of the multiplet  $k$ ,  $m$  is the azimuthal order  $-l < m < l$ ,  $\theta_r, \phi_r, \theta_s$ , and  $\phi_s$  are the receiver and source colatitudes and longitudes.

In the case where modes are closely spaced in frequency, and their respective eigenfunctions sample similar depths in the Earth, the contribution to the displacement on the surface is formulated as a linear combination of equation(3.32) for each of the multiplets, and there is additional contribution to the seismogram from the cross-multiplet coupling of singlets. We can then express the

seismogram in terms of augmented receiver and source vectors, and the augmented matrix  $\mathbf{H}$  incorporates the contributions from the self-coupling of singlets within each multiplet in diagonal submatrices of  $\mathbf{H}$ , and cross-coupling of singlets between multiplets in the off-diagonal submatrices of  $\mathbf{H}$ :

$$u(t) = [R_k R_{k'}] e^{i \begin{bmatrix} \omega_{kk} + H_{kk} & \omega_{kk'} + H_{kk'} \\ \omega_{k'k} + H_{k'k} & \omega_{k'k'} + H_{k'k'} \end{bmatrix} t} \begin{bmatrix} S_k \\ S_{k'} \end{bmatrix} \quad (3.35)$$

or more explicitly,

$$\begin{aligned} u(t) = & R_k e^{i(\omega_{kk} + H_{kk})t} S_k + R_{k'} e^{i(\omega_{k'k'} + H_{k'k'})t} S_{k'} + \\ & [R_k e^{i(\omega_{kk'} + H_{kk'})t} S_{k'} + R_{k'} e^{i(\omega_{k'k} + H_{k'k})t} S_k]. \end{aligned} \quad (3.36)$$

The splitting matrix  $\mathbf{H}$  is then a  $[(2l+1) + (2l'+1)] \times [(2l+1) + (2l'+1)]$  dimensional complex matrix. Following *Giardini et al., 1988*,

$$\mathbf{H}\mathbf{U} = \mathbf{U}\mathbf{\Omega} \quad (3.37)$$

where  $\mathbf{H}$ ,  $\mathbf{U}$ , and  $\mathbf{\Omega}$  are  $[(2l+1) + (2l'+1)] \times [(2l+1) + (2l'+1)]$  dimensional matrices.  $\mathbf{U}$  is the matrix of eigenfunctions, and  $\mathbf{\Omega}$  is the matrix of eigenfrequency perturbations.

### 3.3.1 Partial Derivatives for heterogeneity

In order to compose the inverse problem for Earth structure, it is necessary to formulate the partial derivatives of the seismogram  $u(t)$  with respect to the

coefficients of structure perturbation,  $m_s^t$ . We first note that equation (3.36) is non-linear in  $\mathbf{H}$ , and from equation (3.26), it follows that  $u(t)$  has a non-linear relationship to the coefficients  $c_{ll's}^t$  as well. First, we derive the linearized expression for  $\partial u(t)/\partial c_{ll's}^t$ , expanded from the treatment of *Giardini et al., 1991*, to include coupled multiplet pairs. The coefficients  $c_{ll's}^t$  in equation (3.27) are linear in structure perturbations  $m_s^t$ , and it is then trivial to compute the partial derivatives relating seismogram to structure perturbations for a linearized, iterative inverse problem.

Using the notation of *Woodhouse and Girnius, 1982*, a wave propagation operator  $\mathbf{P}(\mathbf{t})$  may be defined as  $\mathbf{P}(\mathbf{t}) \equiv e^{i\mathbf{H}t}$ . Taking the first time derivative, and stating initial conditions, we have

$$\frac{d\mathbf{P}(t)}{dt} = i\mathbf{H}\mathbf{P}; \quad \mathbf{P}(0) = \mathbf{I} \quad (3.38)$$

where  $\mathbf{I}$  is the unit matrix. Perturbing this equation, we find a differential equation linear in  $\delta\mathbf{P}(\mathbf{t})$

$$\frac{d\delta\mathbf{P}(t)}{dt} = i\delta\mathbf{H}\mathbf{P}(t) + i\mathbf{H}\delta\mathbf{P}(t); \quad \delta\mathbf{P}(0) = 0, \quad (3.39)$$

the solution to which is

$$\begin{aligned} \delta\mathbf{P}(t) &= \int_0^t (i\delta\mathbf{H}\mathbf{P}(t') + i\mathbf{H}\delta\mathbf{P}(t')) dt' \\ &= \int_0^t \mathbf{P}(t-t') i\delta\mathbf{H}\mathbf{P}(t') dt'. \end{aligned} \quad (3.40)$$

Then using

$$\mathbf{P}(t) = e^{i\mathbf{H}t} = \mathbf{U}e^{i\mathbf{\Omega}t}\mathbf{U}^{-1} \quad (3.41)$$

we can express each element of the matrix in the left hand side of equation (3.40)

as

$$\delta P_{ij}(t) = \sum_{pqmm'} \int_0^t i U_{ip} e^{i\Omega_{pp}(t-t')} U_{pm}^{-1} \delta H_{mm'}^{kk'} U_{m'q} e^{i\Omega_{qq}t'} U_{qj}^{-1} dt'. \quad (3.42)$$

In the case of singlet coupling within an isolated multiplet ( $k = k'$ ), the indices  $-m \leq i, j, p, q \leq m$ , and in the case of non-isolated multiplets ( $k \neq k'$ ), the rows are indexed by  $-m \leq i, p \leq m$  and the columns by  $-m' \leq j, q \leq m'$ .

Taking the derivative of equation (3.42) with respect to  $H_{mm'}^{kk'}$ , and keeping in mind the indexing as described above,

$$\begin{aligned} \frac{\partial \exp(i\mathbf{H}t)_{ij}}{\partial H_{mm'}^{kk'}} &= \sum_{pqmm'} i \int_0^t U_{ip} e^{i\Omega_{pp}(t-t')} U_{pm} U_{m'q} e^{i\Omega_{qq}t'} U_{qj} dt' \\ &= \sum_{pqmm'} i U_{ip} U_{pm}^{-1} U_{m'q} U_{qj}^{-1} \left[ \frac{e^{i\Omega_{qq}t} - e^{i\Omega_{pp}t}}{\Omega_{qq} - \Omega_{pp}} \right]. \end{aligned} \quad (3.43)$$

This leads to a linearized form of equation (3.36):

$$\begin{aligned} \delta u(t) &= \sum_{\zeta=1}^4 \Re \left[ \sum_{pqst} \sum_i r_i U_{ip} \sum_{mm'} U_{pm}^{-1} U_{m'q} \gamma_{ll's}^{mm't} \sum_j U_{qj}^{-1} s_j e^{i\omega_{kk'}t} \right. \\ &\quad \left. \times \frac{e^{i\Omega_{qq}t} - e^{i\Omega_{pp}t}}{\Omega_{qq} - \Omega_{pp}} \delta c_{ll's}^t \right]_{\zeta} \end{aligned} \quad (3.44)$$

where  $\zeta$  indexes over the combinations of mode coupling:  $1 \equiv \langle km|km \rangle$ ,  $2 \equiv \langle k'm'|k'm' \rangle$ ,  $3 \equiv \langle km|k'm' \rangle$ , and  $4 \equiv \langle k'm'|km \rangle$ .

For  $q \neq p$ ,

$$\sum_{pq} \frac{e^{i\Omega_{qq}t} - e^{i\Omega_{pp}t}}{\Omega_{qq} - \Omega_{pp}} = \sum_{pq} \frac{e^{i\Omega_{qq}t}}{\Omega_{qq} - \Omega_{pp}} + \sum_{qp} \frac{e^{i\Omega_{qq}t}}{\Omega_{qq} - \Omega_{pp}} \quad (3.45)$$

For  $q=p$ ,

$$\lim_{\Omega_{qq} \rightarrow \Omega_{pp}} \frac{e^{i\Omega_{qq}t} - e^{i\Omega_{pp}t}}{\Omega_{qq} - \Omega_{pp}} = it e^{i\Omega_{qq}t} \quad (3.46)$$



Rewriting

$$\begin{aligned}
r'_p &= \sum_i U_{ip} r_p \\
s'_q &= \sum_j U_{iq} s_q \\
\gamma'_{pqst} &= \sum_{mm'} U_{pm}^{-1} U_{m'q} \gamma_{ll's}^{mm't},
\end{aligned} \tag{3.47}$$

equation (3.44) then becomes

$$\begin{aligned}
\delta u(t) &= \Re \sum_{\zeta} \left[ \omega_{kk'} e^{i\omega_{kk'} t} \sum_{st} \delta c_{ll's}^t \sum_q e^{i\Omega_{qq} t} \right. \\
&\times \left. \left( \sum_{p \neq q} \frac{r'_p s'_q \gamma'_{pqst} + r'_q s'_p \gamma'_{qpst}}{\Omega_{qq} - \Omega_{pp}} + i t r'_q s'_p \gamma'_{qqst} \right) \right]_{\zeta},
\end{aligned} \tag{3.48}$$

and the partial derivative  $\partial u(t)/\partial c_{ll's}^t$  can readily be obtained from equation (3.48).

The linearity of  $c_{ll's}^t$  to the perturbations in structure (equation (3.26)) then allows for straight forward formulation of the partial derivatives  $\partial c_{ll's}^t/\partial m_s^t$ .

By combining the two partial derivatives  $\partial u(t)/\partial c_{ll's}^t$  and  $\partial c_{ll's}^t/\partial m_s^t$ , the linearized partial derivative

$$\frac{\partial u(t)}{\partial m_s^t} = \frac{\partial u(t)}{\partial c_{ll's}^t} \frac{\partial c_{ll's}^t}{\partial m_s^t} \tag{3.49}$$

is formed to relate the observed seismogram directly to the heterogeneity in the Earth. The product of these two sets of partial derivatives allows us to invert for structure directly from the seismograms, which sets this study apart from work by other normal mode groups (*Resovsky and Ritzwoller, 1999b; Ishii and Tromp, 1999*) who solve for  $c_{sl'l'}$  coefficients for a number of modes separately,

and then combine these coefficients to perform a linear inversion for structure. The advantage gained from the direct inversion approach is that the inverse problem is more regularized, by which we mean that all the mode data spectra are inverted simultaneously for a consistent model of Earth structure.

### 3.4 Normal Mode Kernels

#### 3.4.1 Kernels for volumetric heterogeneity

Heterogeneity in the Earth can be described by different sets of physical properties, and specifically for seismology, Earth structure may be characterized by its elastic properties and density. Neglecting the effects of anisotropy, the perturbations in normal mode eigenfrequencies have been specified by perturbations in shear modulus  $\delta\mu(r, \theta, \phi)$ , bulk modulus  $\delta\kappa(r, \theta, \phi)$ , density  $\rho(r, \theta, \phi)$ , and the boundary topography  $\delta h(\theta, \phi)$  in *Woodhouse, 1980*.

We choose to describe the heterogeneity in terms of perturbations in compressional velocity,  $v_P$ , shear velocity,  $v_S$ , and density  $\rho$  so that the term  $\delta\mathbf{m}_s^t$  in equation ( 3.27) is

$$\delta\mathbf{m}_s^t = \left[ \frac{\delta v_{Ps}^t}{v_P}, \frac{\delta v_{Ss}^t}{v_S}, \frac{\delta \rho_s^t}{\rho} \right] \quad (3.50)$$

where the numerators are spherical harmonic components of angular degree  $s$  and azimuthal order  $t$  of the perturbation, and the denominators are evaluated at the relevant depth in the spherical reference model. When the effects of attenuation are included,  $\delta v_{Ps}^t$  and  $\delta v_{Ss}^t$  may be complex.

For this description of heterogeneity, the kernel  $\mathbf{M}_s^{kk'}(r)$  can then be defined as

$$\mathbf{M}_s^{kk'}(r) = [P_{kk'}^s(r), S_{kk'}^s(r), R_{kk'}^s(r)]. \quad (3.51)$$

The kernels weight, as a function of radius  $r$ , the contribution which heterogeneity of degree  $s$  gives to the eigenfrequency perturbation. Kernels  $P_{kk'}^s(r)$ ,  $S_{kk'}^s(r)$ , and  $R_{kk'}^s(r)$  are functions of the eigenfunctions of the coupling multiplets  $(k, k')$  for the spherical reference model (equation (3.12)), and can be formulated in terms of the equations (A36), (A37), and (A38) given in *Woodhouse, 1980*, for which the kernels are cast for bulk modulus  $\kappa$ , shear modulus  $\mu$  and density  $\rho$ , are, respectively:

$$\begin{aligned} \omega_{kk'} P_s^{kk'}(r) &= 2v_P \rho K_s \\ &= 2\left[\left(\kappa + \frac{4}{3}\mu\right)\rho\right]^{1/2} K_s \end{aligned} \quad (3.52)$$

$$\begin{aligned} \omega_{kk'} S_s^{kk'}(r) &= 2v_S \rho \left(M_s - \frac{4}{3}K_s\right) \\ &= 2[\mu\rho]^{1/2} \left(M_s - \frac{4}{3}K_s\right) \end{aligned} \quad (3.53)$$

$$\begin{aligned} \omega_{kk'} R_s^{kk'}(r) &= \left[(v_P^2 - \frac{4}{3}v_S^2)K_s + v_S^2 M_s + R_s^{(1)}\right] \\ &= \frac{1}{\rho}(\kappa K_s + \mu M_s + \rho R_s^{(1)}) \end{aligned} \quad (3.54)$$

We have replaced  $l''$ , in the notation of *Woodhouse, 1980*, by  $s$  here, and the dependence of  $K_s$ ,  $M_s$  and  $R_s$  on radius  $r$  is understood.

### 3.4.2 Kernel coefficients for boundary topography

The undulations  $\delta h_{sd}^t$  of a boundary  $d$  at radius  $r$  give rise to eigenfrequency perturbations through the kernel coefficients evaluated at the boundary radius. If  $\delta h_{sd}^t$  in equation (3.26) is defined as topography normalized by the boundary radius, then the corresponding kernel can be expressed as

$$\begin{aligned}\omega_{kk'} H_s &= r\rho[(v_P^2 - \frac{4}{3}v_S^2)\tilde{K}_s + v_S^2\tilde{M}_s + R_s^{(1)}]_-^+ \\ &= r[\kappa\tilde{K}_s + \mu\tilde{M}_s + \rho_0 R_s^{(1)}]_-^+\end{aligned}\tag{3.55}$$

where  $\tilde{K}_s$ ,  $\tilde{M}_s$ , and  $R_s^{(1)}$  are given in (A27), (A28), and (A38) of *Woodhouse, 1980*, respectively. The notation  $[\cdot]_-^+$  is used to signify the discontinuity jump of the enclosed quantity across the boundary, where the positive contribution corresponds to the positive  $\hat{\mathbf{r}}$  side of the boundary.

## Chapter 4

### Inverse Theory

The physical properties of the Earth's interior cannot always be measured directly. Assuming that a mathematical representation is valid, inverse theory is used to estimate the model parameter values, given a set of data and a model theory. Also encompassed in inverse theory is the estimation of resolution and uncertainty in model parameters. The inverse formulation for the problem specified in this thesis, and solution evaluation schemes are discussed below.

#### 4.1 Formulation of the Inverse Problem

In this thesis, the three-dimensional structure in density, and compressional and shear velocity are the physical properties which we wish to quantify. From a collection of observed seismograms  $u(t)$ , we invert for three-dimensional structure in compressional velocity  $\delta \ln \alpha_s^t(r)$ , shear velocity  $\delta \ln \beta_s^t(r)$ , density  $\delta \ln \rho_s^t(r)$  and boundary undulations  $\delta h_{st}^d$ . The digital seismograms  $u(t)$  are discretely tabulated, and the solutions for three-dimensional structure are discretized in the

form of polynomial expansion coefficients, as described in Section 5.5. Defining  $\mathbf{m}_s^t(r)$  to be the vector of three-dimensional model structure coefficients, it is clear from equation (3.49) that solving for  $\mathbf{m}_s^t(r)$  from the collection of data,  $u(t)$ , is a non-linear inverse problem.

We seek solutions for our model parameters  $\mathbf{m}$  from the following relation:

$$\mathbf{d} = \mathbf{f}(\mathbf{m}) + \mathbf{e} \quad (4.1)$$

where  $\mathbf{d}$  is the  $N$ -dimensional vector of data,  $\mathbf{f}$  is a non-linear function,  $\mathbf{m}$  is the  $M$ -dimensional vector of model parameters, and  $\mathbf{e}$  is the vector of errors in  $\mathbf{d}$ .

Assuming that the noise in the data has a white spectrum, errors in  $\mathbf{e}$  are then normally distributed with a zero mean and a variance  $\sigma_e^2$ . The data covariance matrix  $\mathbf{C}_e$  is then a matrix in which the diagonal elements are equal to  $\sigma_e^2$ . We also make the assumption that the probability distributions of the model parameters in  $\mathbf{m}$  are Gaussian. The variables in  $\mathbf{m}$  then have *a priori* mean values  $\mathbf{m}_0$ , and covariance defined in the matrix  $\mathbf{C}_m$ .  $\mathbf{m}_0$  represents values of a starting model which we expect values of our final model to be close to, and the covariance matrix  $\mathbf{C}_m$  reflects the strength of our expectations. Combining the probability distribution of errors and *a priori* probability distribution of model parameters with the our model equation  $\mathbf{d}=\mathbf{f}(\mathbf{m})$ , the probability distribution of the model vector  $\mathbf{m}$  is

$$P(\mathbf{m}) \propto \exp\left[-\frac{1}{2}(\mathbf{d} - \mathbf{f}(\mathbf{m}))^T \mathbf{C}_e^{-1}(\mathbf{d} - \mathbf{f}(\mathbf{m}))\right] \times$$

$$\exp\left[-\frac{1}{2}(\mathbf{m} - \mathbf{m}_0)^T \mathbf{C}_m^{-1}(\mathbf{m} - \mathbf{m}_0)\right]. \quad (4.2)$$

The maximum likelihood solution to  $\mathbf{d}=\mathbf{f}(\mathbf{m})+\mathbf{e}$  is then the minimum of the argument of the exponential in (4.2). The objective function which must be minimized is given by

$$\Phi(\mathbf{m}) = (\mathbf{d} - \mathbf{f}(\mathbf{m}))^T \mathbf{C}_e^{-1}(\mathbf{d} - \mathbf{f}(\mathbf{m})) + (\mathbf{m} - \mathbf{m}_0)^T \mathbf{C}_m^{-1}(\mathbf{m} - \mathbf{m}_0). \quad (4.3)$$

The minimum of the objective function  $\Phi(\mathbf{m})$  is found by applying the following in an iterative fashion:

$$\mathbf{m}_{i+1} = \mathbf{m}_i + (\mathbf{A}_i^T \mathbf{C}_e^{-1} \mathbf{A}_i + \mathbf{C}_m^{-1})^{-1} [\mathbf{A}_i^T \mathbf{C}_e^{-1}(\mathbf{d} - \mathbf{f}(\mathbf{m}_i)) - \mathbf{C}_m^{-1}(\mathbf{m}_i - \mathbf{m}_0)] \quad (4.4)$$

where  $\mathbf{A}_i$  is an  $N \times M$  matrix of partial derivatives

$$\mathbf{A}_i = \left[ \frac{\partial \mathbf{f}(\mathbf{m})}{\partial \mathbf{m}} \right]_{\mathbf{m}=\mathbf{m}_i}, \quad (4.5)$$

and is expressed explicitly by equation (3.49), and  $i$  is the index of iteration.

To avoid obtaining solutions in  $\mathbf{m}$  which may be biased towards pre-existing three-dimensional models, particularly by seismic velocities models derived from higher frequency data, the *a priori* model vector  $\mathbf{m}_0$  has been set to zero, *i.e.*, PREM, for the inversions in this study. We have been seeking solutions for perturbations from a spherical model of the Earth, namely PREM (*Dziewonski and Anderson, 1981*), in order to investigate the heterogeneities to which the normal mode spectra are sensitive. The inversion relation for the model thus

becomes

$$\mathbf{m}_{i+1} = \mathbf{m}_i + (\mathbf{A}_i^T \mathbf{C}_e^{-1} \mathbf{A}_i + \mathbf{C}_m^{-1})^{-1} [\mathbf{A}_i^T \mathbf{C}_e^{-1} (\mathbf{d} - \mathbf{f}(\mathbf{m}_i)) - \mathbf{C}_m^{-1} \mathbf{m}_i]. \quad (4.6)$$

In what follows, we discuss the model covariance matrix  $\mathbf{C}_m$ , and the error estimates which constitute the diagonal of the matrix  $\mathbf{C}_e$ .

## 4.2 Model Covariance Matrix

The normal modes used in this study sample the mantle structure given by the model kernel sensitivity (equations (3.53)-(3.54)). For each mode, there are spectral measurements from a number of stations and events. We have required that the dimension of the model vector be inferior to the dimension of the data vector to ensure that our inversions are not underdetermined. However, the model parameterization has global extent while the modes do not have uniform sensitivity throughout the depths in the mantle, as discussed in Section 5.5. Also, our mode data set primarily has sensitivity to even degrees  $s$  of heterogeneity, the details of which will be outlined in Section 5.5.1. This data coverage, for the model parameterization we chose, defines a mixed-determined inverse problem, and we wish to determine our solutions in terms of minimizing the prediction error  $\mathbf{e} = \mathbf{d} - \mathbf{f}(\mathbf{m})$  and solution length  $\mathbf{L} = \mathbf{m} - \mathbf{m}_0$ , in which we impose *a priori* assumptions and/or constraints about the behavior of the solution model parameters  $\mathbf{m}$  with respect to a starting model  $\mathbf{m}_0$ . The *a priori* information is introduced in the model covariance matrix  $\mathbf{C}_m$ , and imposed on



the model parameters in the form  $\mathbf{m}^T \mathbf{C}_m^{-1} \mathbf{m}$  (*Tarantola and Valette, 1982; Li and Romanowicz, 1996*).

Following the description in *Li and Romanowicz, 1996*, we specify the elements of model vector  $\mathbf{m}$  as coefficients of polynomial expansions laterally and radially in the following fashion:

$$\frac{\delta m(r, \theta, \phi)}{m(r)} = \sum_p^{pmax} \sum_s^{smax} \sum_{t=-s}^s {}_p m_s^t f_p(r) Y_s^t(\theta, \phi), \quad (4.7)$$

where  ${}_p m_s^t$  are coefficients of expansion for radial functions  $f_p(r)$ , and spherical harmonics  $Y_s^t(\theta, \phi)$ . We can then define the model covariance matrix  $\mathbf{C}_m$  so that  $\mathbf{m}^T \mathbf{C}_m^{-1} \mathbf{m}$  has the form

$$\begin{aligned} \mathbf{m}^T \mathbf{C}_m^{-1} \mathbf{m} = & \int \int \left[ \eta_1 m^2 + \eta_2 \left( \frac{\partial m}{\partial r} \right)^2 + \eta_3 \left( \frac{\partial^2 m}{\partial r^2} \right)^2 + \eta_4 |\nabla_1 m|^2 \right] dr d\Omega \\ & + \int [\eta_{5i} (\delta r_i)^2 + \eta_{6i} |\nabla_1 r_i|^2] d\Omega. \end{aligned} \quad (4.8)$$

The  $\eta_1$  term penalizes the amplitudes of the model. Values for  $\eta_1$  are located along the diagonal of the model covariance matrix. The  $\eta_2$  and  $\eta_3$  terms impose radial smoothness, and  $\eta_4$  terms require horizontal smoothness. Imposing  $\eta_2, \eta_3$ , and  $\eta_4$  terms correspond to placing damping values in the off-diagonal elements of  $\mathbf{C}_m$ , corresponding to covariance between parameters. The term  $\eta_{5i}$  reduces the amplitudes of specific boundary undulations  $i$ , and  $\eta_{6i}$  requires horizontal smoothness on the boundaries. We find that the terms  $\eta_{5i}$  and  $\eta_{6i}$  have interchangeable effects on the boundary amplitudes.

### 4.3 Error Estimates and Model Significance

Uncertainty in the mode spectral measurement can be estimated by considering the noise floor of the seismic trace, the time window chosen before applying the Fourier transform which affects the signal power and resolution, and the frequency window bounds for each spectral measurement, which may incorporate signal from neighboring modes.

There are approximations imposed on the theoretical formulation which we employ, and they further limit the accuracy of the tomographic technique. These approximations in the theory include utilizing a spherically stratified elastic reference Earth model (e.g.. PREM) and extending the representation of the spherical structure to perturbations of only first order. The eigenfunctions and reference eigenfrequencies are computed from the spherically stratified elastic Earth model. Accuracy in spectra prediction could be increased by applying higher order perturbation theory (*eg. Lognonné and Romanowicz, 1990*), computing reference eigenfunctions and eigenfrequencies from a 3-D model, and updating the reference eigenfunctions and eigenfrequencies with each iteration of inversion for 3-D structure until convergence is reached ( *Clévéde and Lognonné, 1994*). This higher order method is computationally laborious, but would allow for wave propagation effects to be modelled such as focusing and defocusing due to 3-D structure, which we here neglect. We also neglect departures from a simple Q-model as described by PREM. By choosing a time window for the seismic

trace which does not exceed 1.1 Q-cycles (*Dahlen, 1982*) we assume, however, that spectral peak broadening is dominated by 3D elastic effects.

For a perfect model  $\mathbf{m}_\oplus$  of the Earth, the measurement error  $\sigma_e^2$  represents the difference between our ability to predict the spectrum from the theory and the observed spectrum. We can define  $\varepsilon$  as some percentage of noise with respect to the observed data. Then, we can consider that the diagonal of the matrix  $\mathbf{C}_e$  is populated by

$$\sigma_e^2 = \varepsilon \mathbf{d}^T \mathbf{d} = (\mathbf{d} - \mathbf{f}(\mathbf{m}_\oplus))^T (\mathbf{d} - \mathbf{f}(\mathbf{m}_\oplus)) \quad (4.9)$$

We assume that the measurement error is at least as good as what we can predict from theory. From spectral records of well-excited modes in which noise is so minimal as to appear absent, we find that this error is about 1% of the size of the record, that is,  $\varepsilon=0.01$ .

The residual variance ratio of squared misfit to squared data is defined as follows:

$$\zeta^2 = \frac{(\mathbf{d} - \mathbf{f}(\mathbf{m}))^T (\mathbf{d} - \mathbf{f}(\mathbf{m}))}{\mathbf{d}^T \mathbf{d}} \quad (4.10)$$

Since the number of model parameters varies between experiments, it is necessary to take into account  $\nu = N - M$ , the number of degrees of freedom, when considering fits to the data. An *a posteriori* estimation can be made of the errors and used to assess the significance of a model, with respect to the number of

model parameters  $M$ . The data variance  $\sigma_d^2$  can be computed by

$$\sigma_d^2 = \frac{(\mathbf{d} - \mathbf{f}(\mathbf{m}))^T (\mathbf{d} - \mathbf{f}(\mathbf{m}))}{N - M} \quad (4.11)$$

For two different realizations,  $M_1$  and  $M_2$ , of the  $N$  data, if  $M_2$  gives a better fit than  $M_1$ , then the F-ratio defined by  $\sigma_{d1}^2/\sigma_{d2}^2$  is greater than 1.

## Chapter 5

# Heterogeneity in the Earth from Normal Mode Spectra

### 5.1 Abstract

Mantle heterogeneity from normal mode studies has been generally derived from "splitting coefficients", which represent an integration, over depth, of the lateral heterogeneity weighted in depth by the mode's sensitivity. The splitting coefficients, measured from individual mantle modes from observed spectra, are then inverted for mantle structure from this linear relationship. In contrast, we forego this intermediate stage of solving for splitting coefficients and invert directly for mantle structure from the spectral data for a sweep of mantle modes. In this manner, the inverse problem for structure becomes more constrained than the dual-stage inversion approach.

Previous models determined from normal mode data were parameterized in terms of  $\delta \ln V_s$ , where aspherical structure in  $V_p$  and  $\rho$  were scaled to  $V_s$  structure, based on proportionality constants from mode studies . We demonstrate

that this assumption is inadequate, and by preserving it, the final S-wave velocity model is contaminated by P-wave velocity and density structure. By setting the scaling relationships free, the model solutions resulting from independently and jointly inverting for  $\delta \ln V_s$ ,  $\delta \ln V_p$ , and  $\delta \ln \rho$  improve the correlation of S-wave velocity models with the existing Berkeley model derived from surface wave and body wave studies. We present and discuss our models of  $V_s$ ,  $V_p$  and density ( $\rho$ ) perturbations in the mantle. The  $V_s$  and  $V_p$  models compare well with results from other studies. The density model is consistently robust, presents features in the mantle which are in accordance with interpretations of denser slabs sinking in the mantle in the circum-Pacific region. A reliable heterogeneous mantle density model would provide a significant contribution to our understanding of mantle convection.

## 5.2 Introduction

Observations of the Earth's free oscillations have been a valuable complement to seismic body and surface wave data in constraining material properties and their lateral variations in the deep Earth. For example, normal mode data provided the first confirmation of the solidity of the inner core (Dziewonski, 1971). Along with the mass and moment of inertia of the earth, they provide the best constraints on the radial density distribution (e.g. *Masters and Gubbins, 1979; Bolt 1972; Dziewonski and Anderson, 1981; Kennett, 1998*). Normal mode split-

ting data have been used to infer the patterns of low degree heterogeneity in the mantle (*Woodhouse and Giardini, 1985; Ritzwoller et al., 1986,1988; Giardini et al., 1987; Li et al., 1991*). They have also been incorporated, along with other data sets, into recent 3D tomographic mantle models to constrain the lowest degree structure (e.g. *Masters et al., 1996; Resovsky and Ritzwoller, 1999b*). The analysis of modes sensitive to core structure has also lead to constraints on inner core anisotropy (e.g. *Woodhouse et al., 1986; Li et al., 1991; Tromp, 1995; Romanowicz et al., 1996; Durek and Romanowicz, 1999*).

While in principle mantle mode data provide information on the  $V_s$ ,  $V_p$  and  $\rho$  in the mantle, the sensitivity to  $V_s$  is dominant, and most studies to-date have assumed an a-priori scaling between the 3 elastic parameters, and inverted for  $V_s$  alone (*Giardini et al., 1987; Li et al., 1991a; Resovsky and Ritzwoller, 1998*). In particular, the density structure is thought to be rather poorly resolved. On the other hand, several studies have shown that the assumption of proportionality between  $V_p$  and  $V_s$  breaks down in the mid-mantle, based on the comparison of  $V_p$  and  $V_s$  models derived from P and S travel time data respectively, or the simultaneous inversion of such data (*Robertson and Woodhouse, 1995,1996; Vasco and Johnson, 1998*). Cast in terms of bulk modulus  $\kappa$  and shear modulus  $\mu$ , instead of seismic velocities, such comparisons indicate anticorrelation in the lowermost mantle (*Su and Dziewonski, 1997*).

With the accumulation of high quality data from global digital seismic net-

works, and the recent occurrence of several very large deep earthquakes (in particular the Mw 8.2 06/09/94 Bolivia, and Mw 8.3 10/10/94 Kurile events), a new data set, greatly improved in quality, is currently available (e.g. *Resovsky and Ritzwoller, 1995; He and Tromp, 1997*) and has been used to improve 3D models of the mantle (e.g. *Resovsky and Ritzwoller, 1999b; Ishii and Tromp, 1998; Kuo et al., 1998*). In what follows, we describe our efforts in this direction, using a somewhat different inversion approach from other studies, and a data set of spheroidal mode spectra.

Most normal mode inversions are cast in terms of a two-step formalism, in which "splitting functions" (*Woodhouse et al., 1986*) are first computed for each mode in the data set. In the second step, splitting functions are simultaneously inverted for the distribution of elastic parameters with depth. This is similar to the standard phase-velocity inversion procedures for surface waves. Such a methodology is convenient, since the 2nd step is linear, and rapidly performed. However, there are some issues about the accuracy and uniqueness of the splitting function coefficients obtained in the first, non-linear step (eg. *Mégnin and Romanowicz, 1995*). The splitting functions may depend on the starting model and may not be completely compatible with a unique earth model. Following *Li et al (1991a)*, and *Durek and Romanowicz (1999)*, we have opted for a direct, one step method, which inverts normal mode spectra directly for 3D earth structure. While more time consuming, this approach is more internally consistent.



Also, most studies include only isolated modes in the spectral representation of seismograms, and the resulting 3D earth models therefore only include even-order terms of lateral heterogeneity (*Woodhouse, 1983; Romanowicz, 1987; Resovsky and Ritzwoller, 1995*). We allow for coupling between two nearby modes in our formalism and apply it to several mode pairs. As shown by *Resovsky and Ritzwoller (1995)*, this has several advantages: (1) Reducing the bias introduced by an isolated mode approximation when 2 modes are close in frequency, therefore increasing the available mode data set, (2) adding sensitivity to odd-order structure.

Using this approach, we have performed inversions in which we simultaneously solve for  $Vs$ ,  $Vp$ ,  $\rho$  structure up to degree 4 in the mantle, for both even and odd degrees. In what follows we present our data set and mantle models, and we discuss the resolution achieved in the different elastic parameters.

### 5.3 Data selection

We have extracted high quality very long period data from GSN/IRIS and Geoscope stations for events listed in Table 1. Events were selected according to their size ( $M_0 \geq 5 \times 10^{20}$  Nm) and their occurrence preceding and following a relatively quiet period in seismicity, so that about 125 hours of data could be obtained from each record, free of perturbations from major aftershocks or other earthquakes with  $M_w \geq 6.5$  ( $M_0 \geq 7 \times 10^{18}$  Nm ). Only vertical component

Table 5.1: Earthquake event information

Date	Moment ( $\times 10^{20}$ Nm)	$M_w$	Depth (km)	Region
03/09/94	3.5	7.63	564	Fiji Islands
06/09/94	30.5	8.26	637	Northern Bolivia
10/04/94	33.9	8.29	33	Kurile Islands
07/30/95	13.8	8.03	47	Northern Chilean Coast
10/09/95	13.3	8.02	49	Coast Near Jalisco, Mexico
01/01/96	8.8	7.90	33	Minahassa Peninsula
02/17/96	27.5	8.23	33	West Irian Region
06/17/96	8.2	7.88	587	Flores Sea

records were considered (spheroidal modes only). Deep events ( $h > 200$  km) were favored, since they excite mode branches sensitive to very deep structure better than shallow earthquakes of the same size.

Each time domain record was edited to remove glitches as well as tides, the latter using an order-50 Legendre polynomial fit (*Bohn, 1994*). In addition to removing the tidal signal, this also removed the mean and trend of the data. Small events and aftershocks were deleted from the traces, which were padded up using linear interpolation. If, in total, more than  $\sim 1$  hour of data required adjustment, the record was discarded. The edited and cleaned selected traces were deconvolved to ground acceleration, and a tapered band-pass filter was applied. The records were then Fourier transformed using a length of record determined by trial and error to optimize the signal to noise ratio and the isolation from neighboring modes. When using a Hann window, the duration is typically targeted to be about 1.1 Q-cycles of the mode (*Dahlen 1982*) to

optimize the estimation of frequencies and decay rates of well-isolated modes. Some target multiplets are close in frequency to low-Q neighbors, and it is advantageous to initiate the Hann window a few hours after the origin time of the event in order to allow the neighboring modes to decay and bring out the signal amplitude of the target mode. The traces are then padded with zeroes before the application of a fast Fourier transform algorithm to the frequency domain. The frequency window limits are chosen for each mode, and do not vary between stations and events.

Synthetic time-domain traces were calculated using the 3D SH velocity model SAW12D (*Li and Romanowicz, 1996*), and source characteristics from the CMT catalog (*eg. Dziewonski et al., 1995*) were assumed in the forward modeling of the traces. For each trace, the same editing, windowing, and filtering algorithms as used for the data were applied to the synthetic traces to compute synthetic spectra. The synthetics were compared with the data to look for anomalous amplitudes which could be attributed to systematic errors, such as inaccurate instrument response functions. However, the misfit of the data compared to the spectral prediction from the 3D model was not a strong factor in selecting spectra, so as not to introduce potential bias towards the initial model. During the data selection process, the spectra of  $V_s$  dominant modes, when displayed in comparison with synthetic spectra computed from an S-velocity model, generally have smaller misfit values than P-velocity sensitive modes. Choosing spectra for

minimal misfit to spectra derived from a model prediction will tend to produce a final model which is very highly correlated to the model used for prediction. This is done in practice in many types of inversions in order to quickly stabilize the solution. We have found that our direct inversion method is very stable and independent of the starting model, whether it is a spherically symmetric model such as PREM (*Dziewonski and Anderson, 1981*), or a 3D  $V_s$  model such as SAW12D (*Li and Romanowicz, 1996*). Structure in  $V_p$  and  $\rho$  not proportional to  $V_s$ , such as can be predicted from SAW12D, will be lost if the criterion of minimal misfit to spectral prediction is emphasized in data selection.

We analyze the vertical component spectra of spheroidal mantle modes whose eigenfunctions primarily exhibit particle motion in the mantle ( $_0S$ ,  $_1S$ ,  $_2S$ ,  $_4S$ ,  $_5S$  branches, and a few in the  $_6S$ ,  $_7S$ ,  $_8S$  branches). Modes with significant displacement in the core are not included in this study, although some mantle modes in our data set have some sensitivity to outer core structure. The effect of outer core sensitivity on our models of mantle structure is minimal, and this is consistent with conclusions of *Giardini et al. 1987*. Models which include core modes and parameterization in the outer core will be described in detail in a future paper. Below 5 mHz, the mantle modes in our study are well-isolated in frequency, which minimizes contamination by neighboring modes. On the other hand, our analysis code is capable of taking into account the more complex effects of 3-D structure on the spectra of coupled mode pairs. In total, we have

chosen 30 isolated mantle modes and 7 coupled mantle mode pairs, amounting to a total of 44 spheroidal mantle modes, and spectra from a total of 2757 individual seismograms. From each spectrum, about  $\sim 10 - 20$  data points are used.

## 5.4 Inversion Procedure

As seen from equation (3), solving for 3D structure using normal mode observations is a non-linear inverse problem. The relation between the structure  $\frac{\delta \mathbf{m}}{\mathbf{m}}(r, \theta, \phi) = (\frac{\delta V_p}{V_p}(r, \theta, \phi), \frac{\delta V_s}{V_s}(r, \theta, \phi), \frac{\delta \rho}{\rho}(r, \theta, \phi))$  and the splitting coefficients  $c_s^t$  is linear, and the corresponding partial derivatives are readily obtained. The derivation of partial derivatives of the seismogram  $u(t)$  with respect to  $c_s^t$ 's follow that of the case for isolated modes, such as in *Giardini et al. 1988*, but includes the case of coupled modes in which  $\mathbf{H}$  is augmented by cross-coupling terms. The product of these two sets of partial derivatives allows us to invert for structure directly from the seismograms, which sets this study apart from work by other normal mode groups (*Resovsky and Ritzwoller 1999b*, and *Ishii and Tromp 1997, 1998, 1999*) who solve for  $c_s^t$  coefficients for a number of modes, and then use these coefficients to perform a linear inversion for structure.

The expressions for the partial derivatives can be found in *Durek & Romanowicz (1999)*. We employ an iterative inversion scheme which minimizes the objective function

$$\Phi(m) = (d - f(m))^T C_e^{-1} (d - f(m)) + m^T C_m^{-1} m. \quad (5.1)$$

$d - f(m)$  is the difference between synthetic spectra  $f(m)$  related non-linearly to the model parameters  $m$ , and the data  $d$  spectra.  $C_e^{-1}$  is the data covariance matrix. The noise, excitation of modes, and contamination of spectra by neighboring modes are assessed during data selection, discarding undesirable spectra. The data are weighted by the fractional amplitude of the data per mode over the total amplitude of all the data:

$$w_m = \sqrt{\frac{\frac{1}{N_{stn}} \sum_i^{N_{stn}} d_i^{m\,2}}{\frac{1}{N_m} \frac{1}{N_{stn}} \sum_m^{N_m} \sum_j^{N_{stn}} d_j^{m\,2}}} \quad (5.2)$$

where  $w_m$  is the weight for mode  $m$ ,  $d_{i,j}^m$  is the spectrum of mode  $m$  at each station  $i, j$  over  $N_{stn}$  stations, and  $N_m$  is the total number of modes in the data set. In this manner, the modes which are strongly excited will contribute more to the model than weakly excited modes. *Li et al. (1991a)* measured the signal-to-noise ratio of each trace from a quiescent time window before each event to compose the  $C_e^{-1}$  matrix. Other mode studies have used an *a posteriori* weighting scheme in which the data are weighted according to the misfit to the previous iteration (*Resovsky & Ritzwoller, 1998; He & Tromp, 1996*). The consequence of this *a posteriori* weighting scheme is that the final result could be biased towards the starting model.

The model covariance matrix  $C_m^{-1}$  represents a priori constraints, such as model size and smoothness. The elements of  $C_m$  can be computed from imposed

damping parameters, and a discussion of this can be found in *Li & Romanowicz (1996)*. There exists a trade-off between the variances of final models and damping parameter values used in the inversion. Damping parameter values are thus selected in the vicinity of the point at which the variance versus damping parameter curve flattens out.

### 5.4.1 Starting model

It is a common procedure to use a starting model of heterogeneity in the inversion process to quickly stabilize the solution, assuming that the starting model is already close to the minimum in misfit-space. When using a laterally heterogeneous starting model, we have employed the following schemes:

1. in inversions for a  $V_s$  model, either PREM, or models of heterogeneity in  $V_s$  from body and surface wave studies were used as starting models.
2. for a  $V_s + n$ -parameter models, where  $n = V_p, \rho$ , two schemes were undertaken:
  - (a) scaling relationships between  $V_s$  and  $n$  were used to calculate the heterogeneities in  $n$ , or
  - (b)  $V_s$  models were used as starting models and no aspherical structure in  $V_p$  or  $\rho$  was assumed.

We find that our final models are independent of the starting model used in the inversion, whether we choose a spherically averaged model such as PREM as starting model, or a laterally heterogeneous model, such as SAW12D or S12WM13 (*Su et al., 1994*) for  $V_s$ , and whether the starting  $V_p$  and  $\rho$  perturbations are assumed to be proportional to those of  $V_s$ , or are initially set to PREM. For either spherical or laterally heterogeneous starting models, our inversions converge after  $\sim 3$  iterations and produce final models which are highly correlated in depth with each other. For this reason, we have adopted PREM as our starting model for  $V_s$ ,  $V_p$ , and  $\rho$  to obtain models of heterogeneity in the absence of *a priori* knowledge of aspherical structure.

### 5.4.2 Model Corrections

As our goal is to study the effects of volumetric mantle heterogeneity on the eigenfrequency spectra of normal modes, we must consider contributions to multiplet splitting other than those from mantle heterogeneity. These include the hydrostatic ellipticity and rotation of the Earth, and crustal structure. We account for these by forward modeling their effects on spectral splitting. Spectral splitting of isolated and coupled multiplets as a result of the rotation of the Earth and consequently hydrostatic ellipticity are calculated from *Woodhouse 1980* and are incorporated into  $\alpha$  of equation 1. Splitting by heterogeneity of the crust is computed by considering the last term in equation 2 for models of



surface and Moho boundary undulations from SAW12D.

## 5.5 Model Parameterization

### 5.5.1 Sensitivity to wavelength of structure

Before exploring the spatial parameterization of our models, we consider the sensitivity of the modes used in our data set. For spheroidal modes, the sensitivity to harmonic degree  $s$  structure goes as, in general,  $|l - l'| < s < l + l'$  and is governed by the coefficient  $\gamma_{ll's}^{mm't}$  which is non-zero for even values of the sum  $l + l' + s$ . The value of  $\gamma_{ll's}^{mm't}$  indicates the strength of coupling between singlets. Isolated modes  $(n, q, l)$  are therefore sensitive to even degrees of structure,  $s = 0, 2, \dots, 2l$ . Coupled modes may contribute sensitivity to odd degree structure, in addition to even degree structure. Coupled modes may have additional odd degree sensitivity if the difference and sum of their angular orders  $(l, l')$  is odd. For example, the modes  ${}_1S_5$  at 1.370 mHz and  ${}_2S_4$  at 1.379 mHz are coupled, and have sensitivity to even degrees 0,2,4,6,8, and 10 and to odd degrees 1,3,5,7, and 9 (*Resovsky and Ritzwoller, 1995*).

In order to understand the depths at which the modal data have resolving power, we compute the combined sensitivity kernels of the 30 isolated and 14 coupled modes for each model parameter, at each harmonic degree of our model. Sensitivity kernels represent the weight which a perturbation from spherical structure has, at a particular depth, on the splitting of spectra. The combined

sensitivity of the modes to variations in mantle structure is computed as follows:

$$\mathcal{S}_{M^s}(r) = \frac{1}{N} \left( \sum_i^N M_{kk'}^s{}_i(r) \right)^2. \quad (5.3)$$

where  $s$  is the index of harmonic degree,  $M_{kk'}^s$  is the sensitivity kernel  $P_{kk'}^s$ ,  $S_{kk'}^s$ , or  $R_{kk'}^s$  (equations(3.53)-(3.54)),  $i$  is the mode index up to  $N$  total modes. The combined sensitivity of all the modes used in this study is predominantly to  $V_s$  (Figure 5.1), but at certain depths, particularly in the shallow portions of the lower mantle and near the core-mantle boundary, the sensitivity to  $V_s$  is reduced, and the sensitivity to  $V_p$  dominates. Sensitivity to  $\rho$ , on the other hand, is consistently lower than to velocity, except at the very top of the mantle.

### 5.5.2 Model parameter expansion

A model parameter,  $\delta \ln \mathbf{m} = (\delta \ln V_s, \delta \ln V_p, \delta \ln \rho)$ , representing a perturbation in seismic velocity or density in three-dimensions, can be expressed as a function of radius  $r$ , colatitude  $\theta$ , and longitude  $\phi$ , and expanded in spherical harmonics as follows:

$$\frac{\delta \mathbf{m}}{\mathbf{m}}(r, \theta, \phi) = \sum_p^{pmax} \sum_s^{smax} \sum_{t=-s}^s {}_p m_s^t f_p(r) Y_s^t(\theta, \phi),$$

where  ${}_p m_s^t$  are coefficients of expansion for radial functions  $f_p(r)$ , and spherical harmonics  $Y_s^t(\theta, \phi)$ .

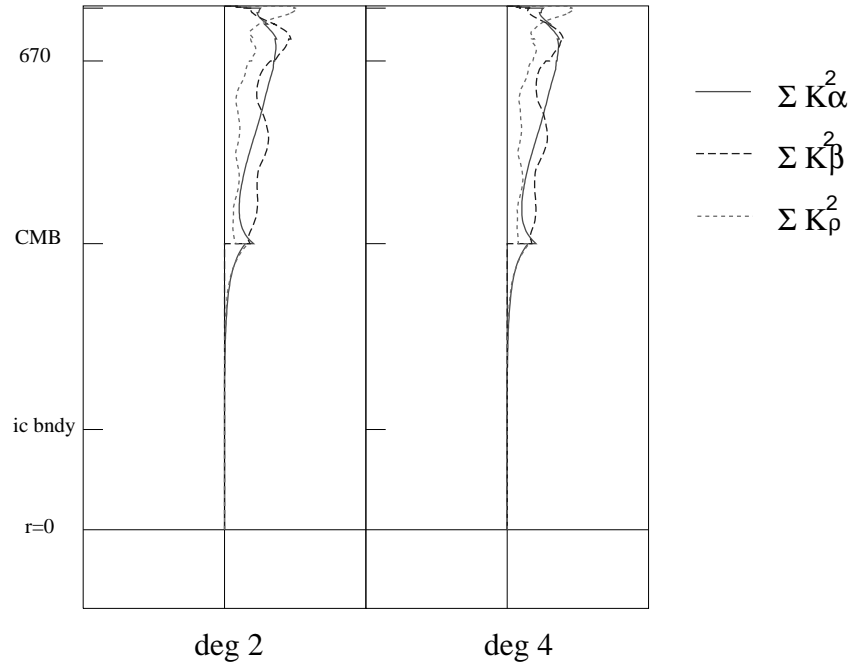


Figure 5.1: The accumulated sensitivity of mantle modes used in the inversion. The sensitivity kernels represent the weight which heterogeneity at a particular depth has on spectral splitting.  $\Sigma K_{\alpha}^2$  (solid line)  $\Sigma K_{\beta}^2$  (dashed line), and  $\Sigma K_{\rho}^2$  are the cumulative sensitivity of the modes to aspherical structure in compressibility velocity, shear velocity, and density as functions of depth, respectively, averaged over the number of modes in the data set. Shown in the left panel is the sensitivity to degree 2 structure, and the right panel, to degree 4 structure.

The choice of spherical harmonic expansion laterally simplifies the computation of coupling effects, owing to the mathematical rules that govern the  $\gamma_{ll's}^{mm't}$  coefficients. As the modes in our data set have very low frequencies, they are sensitive to very long wavelength structure. Given that the lowest angular order in our data set is  $l = 2$ , all the modes in the data set have sensitivity in even degree structure up to degree 4. While many of the modes have sensitivity to even degree structure higher than 4, we only have 4 coupled mode pairs which have sensitivity to odd degree structure: two pairs from which odd degree 1-9 structure ( ${}_2S_4 - {}_1S_5$  and  ${}_2S_5 - {}_1S_6$ ) can be retrieved, and two pairs from which degrees 5-11 ( ${}_4S_3 - {}_2S_8$  and  ${}_6S_3 - {}_3S_8$ ) can be retrieved. In the interest of ensuring that each harmonic degree of our models is well 'sampled', we first limit the harmonic degree of heterogeneity in our model to a maximum value of 4 in preliminary tests of data sensitivity to model parameters. After the mode sensitivity to model parameters has been established, we will show models extended to degree 6, in order to avoid the effects of aliasing. The polynomial order of the radial basis functions was chosen to be roughly equivalent to the maximum radial order of the modes used in the data set. As we reported in Section 5.3, our data set primarily consists of modes up to radial order  $n = 5$ , but we also include a few modes of higher radial order. Thus, we have chosen to use Legendre polynomials up to order 7 to describe the heterogeneity radially.

## Layered models

Using local basis functions to parameterize the model radially has the advantage over a global basis set in that strong heterogeneity located in particular depth regions, such as D'', should remain localized in the model, rather than possibly being smoothed out over the whole depth range by low order global parameterization. By discretizing the mantle depths into layers, we have observed that the final models are consistent with models radially parameterized by Legendre polynomials of order 7, for harmonic degrees 2 and 4, both in terms of root mean square amplitude profiles and heterogeneity patterns at various depths. For all layers, the pattern of heterogeneity retrieved in a particular model is an average of the polynomial model patterns of structure over the depth range of that layer. Furthermore, there is no significant degradation nor improvement in the misfit to the data when using a layered parameterization to describe the depth dependence of heterogeneity of  $V_s$ ,  $V_p$  and  $\rho$ . Other authors sometimes use splines, where the basis spline amplitudes in depth can be weighted according to the corresponding mode data set sensitivity (*Masters et al., 1996; Mégnin and Romanowicz, 1999*).

### 5.5.3 Model structure parameterization

The contamination of a  $V_s$  model by  $V_p$  and  $\rho$  structure, when both  $V_p$  and  $\rho$  are assumed to scale with  $V_s$ , can be illustrated by the trade-offs between models

derived from dependent and independent model parameters. The trade-offs between  $\delta \ln V_s$ ,  $\delta \ln V_p$  as well as  $\delta \ln \rho$  were tested by running three experiments: 1) one in which only  $\delta \ln V_s$  was retrieved, 2) one in which  $\delta \ln V_s$  and  $\delta \ln V_p$  were inverted independently, and finally, 3) one in which  $\delta \ln V_s$ ,  $\delta \ln V_p$ , and  $\delta \ln \rho$  were determined independently. We label the resulting models S.sclPR, PS.sclR, and PSR.noscl, respectively. For the first experiment (S.sclPR), the perturbations in  $V_p$  and  $\rho$  were assumed to vary with  $\delta \ln V_s$  uniformly throughout the mantle, according to:  $\frac{\delta \ln V_s}{\delta \ln V_p} = 2.0$  and  $\frac{\delta \ln V_s}{\delta \ln \rho} = 4.0$ . (*Li et al., 1991b*). In the second experiment (PS.sclR), the perturbations to  $\rho$  were set to scale to  $\delta \ln V_s$  with  $\frac{\delta \ln V_s}{\delta \ln \rho} = 4.0$ .

Model assessment includes correlating the S-velocity model from each experiment with SAW12D, and comparing the data misfits obtained in each experiment. We opt to use SAW12D as the standard for S-velocity perturbations in the mantle as it was developed using SH waveform data, and therefore is a purely shear model, whereas other models, which include SV data, have built-in assumptions about relation of P to S velocity in the mantle. However, we also show comparisons with a Harvard derived  $V_s$  model, SH12WM13 (*Su et al., 1994*). The residual variance is defined as follows:

$$\varsigma^2 = \frac{\sum_i (d_i - d_i^p)^2}{\sum_i d_i^2}$$

where  $d_i$  is the data at each station  $i$ , and  $d_i^p$  is the prediction from the model.

Since the number of model parameters varies between experiments, the number

of degrees of freedom needs to be taken into account when comparing fits to the data. We consider the following data misfit definition:

$$\sigma_d^2 = \frac{1}{N - M} \sum_i \frac{(d_i - d_i^p)^2}{\sigma_i^2}$$

where  $d_i$  and  $d_i^p$  are defined as above,  $\sigma_i^2$  is the estimate of uncertainty for each measurement of the  $N$  spectra at station  $i$ , and  $M$  is the number of model parameters. Uncertainty in the mode spectral measurement can be estimated by considering the noise floor of the seismic trace, the time window chosen before Fourier transforming which affects the signal power and resolution, and the frequency window bounds for each spectral measurement, which may incorporate signal from neighboring modes. In addition to the weighting scheme outlined in the data covariance matrix description, we assume that the measurement error is at least as good as what we can predict from theory. From spectral records of well-excited modes in which noise is so minimal as to appear absent, we find that this error is about 1% of the size of the record. The 1% error represents the difference between our ability to predict the spectrum from the theory and the observed spectrum.

There are approximations imposed on the theoretical formulation which we employ, and they further limit the accuracy of the tomographic technique. These approximations in the theory include utilizing a spherically stratified elastic reference Earth model (e.g.. PREM) and extending the representation of the spherical structure to perturbations of only first order. The eigenfunctions and refer-

ence eigenfrequencies are computed from the spherically stratified elastic Earth model. Accuracy in spectra prediction could be increased by applying higher order perturbation theory (*eg. Lognonné and Romanowicz, 1990*), computing reference eigenfunctions and eigenfrequencies from a 3-D model, and updating the reference eigenfunctions and eigenfrequencies with each iteration of inversion for 3-D structure until convergence is reached (*Clévéde and Lognonné, 1994*). This higher order method is computationally laborious, but would allow for wave propagation effects to be modeled such as focusing and defocusing effects due to 3-D structure, which we here neglect.

We also neglect departures from a simple Q-model as described by PREM. Choosing a time window for the seismic trace which does not exceed 1.1 Q-cycles (*Dahlen, 1982*) we assume, however, that spectral peak broadening is dominated by 3D elastic effects.

## 5.6 Results of model parameterization experiments

In the following experiments, three-dimensional structure was parameterized in terms of spherical harmonics up to degree 4 laterally, and in the radial direction, using Legendre polynomials up to degree 7. We have already mentioned that using a layered parameterization in depth gives consistent results. Damping parameters have not been fully explored in these preliminary experiments, but the norm damping was set so as to produce models whose root-mean-squared



amplitude values in  $V_s$  are of the same order as SAW12D (*Li & Romanowicz, 1996*).

### 5.6.1 $\delta \ln V_s$ models

In the first experiment, only  $V_s$  is solved for and the resulting model is labeled *S.sclPR*.

After 3 iterations, the residual variance, as defined above, is 0.308. The structure obtained in the depth range 800-1200 km and near the core-mantle boundary for S.sclPR differs significantly from existing  $\delta \ln V_s$  models based on body wave and surface wave data such as SAW12D and SH12WM13 (*Su et al., 1994*), as can be seen in the correlation profiles of lateral heterogeneity in Figure 5.2 a and b (solid lines). Although it is possible that the differences reflect differences in sampling between body-wave studies and normal modes in this depth range, we also note that the combined sensitivity amplitude of the mode set to  $V_s$  structure is relatively small in this depth range (Figure 5.1), whereas the sensitivity to  $V_p$  structure is strong. The lack of correlation of *S.sclPR* with *SAW12D* and *SH12WM13* in the depth range 800-1200 km may be due to  $V_p$  structure inadvertently being mapped into  $V_s$  structure by using inaccurate a priori assumptions about the relationship between  $V_s$  and  $V_p$  heterogeneity throughout the mantle. As we will see below, we favor the latter explanation.

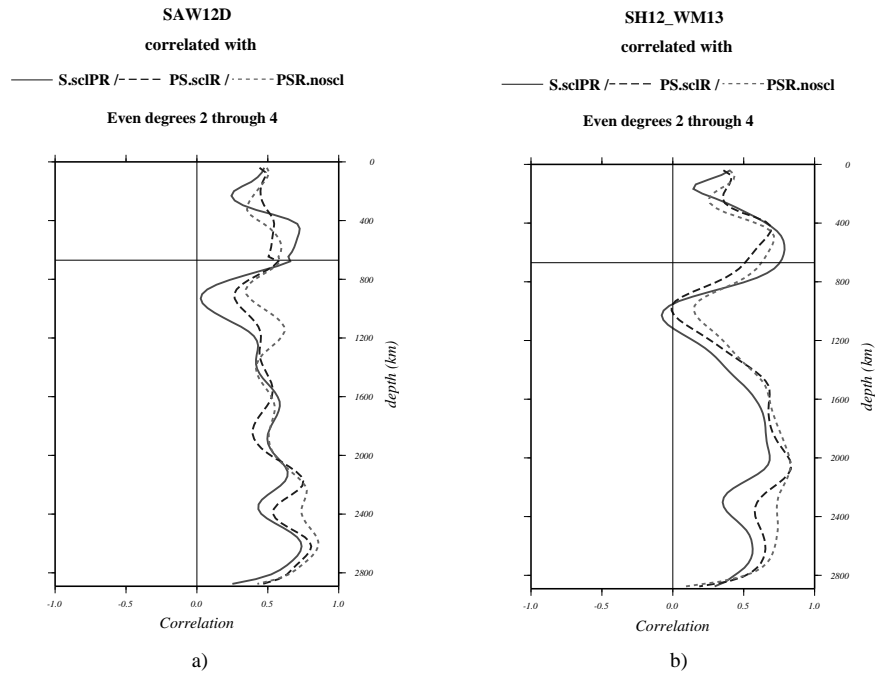


Figure 5.2: For degrees 2 and 4, correlation profiles in  $V_s$  models S.sclPR in solid line, PS.sclR in dashed line, and PSR.noscl in dotted line, to a) SAW12D and b) SH12WM13. The improvement of mode spectra inversion capability in imaging  $V_s$  perturbations when relaxing scaling relationships between  $V_s$ ,  $V_p$ , and  $\rho$  is demonstrated by the dotted line, for model PSR.noscl.

### 5.6.2 $\delta \ln V_s, \delta \ln V_p$ models

In the second experiment, we invert for  $\delta \ln V_s$ , and  $\delta \ln V_p$  jointly and independently (*PS.sclR*). We use the same damping of the model norms for both  $V_s$  and  $V_p$  models in order to remain consistent with the previous experiment.

By increasing the model space from a  $V_s$  model to a joint inversion of  $V_s$  and  $V_p$ , the variance after two iterations is reduced from 0.308 to 0.278. More significantly, the variance per degree of freedom is decreased from S.sclPR to PS.sclR; the ratio  $\sigma_{dS.sclPR}^2 / \sigma_{dPS.sclR}^2 = 1.292$  (equation 4.11). This implies that the spectra are better explained by inverting separately for P-velocity and S-velocity perturbations in the mantle. From the dashed line in Figures 5.2a and 5.2b, the correlation of the  $V_s$  perturbation from this joint inversion to that of SAW12D is also improved somewhat in the depth range 800-1200 km, and at the bottom of the lower mantle, but it is degraded in the transition zone. There appears to be some trade-offs in our ability to retrieve the  $V_s$  structure in the mid-mantle.

### 5.6.3 $\delta \ln V_s, \delta \ln V_p$ , and $\rho$ models

Inverting for all three parameters independently (*PSR.noscl*) reduces the variance further to 0.271. In this case, the correlation with SAW12D (Figure 5.2, dotted lines) is improved in the mid-mantle, particularly between 800-1200 km, and also in the bottom 800 km of the lower mantle. We note that the

improvement in correlation in the depth range 800-1200 km is less strong when the reference model is SH12\_WM13, a model derived from both SH and SV data.

By inverting separately for  $V_s$ ,  $V_p$ , and  $\rho$ , we not only decrease the residual variance, but also improve the correlation of the resulting  $V_s$  model with independently derived tomographic  $V_s$  models. While the improvement in variance is marginal and could, by itself, be attributed to the addition of 240 parameters, the improved correlation indicates that there are resolvable differences between modeling  $V_s$ ,  $V_p$ , and  $\rho$ .

#### 5.6.4 Fits to observed spectra

Figure 5.3 illustrates the fit to the spectrum and phase (solid lines) of spheroidal mode  ${}_5S_4$  from various model predictions (dashed lines): a) PREM, b) SAW12D, c) S.sclPR, d) PS.sclR, and e) PSR.noscl. S.sclPR gives a significantly better fit to  ${}_5S_4$  in both phase and spectrum amplitude compared to SAW12D, an SH model developed from an independent data set of body and surface waveforms. From f) in Figure 5.3, we see that  ${}_5S_4$  is predominantly sensitive to  $V_p$  perturbations. The model with relaxed scaling between  $V_p$  and  $V_s$  perturbations, PS.sclR, improves the fit to the spectrum even more, particularly the amplitude. We see that the addition of density perturbations in the model parameterization does not improve the fit for this mode. On the other hand, Figure 5.4 shows the fits obtained to a primarily S-sensitive mode,  ${}_1S_7$  for the

different models. As seen from the bottom right panel of this figure, this mode has some sensitivity to density in the upper-most mantle and the mid-lower mantle. Improvements in fit from SAW12D, *S.sclPR* and *PS.sclR* are marginal. When comparing the *PS.sclR* fit with that of *PSR.noscl*, we note a perceptible, although not large, improvement in the amplitude of the larger peak. More generally, fits to modes with some sensitivity to density are slightly improved when density is inverted for independently, although one could argue that other unmodeled factors could equally well influence the amplitudes of these modes, at the marginal level of improvement that we observe.

Table 5.2 summarizes the fit of the three models, *S.sclPR*, *PS.sclR*, and *PSR.noscl*, to the observed spectra. The residual variances decrease with increasing number of model parameters, as expected. However, the significance of the parameterization is assessed by the error per degree of freedom,  $\sigma_d^2$  (equation (4.11)), for each model. A model parameterization  $M_1$  significantly improves the fit to the data over  $M_2$  if  $\sigma_{d1}^2/\sigma_{d2}^2 > 1$  (*Menke, 1989*). We note from the ratios of  $\sigma_d^2$  that although *PSR.noscl* does not improve the error per degree of freedom compared to *PS.sclPR*, the change in error is slight. From Figure 5.1, it is apparent that most of the sensitivity of our mode data set is to  $V_s$  and  $V_p$ , and there is little to density. Through these kernels, the contribution of the density model to the spectra is small, and we do not expect the density model to be well resolved. Nevertheless, as we will see below, our observations of den-

PAS

Power spectra fits to  ${}_5S_4$   
June 9, 1994 Mw=8.3 event

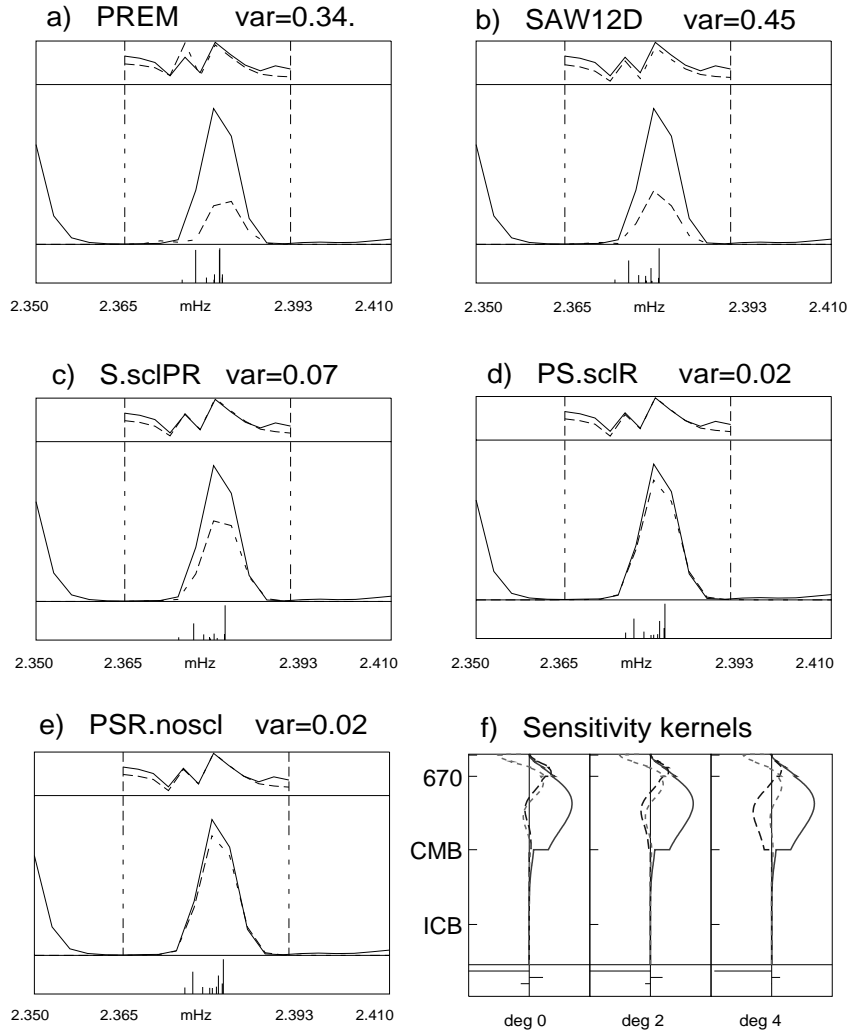


Figure 5.3: The fit to the spectrum and phase (solid lines) of spheroidal mode  ${}_5S_4$  from various model predictions (dashed lines): A) PREM, B) SAW12D, C) S.sclPR, D) PS.sclR, and E) PSR.noscl. The top panel of each plot in A)-E) shows the fit to the phase, the middle panel shows the fit to the spectrum, and the bottom panel illustrates the predicted singlet contribution to splitting. The abscissa range dimension is frequency in mHz.  ${}_5S_4$  is a predominantly  $V_p$  sensitive mode, as seen in F), where the solid line indicates sensitivity to  $V_p$ , dashed to  $V_s$ , and dotted to  $\rho$ , with depth for degrees 0, 2 and 4 structure. The spectra are plotted for the June 9, 1994 Bolivia event at station PAS, in Pasadena, California.

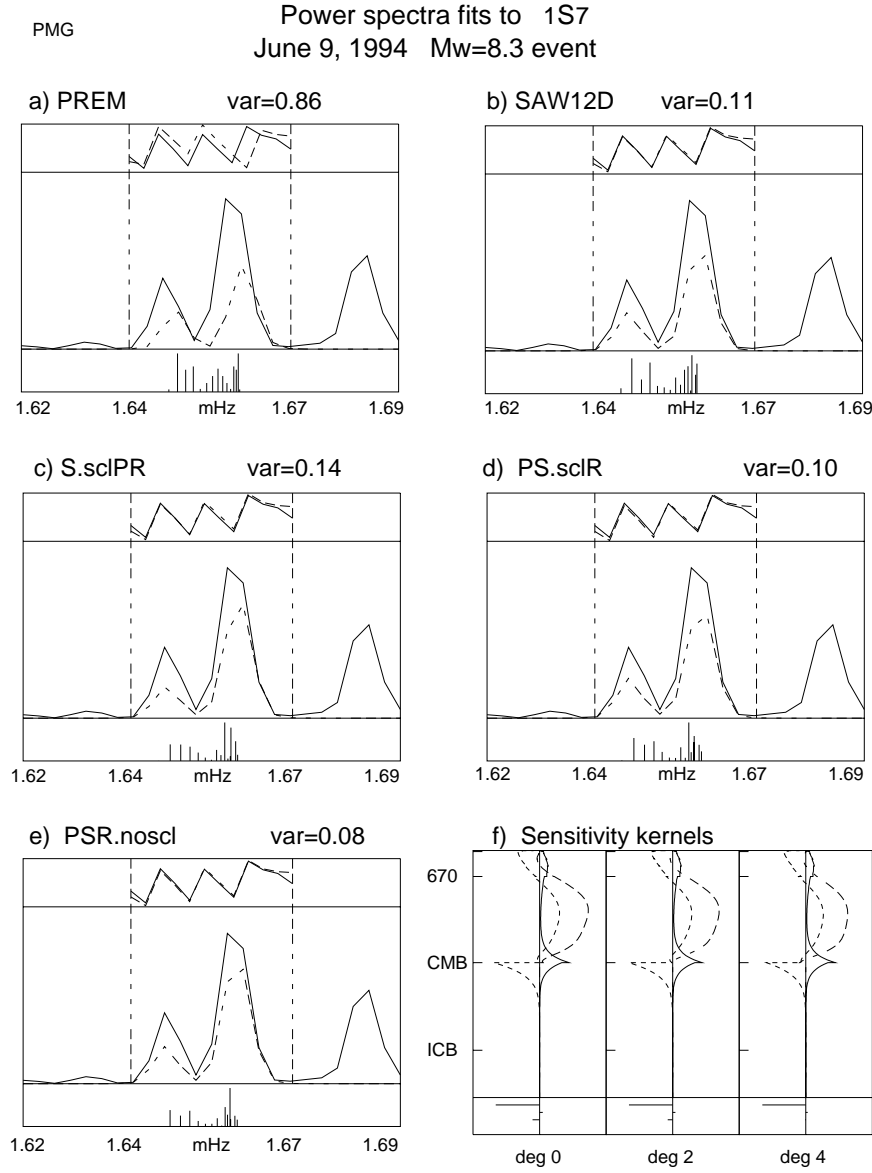


Figure 5.4: The same as in Figure 5.3, but for mode  ${}_1S_7$ , which has little sensitivity to  $V_p$ , but is rather  $V_s$  and  $\rho$  sensitive. These spectra are plotted for the same event as in Figure 5.3, but at station PMB, in Port Moresby, New Guinea.

Table 5.2: The fits to the data for the models listed in column 1, described in the text, are summarized here. The lateral parameterization of the models is listed in the third column, and the radial parameterization is to polynomial order 7 for each model parameter  $\delta \ln V_p, \delta \ln V_s$ , and  $\delta \ln \rho$ . M is the number of model parameters, and N is the number of data spectra. The fifth column lists the ratio of the model variance per degree of freedom ( $\sigma_d^2$  equation 4.11) to that of the previous model to assess the significance of data fit after removing scaling relationships between the model parameters (see Section 4.3. There is significant improvement by independently solving for S-velocity and P-velocity perturbations, but by additionally relaxing the scaling between S-velocity and density perturbations, there is marginal significance in improvement. (See text for details).

Model	Model Parameters	$s_{max}$	M	N	Data Misfit	$\frac{\sigma_{d\ prev}^2}{\sigma_d^2}$
S.sclPR	$\delta \ln V_s$	4	120	2630	0.308	—
PS.sclR	$\delta \ln V_p, \delta \ln V_s$	4	240	2630	0.278	1.292
PSR.noscl	$\delta \ln V_p, \delta \ln V_s, \delta \ln \rho$	4	360	2630	0.271	0.964
PR.fixS— .SAW12D	$\delta \ln V_p, \delta \ln \rho$	4	240	2630	0.265	—
S.sclPR.s6	$\delta \ln V_s$	6	392	2757	0.258	—
PS.sclR.s6	$\delta \ln V_p, \delta \ln V_s$	6	784	2757	0.225	1.180
PSR.noscl.s6	$\delta \ln V_p, \delta \ln V_s, \delta \ln \rho$	6	1176	2757	0.230	0.830

Table 5.3: A comparison of the fit to the data when modelling for  $V_p$  and  $V_s$  perturbations. In model PS.sclR.s6, perturbations in  $\rho$  are assumed to scale with  $V_s$  perturbations. In model PS.noR, perturbations in  $\rho$  are assumed to be zero. Both models fit the data about equally well, although there is a slight improvement when taking  $\rho$  perturbations into account.

Model	Model Parameters	$s_{max}$	M	N	Data Misfit	$\frac{\sigma_{d\ prev}^2}{\sigma_d^2}$
PS.sclR.s6	$\delta \ln V_p, \delta \ln V_s$	6	784	2757	0.225	—
PS.noR	$\delta \ln V_p, \delta \ln V_s$	6	784	2757	0.227	0.9617148



sity heterogeneity in the mantle are consistent with geodynamical expectations. The confidence in the density model retrieved is thus solely based on indirect evidence. On the other hand, the importance of solving independently for  $V_p$  heterogeneity is much clearer. In what follows, we present further tests of the stability of the  $V_p$  and  $\rho$  models.

### 5.6.5 Separate inversions of $V_p$ and $V_s$ sensitive modes

In the following experiments, we performed two separate inversions independently for  $V_s$  and  $V_p$ , keeping  $\delta \ln \rho$  scaled to  $\delta \ln V_s$ , using different subsets of data:

1. *PS.sclR.Smod*, including only  $V_s$  sensitive modes in the data set, and
2. *PS.sclR.Pmod*, including only  $V_p$  sensitive modes in the data set.

The spatial and damping parameters of the models were kept the same as in the previous experiments.

In the first inversion, 18 primarily  $V_s$  sensitive modes (Figure 5.5) were used, and the final variance of the model (*PS.sclR.Smod*) is 0.255 after 2 iterations. The correlation in  $V_s$  with SAW12D is comparable to that obtained with PSR.noscl (Figure 5.6 and dashed line in Figure 5.2a). The  $V_s$  perturbations in this model and PSR.noscl are highly correlated at all depths whereas the  $V_p$  structure is not well correlated (Figure 5.7) in the depth range 1500-2500km,

directly reflecting the lack of sensitivity in this depth range to  $V_p$  in the reduced data set of  $V_s$  sensitive modes.

In the second inversion (*PS.sclR.Pmod*), 11 mostly  $V_p$  sensitive modes (Figure 5.8) were used. The final variance of the model is 0.215 after 2 iterations. The correlation of the  $V_p$  structure from this model with *PSR.noscl* is high except at the very top and bottom of the mantle (Figure 5.9), due to the decrease of  $V_p$  mode sensitivity in these regions. However, the subset of S sensitive modes considered above compensates for this in both regions, in the combined data set, as can be seen from Figure 5.5 and Figure 5.7.

These experiments demonstrate further that inverting separately for  $V_s$  and  $V_p$  is justified.

### 5.6.6 S-velocity "Correction" for P-velocity and density variation

Finally, returning to our whole data set, we test the stability of our  $V_p$  and density models by assuming that the  $V_s$  perturbations are those of SAW12D and solving for  $V_p$  and density structure independently (*PR.fixS.SAW12D*). We find that the resulting density model (which gives a residual variance of 0.265) correlates well throughout the mantle with the density model of *PSR.noscl*, except perhaps at the very top and bottom. This indicates that the density model obtained is stable. The  $V_p$  models, on the other hand, are not as stable in this

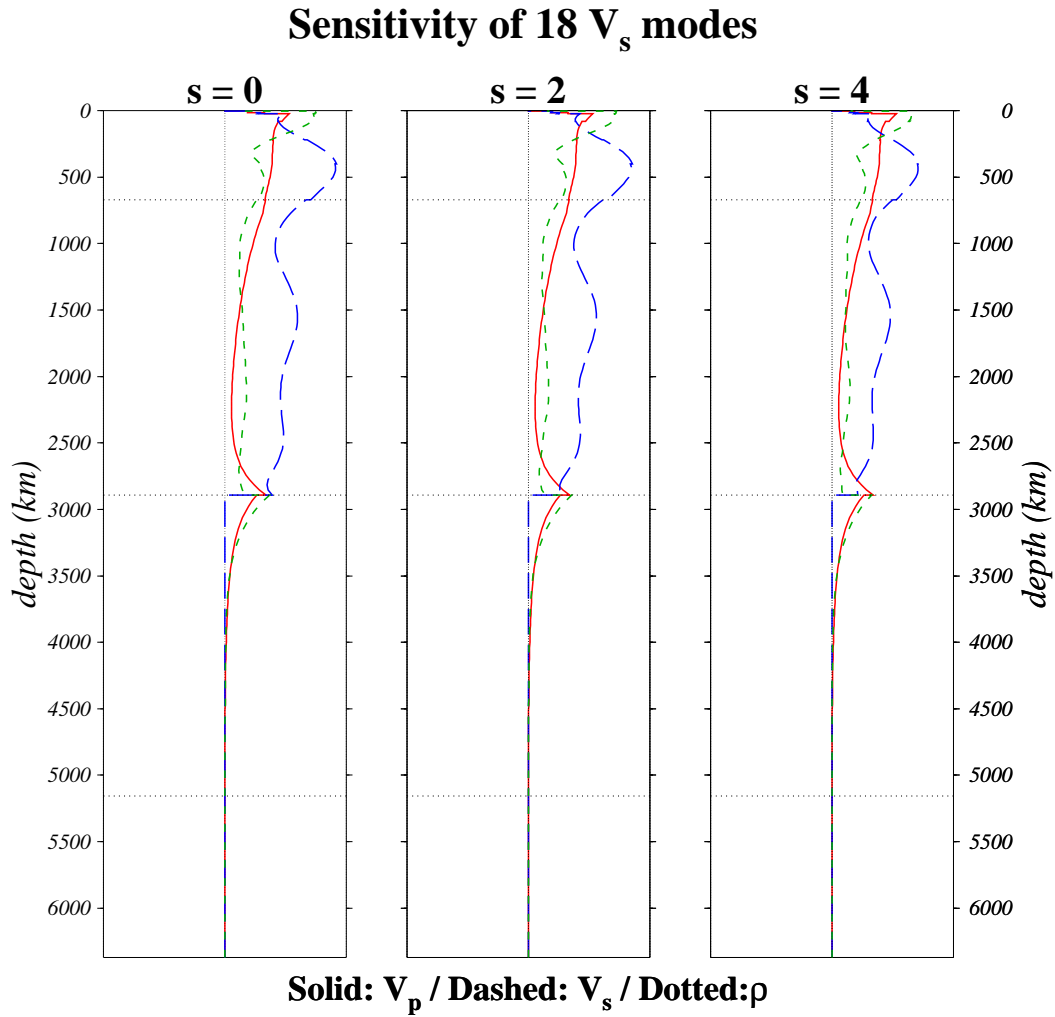


Figure 5.5: Cumulative sensitivity of 18 modes primarily sensitive to perturbations in  $V_s$ , as functions of depth plotted for  $V_p$  in solid line,  $V_s$  in dashed line, and  $\rho$  in dotted line. The left panel is the sensitivity to degree 0, middle panel to degree 2, and right panel to degree 4 aspherical structure. See caption in Figure 5.1 and text for detailed descriptions of cumulative sensitivity kernels.

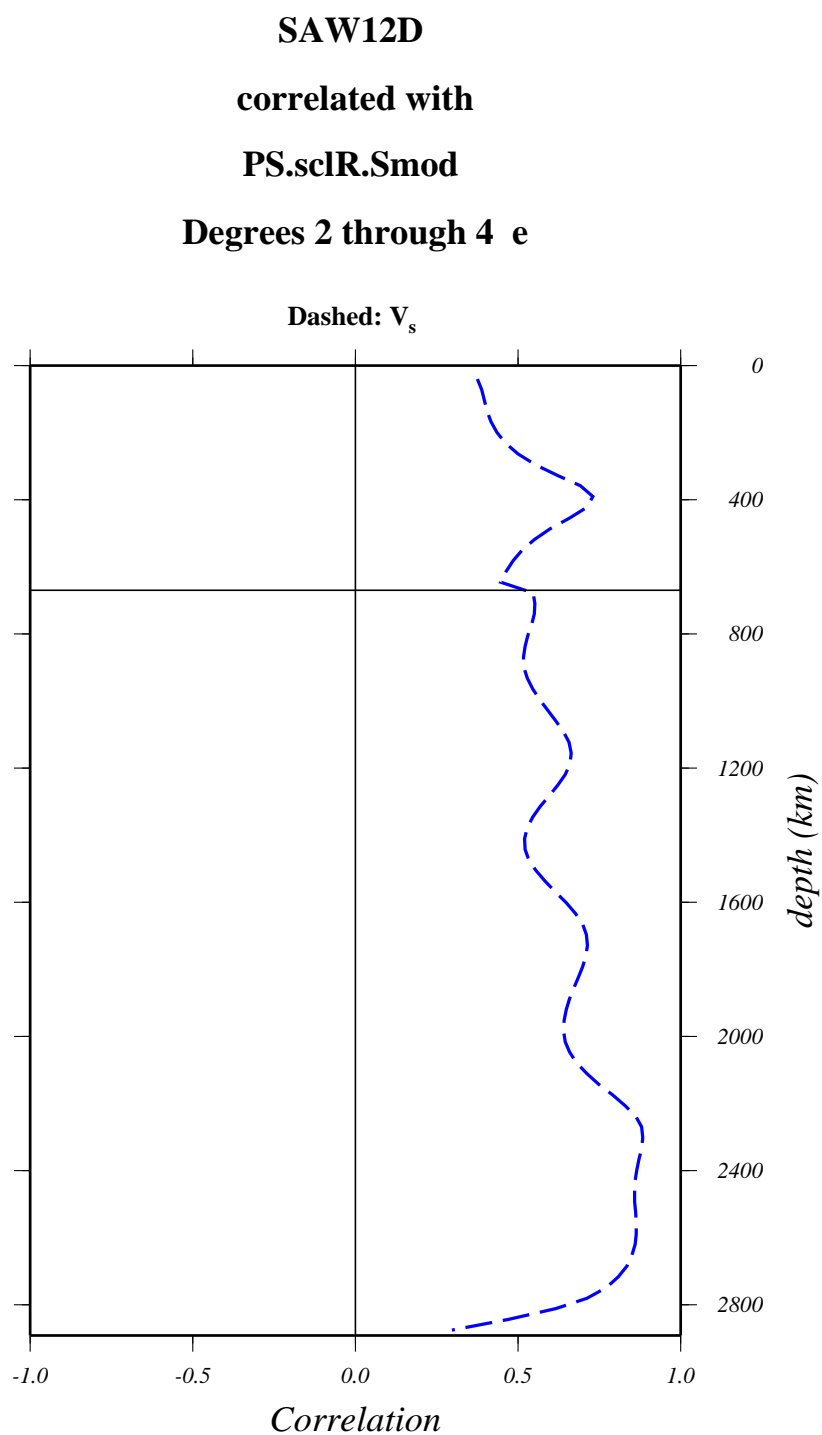


Figure 5.6: The  $\delta \ln V_s$  model PS.sclR.Smod, is correlated to SAW12D as a function of depth for degrees 2 and 4. There is good agreement with SAW12D.

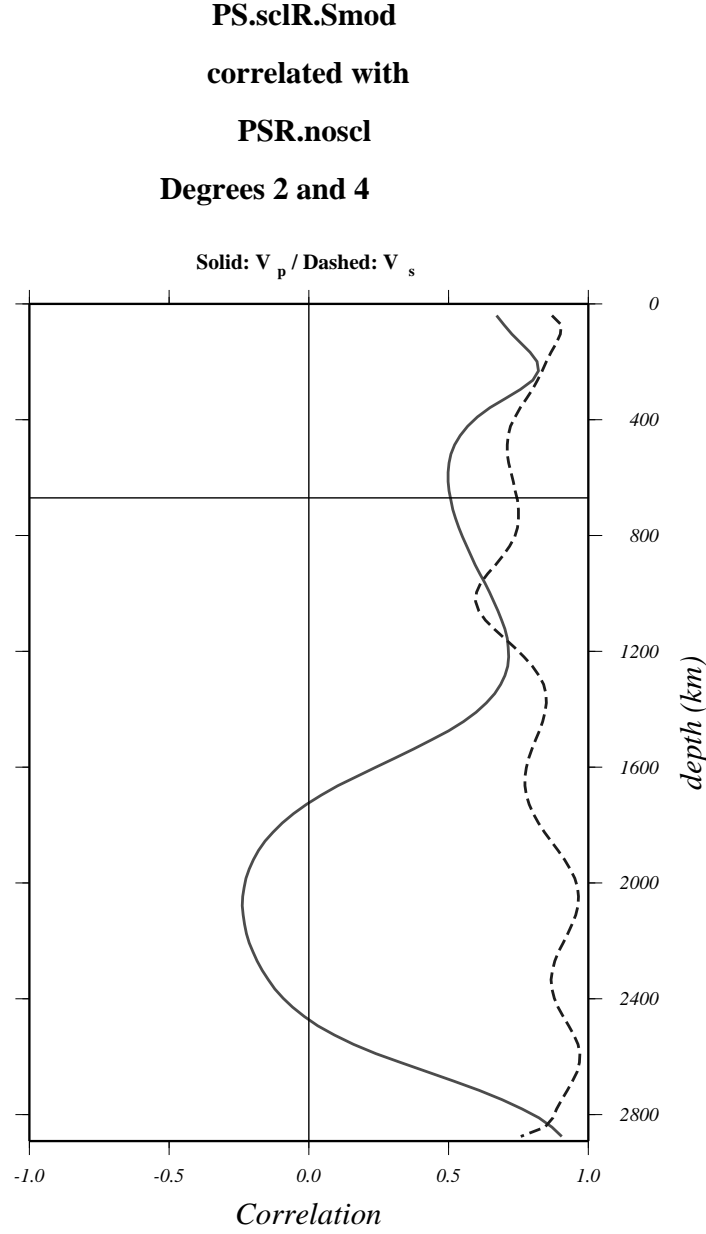


Figure 5.7:  $\delta \ln V_p$  of PS.sclR.Smod correlated with  $\delta \ln V_p$  of PSR.noscl, a model with includes all the modes in the data set, in the solid line. Since the sensitivity to  $\delta \ln V_p$  is weak for the data included for PS.sclR.Smod, the correlation is weak in the lower mantle. The correlation of  $\delta \ln V_s$  between the two models (dashed line) remains high. Correlation is for degrees 2 and 4.

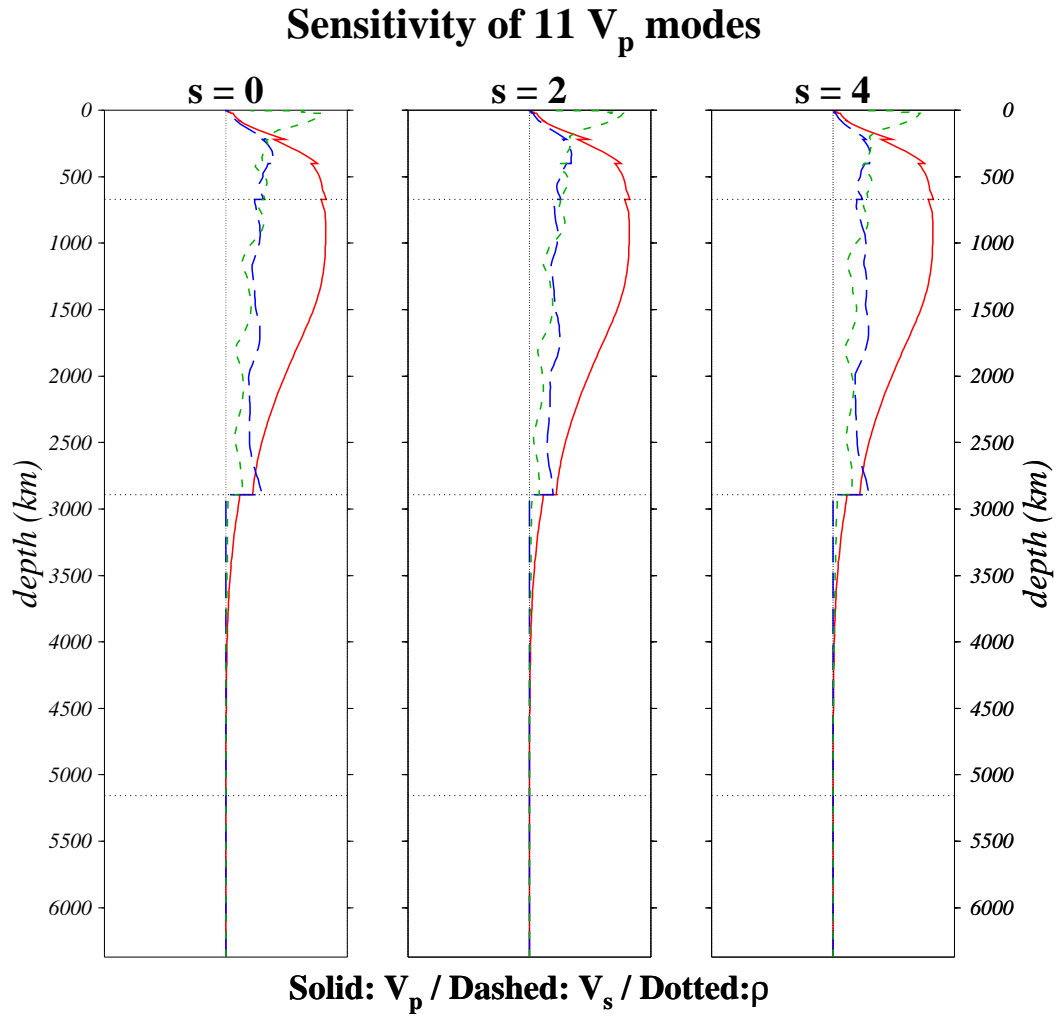


Figure 5.8: As in Figure 5.5, but for 11 modes primarily sensitive to perturbations in  $V_p$ , as functions of depth.

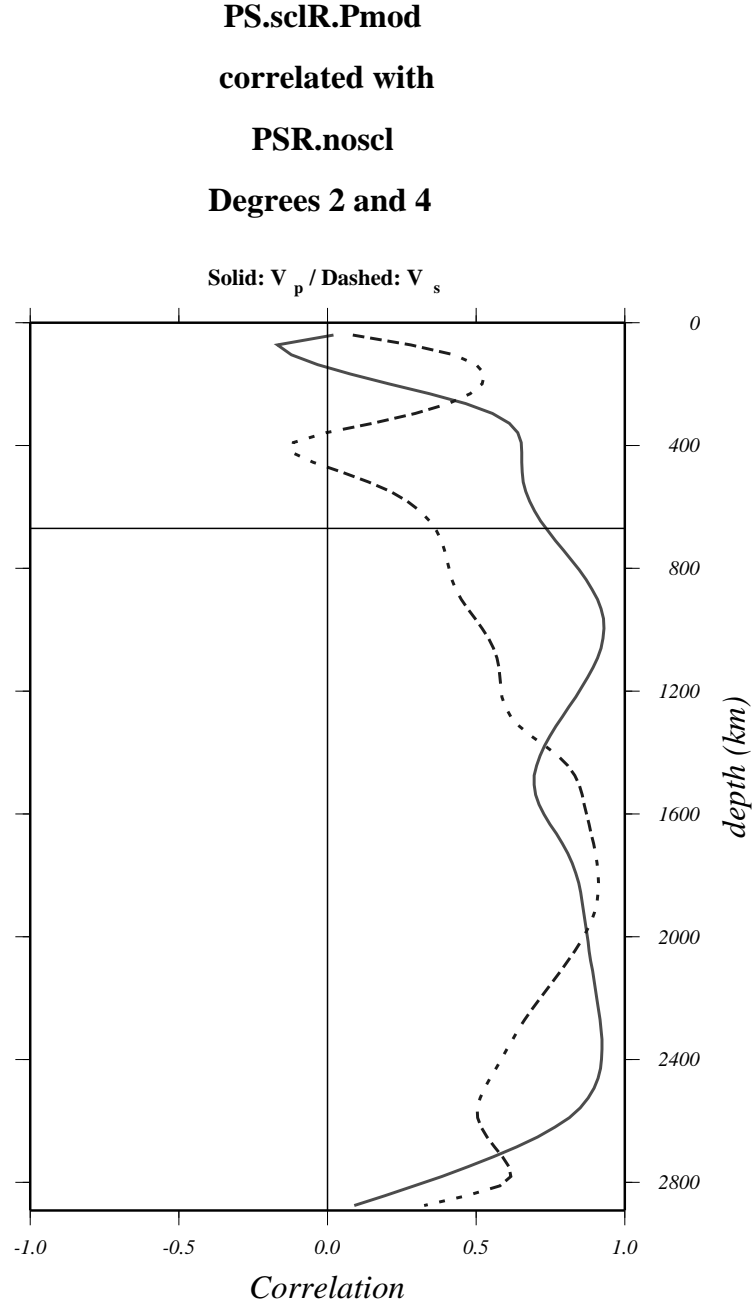


Figure 5.9:  $\delta \ln V_p$  of PS.sclR.Pmod correlated with  $\delta \ln V_p$  of PSR.noscl, a model with includes all the modes in the data set, in the solid line. The correlation of  $\delta \ln V_p$  between the two models is high. Since the sensitivity to  $\delta \ln V_s$  is weak for the data included for PS.sclR.Pmod, the correlation of  $\delta \ln V_s$  (dashed line) is not as strong between the two models.

comparison. The correlation is particularly poor in the mid-lower mantle, but the models agree in the lowermost mantle (Figure 5.10). This is an indication that the mode data set may provide additional constraints to low degree structure in  $V_s$  in the mid-mantle. Indeed, by requiring that the  $V_s$  perturbations follow those of SAW12D, we make the assumption that the mode data set has the same sensitivity and sampling as the higher frequency body and surface wave data. From the present experiment *PR.fixS.SAW12D*, it appears that the  $V_p$  structure retrieved for the lower mantle may be biased by assuming the  $V_s$  perturbations values of SAW12D at those depths. The final  $V_p$  solution from the three parameter inversion (PSR.noscl) correlates well with the  $V_p$  model inverted with primarily  $V_p$  sensitive modes (*PS.sclR.Pmod*) (Figure 5.9), indicating that the modes do find a stable solution for  $\delta \ln V_p$ , when no a-priori constraint is imposed on the  $V_s$  model.

In addition, we have computed the resolution matrix for the case in which  $V_s$ ,  $V_p$ , and  $\rho$  are independently retrieved which show that there are some trade-off between  $V_s$  and  $V_p$  perturbations, as well as with  $\rho$ . In Chapter 6, the effects of *a priori* constraints on model resolution, and contamination between parameters will be discussed.



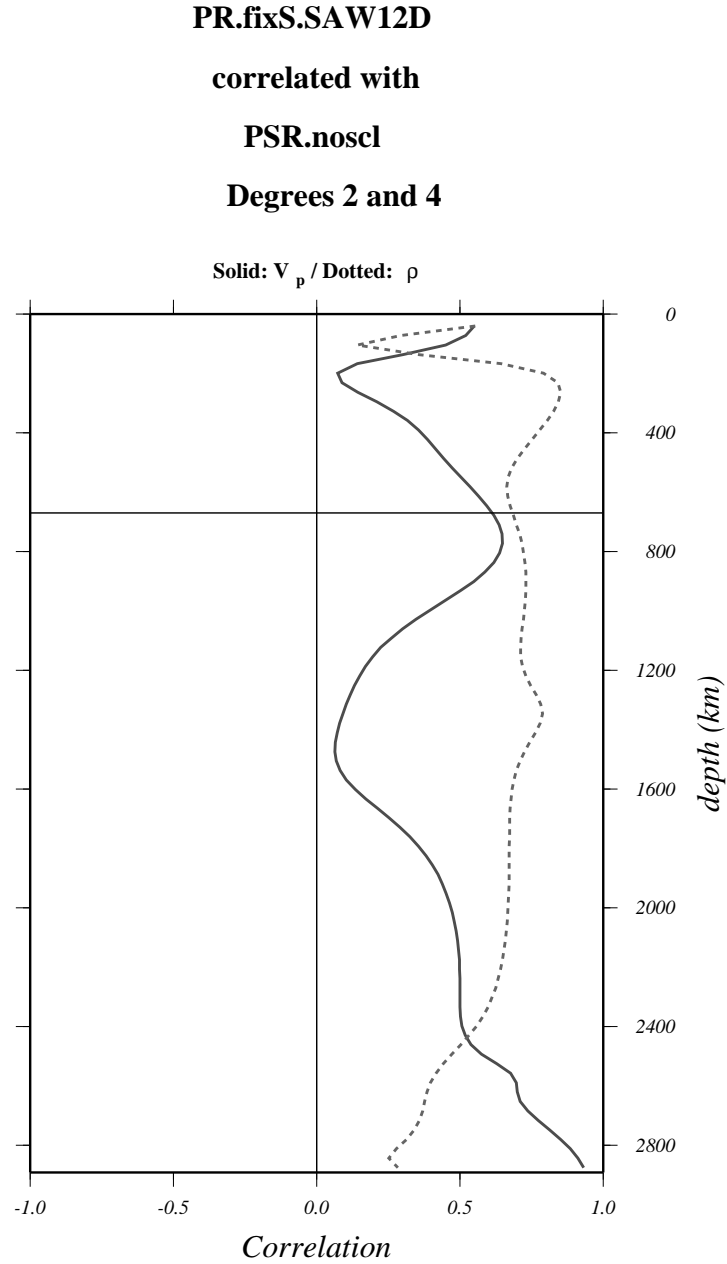


Figure 5.10: Correlation of  $V_p$  heterogeneity between model PR.fixS.SAW12D and PSR.noscl in the solid line, and the correlation of  $\rho$  heterogeneity from these two models, in the dotted line. There are some trade-offs between our ability to resolve  $V_p$  and  $V_s$ , but there is little contamination of velocity structure into  $\rho$  structure. The correlations are for degrees 2 and 4.

## 5.7 Model Results

Having determined in the previous section that there is some value in inverting independently for  $V_s$ ,  $V_p$  and  $\rho$ , we now present the resulting final models, *PSR.s4.cmb* and *PSR.s6.cmb*. In these models, we have allowed for perturbations in core mantle boundary topography, and we will discuss below the significance of doing so. This model was obtained after exploring damping parameter space. We damp the size, the second radial derivative, and the surface gradient (equation (4.8)). The values of damping parameters are chosen by exploring a range for each damping parameter, applying the damping to the inversion, and plotting trade-off curves of the misfit of the resulting models against damping parameter used in its inversion. The damping parameter value which gives the smallest misfit is chosen.

### 5.7.1 Velocity models in *PSR.s4.cmb*

In Figure 5.11, we display our degree 4  $V_p$  and  $V_s$  models at 6 representative depths in the mantle in the left and middle columns, respectively. Density heterogeneity is given in the right column. We only retrieve the very large scale features of lateral heterogeneity in degree 4, and upon inspection, we observe anomalous equatorial high shear velocity band in the shallow mantle. At the bottom of the mantle, shear velocity in *PSR.s4.cmb* also exhibits prominent high velocity regions in the Pacific which we attribute to higher order features derived

from body waves, *eg.*, SAW12D (*Li and Romanowicz, 1996*) or SKS12WM13 (*Dziewonski et al., 1997*). There is, otherwise, good correspondence with expected features of the dynamic Earth, as documented in other studies. Fast anomalies are associated with regions of subduction, particularly in the Western Pacific and are prominent under South America at 650 km depth. In the lower mantle to 1200 km, the fast velocities are somewhat shifted for  $V_s$ , while the  $V_p$  pattern remains stable. At the bottom of the mantle, compressional wave velocity maps exhibit high velocity rings around a low velocity Pacific Ocean.

The anomalous high  $V_s$  features in the degree 4 model may be attributed to aliasing, which is the effect of shorter wavelength terms becoming folded into longer wavelength terms due to the truncation of the polynomial series of our spatial model parameterization. In the next section, models parameterized to degree 6 in spherical harmonics are described.

### 5.7.2 Velocity models in PSR.s6.cmb

By extending the lateral parameterization to spherical harmonic degree 6, we obtain models with better resolution in which aliasing is diminished and shorter wavelength structure is resolved, as illustrated in Figure 5.12, where the models of heterogeneity in  $V_p$ ,  $V_s$ , and  $\rho$  are displayed in the same columns as in Figure 5.11. For six depths in the mantle at 200, 650, 1200, 1800, 2200, and 2800 km, we compare our  $V_s$  and  $V_p$  models (with and without CMB undulations) with

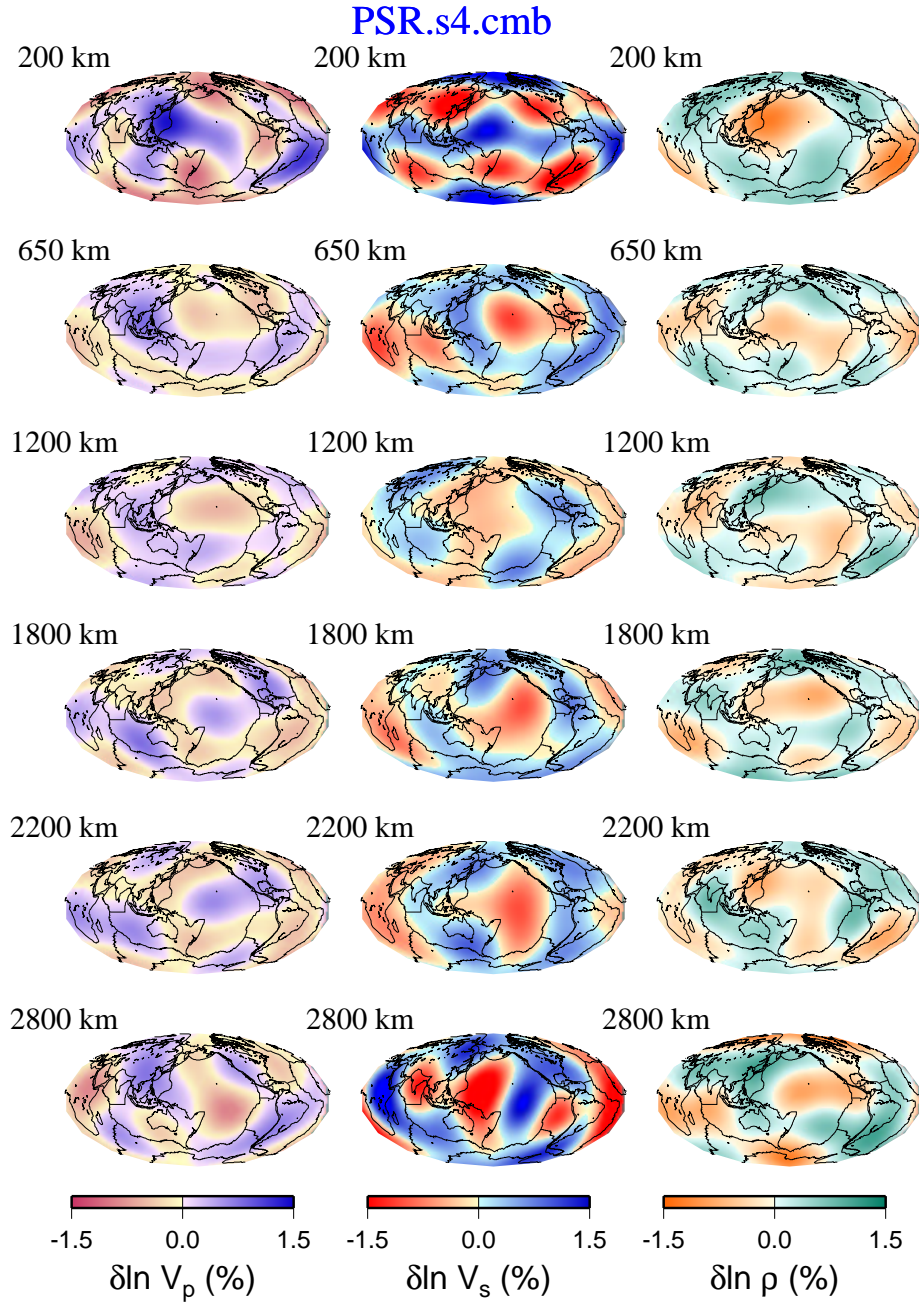


Figure 5.11: PSR.s4.cmb, degrees 1-4, for a)  $V_p$  perturbations, and b)  $V_s$  perturbations c)  $\rho$  perturbations.

independently derived published models, expanded in spherical harmonics up to degree 6 (Figures 5.13 and 5.14). The left map at each depth section is the  $V_s$  (respectively  $V_p$ ) structure of our model *PSR.s6.cmb*. The maps of independently derived heterogeneity are in the middle and right column in each depth section. In the  $V_s$  comparison (Figure 5.13), we use SAW12D (*Li and Romanowicz, 1996*) and SKS12WM13 (*Dziewonski et al., 1997*). For  $V_p$  (Figure 5.14), we compare our models with WE1997 (*Vasco and Johnson, 1997*) and P16B30 (*Masters and Laske, personal communication*). The model of  $V_p$  heterogeneity from WE1997 is inverted from ISC travel time data, and P16B30 incorporates travel time data, surface-wave phase velocities, and normal mode data in the form of 'splitting coefficients' for 19 spheroidal modes which have sensitivity to lower mantle structure.

There is very good agreement between our  $V_s$  model and both SAW12D (*Li and Romanowicz, 1996*) and SKS12WM13 (*Dziewonski et al., 1997*). The pattern of  $V_s$  heterogeneity at 200 km exhibits fast velocities beneath the colder Pacific Basin, beneath Western Australia, and beneath the American, African and Antarctic continents. Mid-ocean ridge regions associated with warm upwelling material are slow. At 650 km, fast velocities are prominent in regions often referred to as subducting slabs. In the lower mantle, the patterns in our  $V_s$  model appear to agree with those of SKS12WM13 more than with SAW12D. SKS12WM13 is sensitive to SV perturbations, and SAW12D is a model of SH

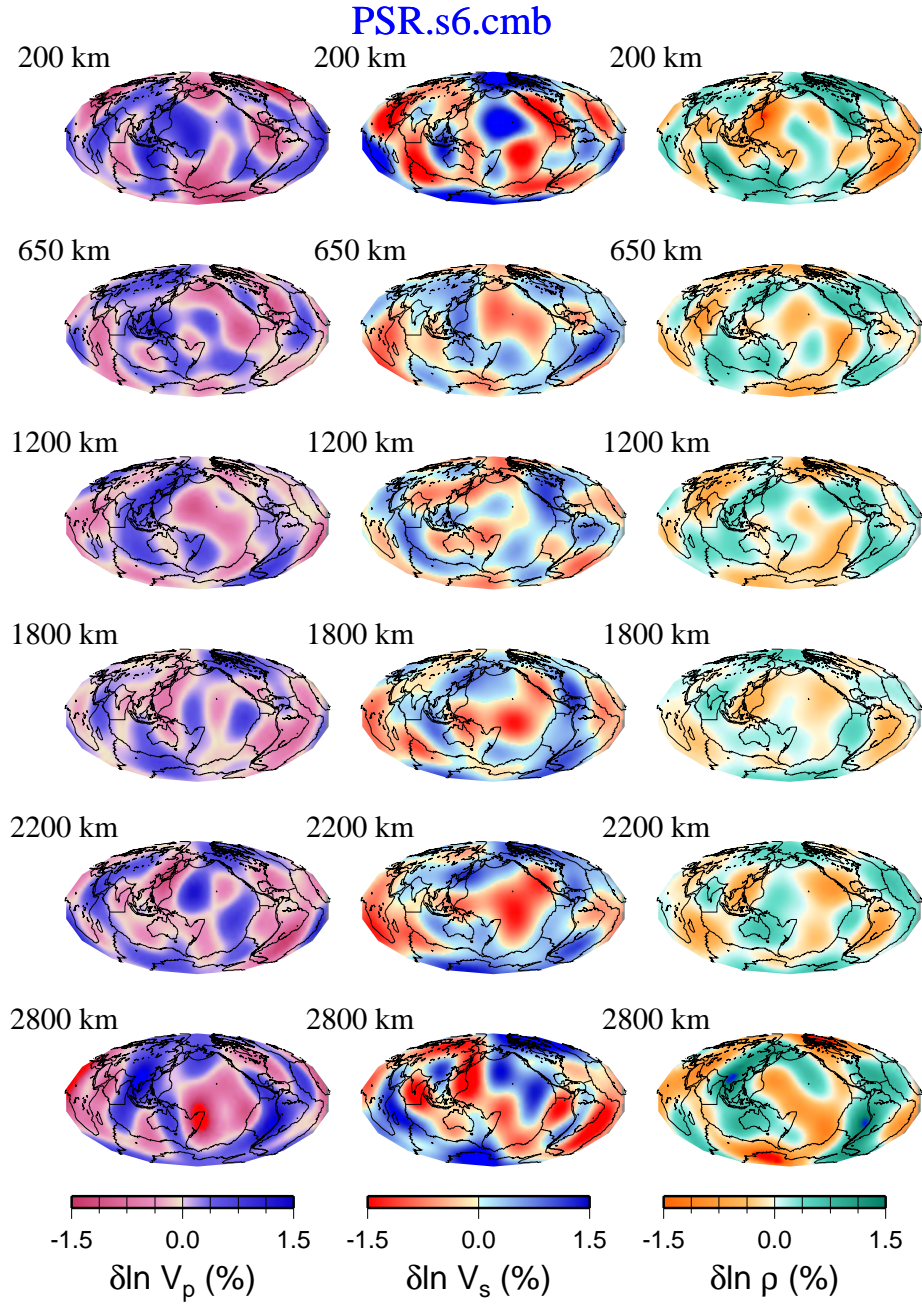


Figure 5.12: PSR.s6.cmb, degrees 1-6, for a)  $V_p$  perturbations, and b)  $V_s$  perturbations c)  $\rho$  perturbations.

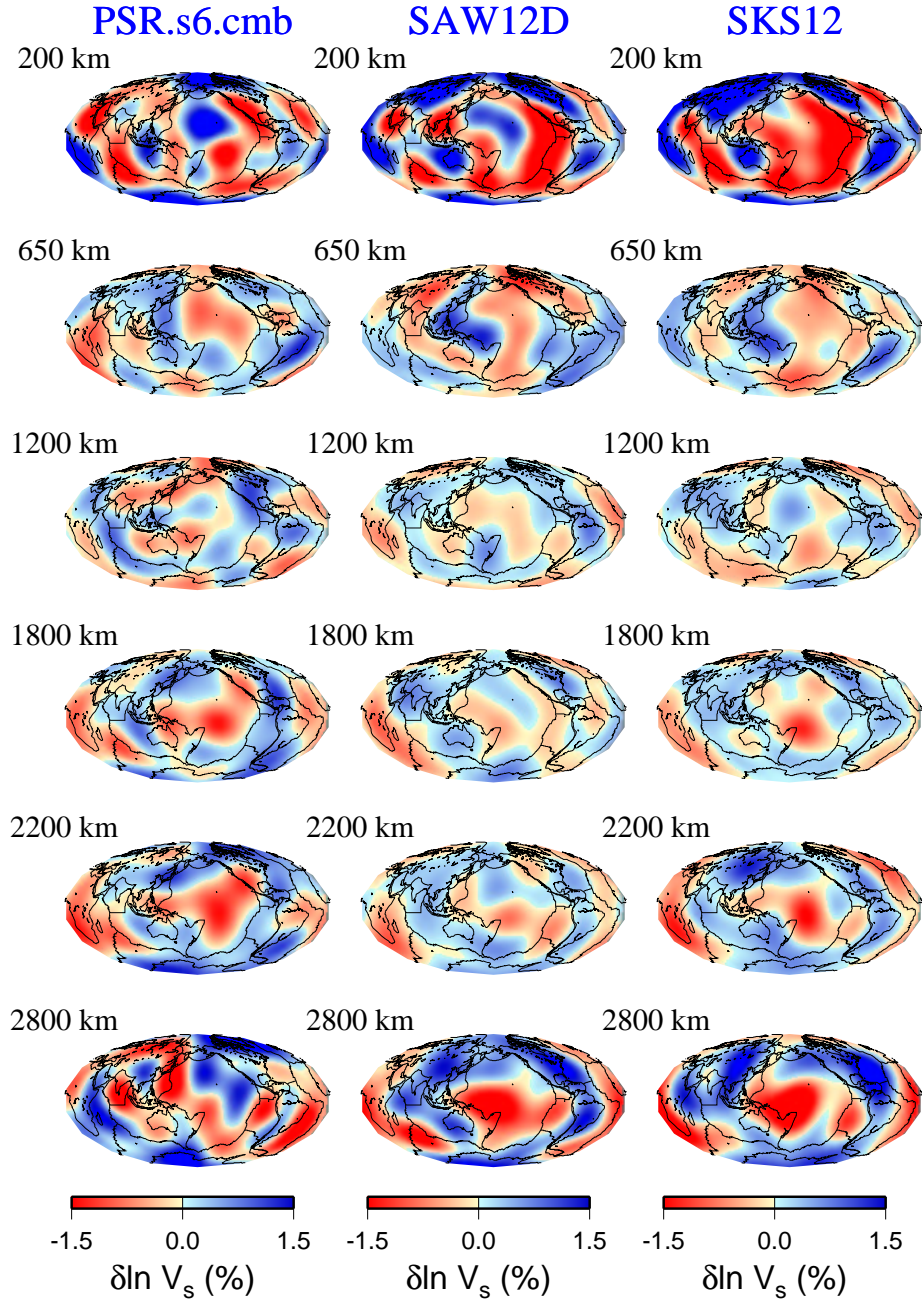


Figure 5.13: Comparison of 3 models of  $V_s$  perturbations for degrees 1-6. The left column is PSR.s6.cmb of this study, the middle column is SAW12D (*Li and Romanowicz, 1996*), and the right column is SKS12WM13 (*Dziewonski et al., 1997*).



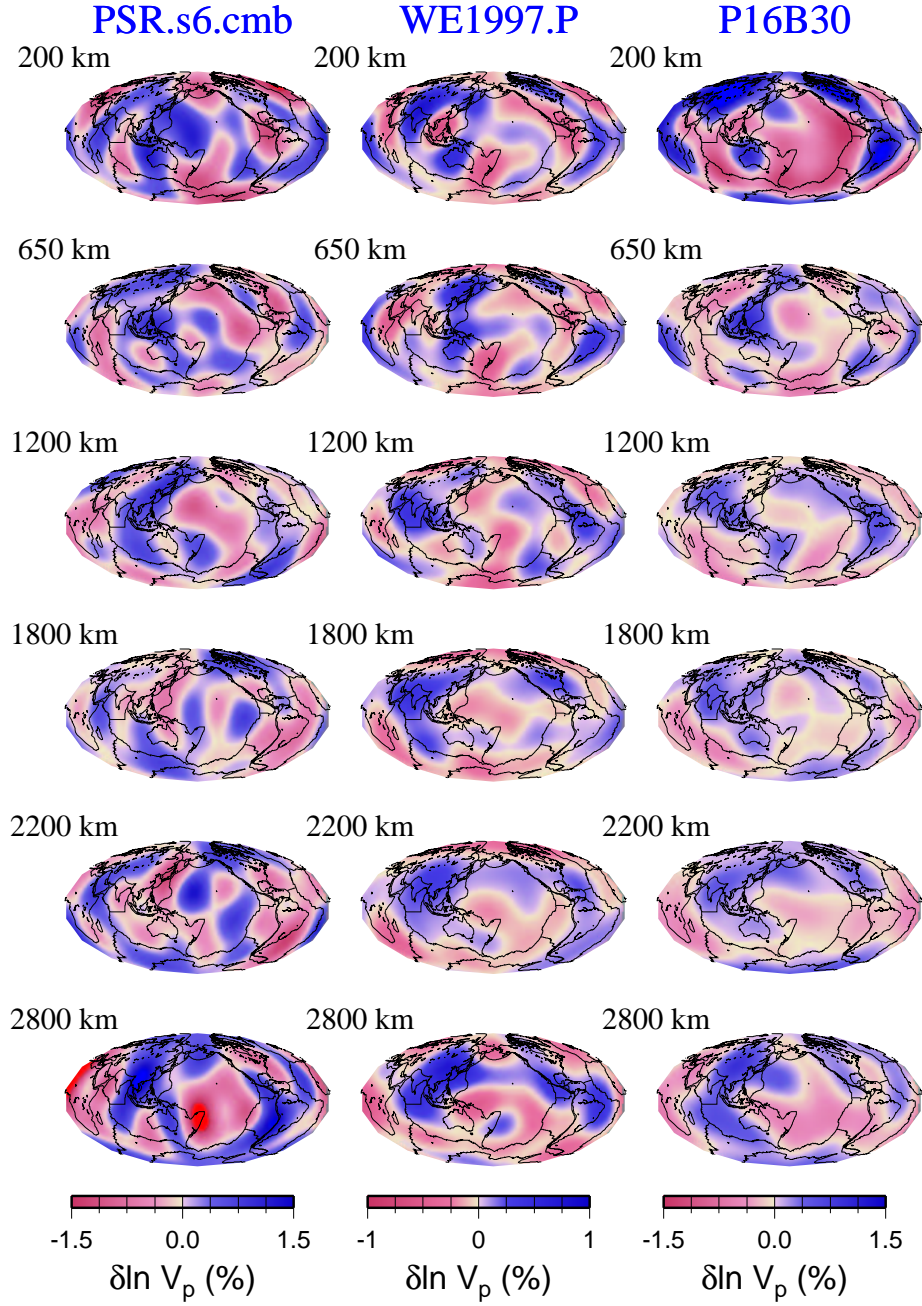


Figure 5.14: Comparison of 3 models of  $V_p$  perturbations for degrees 1-6. The left column is PSR.s6.cmb of this study, the middle column is WE1997 (*Vasco and Johnson, 1997*), and the right column is P16B30 (*Masters et al., 1996*).



perturbations. The correspondence of our model with SKS12WM13 is most likely due to the P-SV nature of particle motion for spheroidal modes. At the bottom of the mantle, however, our  $V_s$  differs from both SAW12D and SKS12WM13, in that our model lacks strong fast regions over Asia.

Referring to Figure 5.14, our model of  $V_p$  structure in the left column compares well with WE1997 (*Vasco and Johnson, 1997*) in the upper mantle. The upper mantle structure in P16B30 is constrained by a number of fundamental mode data, many of which we do not include in our data set. There is good agreement in the lower mantle at 1200 km, but at 1800 and 2200 km, our  $V_p$  model differs from WE1997 and P16B30. The origin of the patterns at these depths can be attributed to contamination from  $V_s$ , as we will discuss in Chapter 6.

### 5.7.3 Volumetric heterogeneity and boundary undulations

When the core-mantle boundary topography is not modeled, CMB undulations may be mapped into patterns of structure in the lowermost mantle. We compare a model *PSR.s6* which assumes a smooth CMB, with *PSR.s6.cmb* which includes CMB topography to try to understand the trade-off between solutions for lower mantle structure and the CMB undulations (Figure 5.15). Model *PSR.s6.cmb* includes up to harmonic degree 6 in CMB undulations, and thus has 49 additional model parameters, compared to *PSR.s6*.

## Maps at 2800 km

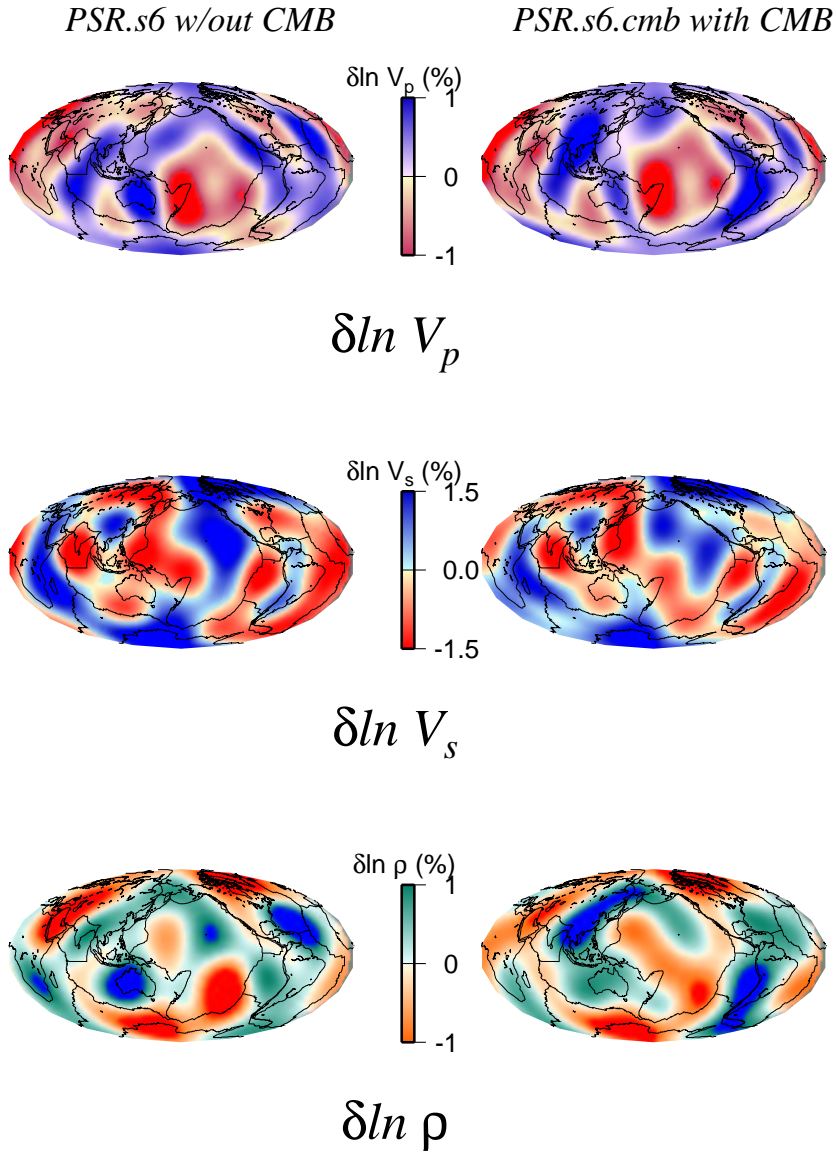


Figure 5.15: At 2800 km, Comparison of models PSR.s6, which assumes a smooth core-mantle boundary, and PSR.s6.cmb, for which boundary topography is included in the model parameterization. Degrees 1 through 6.

The mantle heterogeneity in the two models is very stable, except at depths near the very bottom of the mantle, illustrating the trade-offs between the capability of imaging volumetric structure and boundary deformation in the vicinity of the discontinuity. Although present at shallower depths around 1600-2000 km in *PSR.s6*, the  $c_2^2/s_2^2$  pattern of fast S-velocity perturbations surrounding a slow velocity central Pacific region commonly found in higher frequency seismic tomographic models such as SAW12D, S12WM13, or S16B30 (*Masters et al., 1996*) is not as clear in the model *PSR.s6* at the bottom of the mantle at 2800 km (Figure 5.15a). This  $c_2^2/s_2^2$  pattern at the bottom of the mantle is also present in the shear-velocity model derived from normal modes data by *Resovsky & Ritzwoller 1999b*, but their model has been damped to optimize consistency with mantle models SAW12D, SKS12WM13, and S16B30. Although we have applied damping to the model size, horizontal smoothing, and radial smoothing, we do not retrieve a  $c_2^2/s_2^2$  pattern near the core-mantle boundary in  $V_s$  of *PSR.s6*.

Including topography of core-mantle boundary in our models improves the model of S-velocity heterogeneity at the bottom of the mantle in the sense that at 2800 km, the fast velocity band extending North-South through the Pacific Ocean is removed. More specifically, while the even degree structure of  $\delta \ln V_s$  in *PSR.s6* and *PSR.s6.cmb* has remained somewhat consistent, the odd degrees 1 and 3 have not, and we note that most of the power of the CMB undulation solution is in degrees 1 and 3.

The effect of excluding CMB topography on the  $\delta \ln V_p$  model of *PSR.s6* can also be seen in the lower mantle as illustrated in Figure 5.15. The pattern of heterogeneity in the  $\delta \ln V_p$  model of *PSR.s6.cmb* exhibits fast velocities around a slow Pacific near the CMB. In their discussion of their S-velocity model *S16B30* (*Masters et al., 1996*), the authors confirm that the sensitivity of mode data to boundary topography introduces a trade-off with sensitivity to structure in the vicinity of the boundary. Stating that the boundary undulations are not well-constrained by their data set, they choose not to solve for boundary undulations at the time of producing *S16B30* (*/P16B30*). With the addition of the CMB undulation solution, a fast velocity region over Asia is more pronounced in  $\delta \ln V_p$  of *PSR.s6.cmb*. This fast velocity feature appears consistently in P-velocity models *P16B30*, *JLM4P6* (*Robertson & Woodhouse 1995*), the P-velocity component of *WE1997* (*Vasco & Johnson 1998*), and the P-velocity model derived from *MK12WM13* (*Su & Dziewonski 1997*).

#### 5.7.4 $\rho$ model of PSR.s6.cmb

Although our confidence in the retrieval of density structure is marginal, as discussed in a previous section, we see from Figure 5.12c that the density structure retrieved from *PSR.s6.cmb* is not unreasonable: patterns of high density anomalies in the mantle correspond to regions of down-going slabs in the mantle. High density features are present southwest of South America and Western

Pacific starting at about 250 km depth, in particular near the Tonga Trench. These features surrounding the Pacific extend all the way down to the base of the mantle. Again, we find that the density heterogeneity pattern at the base the mantle differs when we do not include CMB topography modeling. In *PSR.s6*, the density structure at 2800 km is similar to that in *PSR.s6.cmb*, except for the presence of high density extending northwesterly from Western South America, over the Hawaiian Islands, up to the Bering Sea. When the CMB topography is included in the model, as for *PSR.s6.cmb*, this density high is removed and the density pattern corresponding to the subduction of cold slabs is retained at 2800 km (Figure 5.15). There are high density features in the model which would not appear to be thermal in origin, assuming mantle geodynamic models driven by cold and dense downgoing slabs, and warm upwelling plumes originating at the core-mantle boundary. For example, there is high density at 2800 km in the region of the hypothesized origin of the Hawaiian Plume. Before concluding that these features are chemical in origin (*Ishii and Tromp, 1999*), extensive resolution tests must be analyzed for model robustness. We address resolution issues in Chapter 6.

### 5.7.5 Core-Mantle Boundary Topography

Inclusion of parameterization for core-mantle boundary topography improves our models of volumetric heterogeneity at the base of the mantle. In Figure

## CMB degrees 2 and 4

*PSR.s6.cmb*

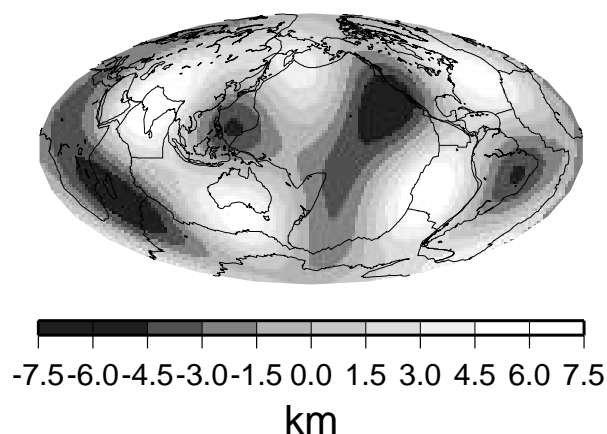


Figure 5.16: Even degrees 2 and 4 of the CMB undulations for model PSR.s6.cmb. Positive deformations indicate elevation (light), and negative deformations represent regions of depression (dark).

5.16, the deformations in degrees 2 and 4 on the core-mantle boundary are displayed for model PSR.s6.cmb, where positive deformations indicate areas of elevation, and negative deformations represent areas of depression. Only degrees 2 and 4 are shown because we have found that the degree 2 and 4 topographic undulations are stable throughout a number of inversion experiments using a number of various spatial parameterizations of our three-dimensional models, while odd degrees, which are constrained by only few coupled-modes are not as stable.

The prominent depressions are seen under the Philippine Sea where the Philippine Trench and New Guinea Trench merge at the surface of the Earth, and over South America, west of the Peru-Chile Trench in the direction of dip. There are two large regions of depressions, west of North America extending to the Tonga Trench region and over Africa, for which we do not have an obvious explanation based on surface tectonics. Nevertheless, our model of CMB topography is comparable in pattern and amplitude to the CMB maps from PcP travel time studies of *Obayashi and Fukao, 1997* and *Rodgers and Wahr, 1993*, particularly the depressions below South East Asia, South America, Africa, and the dominant degree 2 zonal component ( $s = 2, t = 0$ ). A depression in the Pacific west of North America is expressed in the *Rodgers and Wahr, 1993* CMB model from inversions of ISC PcP travel times. We also retrieve elevated topography in high northern latitudes, in agreement with *Obayashi and Fukao, 1997* and *Rodgers and Wahr, 1993*. *Obayashi and Fukao, 1997* interpret the dominant degree 2 zonal pattern in the CMB heterogeneity as possibly related to outer core fluid flow.

Our CMB amplitudes,  $\pm 7.5$  km, are high compared to independent constraints of the topographic amplitudes, such as from Earth tide and nutation measurements (*e.g. Wahr and de Vries, 1989*), which constrain the  $h_2^0$  coefficient of CMB topography to vary between 0.5-1.0 km. However, the residual variance of the model is essentially invariant for a range of amplitudes of the core-mantle

boundary undulations, and we can choose the CMB amplitude damping value which is consistent with independent studies of core mantle boundary topographic amplitudes such as the observations of the Earth's nutation.

The patterns of CMB topography presented by a number of authors (*Morelli and Dziewonski, 1987; Li et al., 1991b; Rodgers and Wahr, 1993; Obayashi and Fukao, 1997*) vary depending on what types of seismic data analyzed. In what follows, we discuss the stability of our model, with respect to spatial parameterizations of our models. In order to test the stability of the even degrees, the following experiments were performed: ones analogous to S.sclPR, PS.sclR, and PSR.noscl in which the CMB topography has been included as additional model parameters, for both even-degree only models (where coupled modes are not considered), and models which also retrieve odd degree structure. A model of Earth heterogeneity which includes parameterization for both CMB topography and outer core structure has also been computed to test mapping of possible outer core structure into the CMB parameterization. The degree 2 and 4 structure is extremely stable throughout all of these experiments.

Although the odd degree CMB topographic coefficients from the relevant parameterization experiments have also been stable, their amplitudes are almost two orders of magnitude too high. In what follows, we describe a resolution test, in which we find that we can reliably retrieve a small amplitude even degree signal. In a test of resolution, we take the product of an input model of mock



even degree CMB undulations with the resolution matrix constructed from our mode kernels for the parameterization for PSR.s6.cmb. While the input CMB model only includes even degrees 2 and 4 and zero values for odd degrees, the output model includes both even and odd degrees. Figure 5.17 displays the input map and output patterns in degrees 2 and 4, and demonstrates that the even degree pattern is well preserved.

While we have demonstrated that we can reliably retrieve an input model of CMB undulations, we'd also like to examine the trade-off between volumetric heterogeneity and boundary topography, but this time, with respect to the effects on the patterns of topography. Assuming now that the input CMB has zero topography, we test the resolution of our data set and see that the output model in Figure 5.18 shows depressions in the circum-Pacific region. This pattern is most likely a result of contamination from seismic velocity signals, which we will discuss in detail in Chapter 6. A comparison between the output models in Figures 5.18 and 5.17 assures us that for our data set, we can resolve trough and elevation peaks of the CMB over  $\sim 0.75$  km without being influenced by the contaminant signal. The output model of CMB undulations in Figure 5.18 is very similar to the CMB model derived from an earlier work in inversions of normal mode spectra for heterogeneity, *Li et al., 1991b* (Figure 12a). In *Li et al., 1991b*, 835 pre-1990 seismic spectra of 20 mantle modes were analyzed to invert for even degree  $V_s$  models of heterogeneity, where  $V_p$  and  $\rho$  perturbations

## CMB resolution degrees 2 and 4

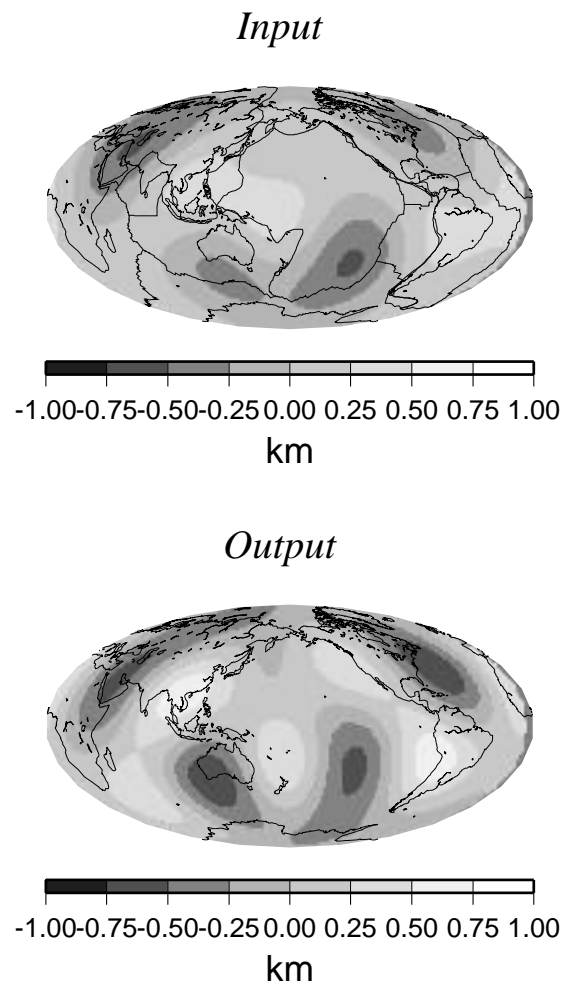
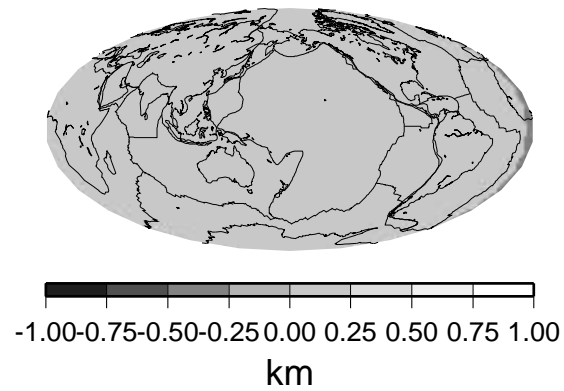


Figure 5.17: Resolution test of CMB topography. Negative values indicate depressions (dark) and positive values indicate elevations (light).

## CMB resolution degrees 2 and 4

*Input*



*Output*

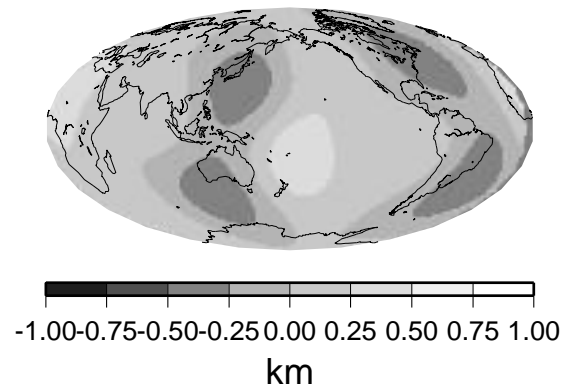


Figure 5.18: A second resolution test of CMB topography examining artifact CMB patterns. Negative values indicate depressions (dark) and positive values indicate elevation (light).

were scaled to  $V_s$  perturbations. Although they retrieve CMB amplitudes of  $\pm 3$  km, we cannot make direct comparisons of threshold sensitivity to contaminant signal amplitudes due to the differences in data set, and model parameterization. However, the difference in pattern between our CMB model and that of *Li et al., 1991b* can be explained by Figure 5.18, where we put forth the suggestion that they may have observed contamination from  $V_s$ .

### 5.7.6 Odd degree sensitivity

Although our mode data set is primarily sensitive to even degree structure from the self-coupling interaction of isolated modes, it is possible to infer odd degree structure from cross coupled modes. We find that for  $V_s$ , our solution for odd degree structure agrees well with that of SAW12D in the lower mantle. For inversions up to degree 4 harmonics involving coupled modes, the sensitivity to odd degree structure is limited to degree 1 and 3, and constrained only by two pairs of couple modes,  ${}_1S_5 - {}_2S_4$  and  ${}_1S_6 - {}_2S_5$ . The sensitivity of these two pairs of coupled modes is strong for  $V_s$  but very weak for  $V_p$  and  $\rho$  for degree 1 and 3 structure in the lower mantle (Figure 5.19). Including the coupled modes, the correlation of the  $V_s$  model from PSR.s6, to SAW12D in degree 1 and 3 structure is high in the lowermost mantle where the sensitivity to  $V_p$  is very low, and the  $V_s$  sensitivity dominates (Figure 5.20). This may suggest that because there is little sensitivity to  $V_p$  and  $\rho$  in degrees 1 and 3, there is much less trade-off with

$V_p$  and  $\rho$  in the  $V_s$  model. We also find that the even degree is stable when odd degree structure coefficients are added to the parameterization. On the other hand, the addition of the CMB topography to our model parameterization degrades the correlation of the odd degree structure with that of SAW12D. The model coefficients of the CMB topography in PSR.s6.cmb is dominated by odd degrees, but we have demonstrated that the even degree structure is well resolved in Figure 5.17, and contamination between even and odd degree CMB structure is negligible.

### 5.7.7 Outer Core

Although our data set consists of 'mantle modes', most of these modes also have sensitivity in the outer core. If the model parameterization only includes depths extending to the core-mantle boundary, outer core structure may be mapped into the coefficients of mantle structure. The outer core is assumed to be homogeneous because of the low viscosity and the vigorous convection of metallic iron required to support the geodynamo; there would be no outer core structure to contaminate the mantle models, in this case. *Stevenson (1987)* concluded from fluid dynamics considerations that lateral variations in the outer core are undetectable by seismology, but there may be limitations to the author's examination (*S. Zatman, personal communication*). Despite these assumptions,

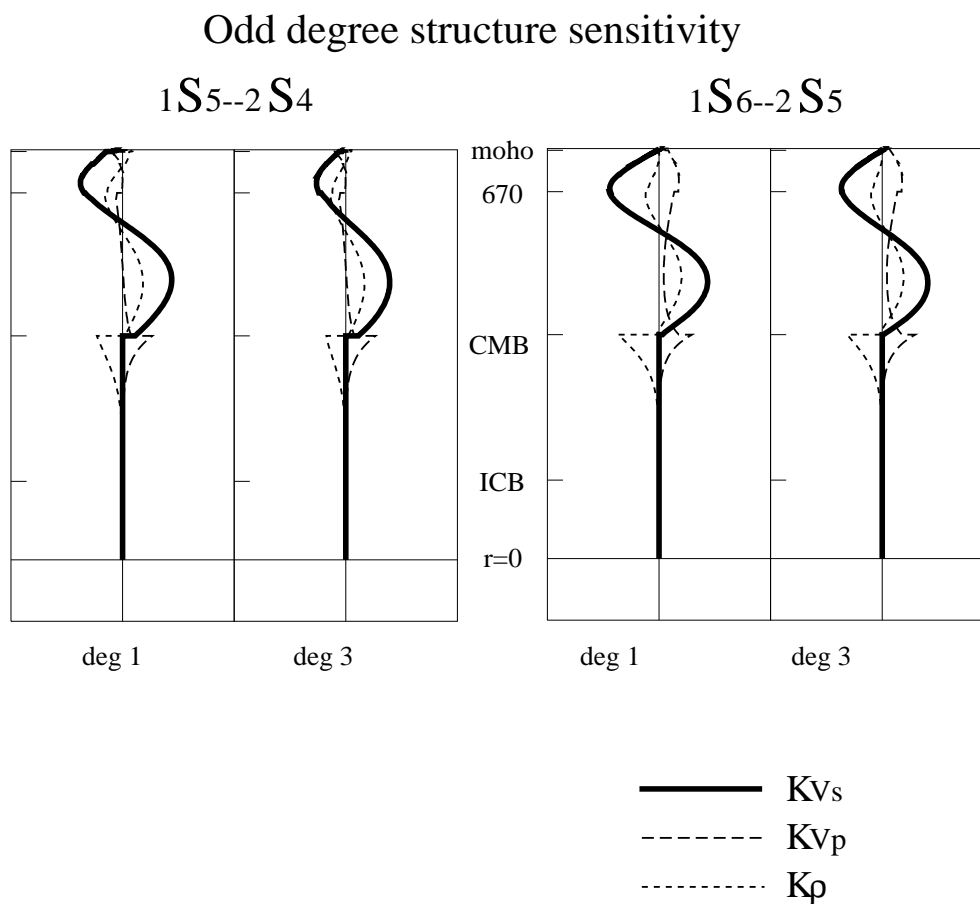


Figure 5.19: Two mode pairs in the coupled mode inversion,  ${}_1S_5-{}_2S_4$  and  ${}_1S_6-{}_2S_5$ , are sensitive to odd degree structure. The mode pairs,  ${}_1S_5-{}_2S_4$  and  ${}_1S_6-{}_2S_5$  give sensitivity to degrees 1 and 3 for our model PSR.s6.cmb and the sensitivity kernels ( $K_{V_s, V_p, \rho}$ ) plotted here show that most of the amplitude in odd degrees is in  $\delta \ln V_s$ .

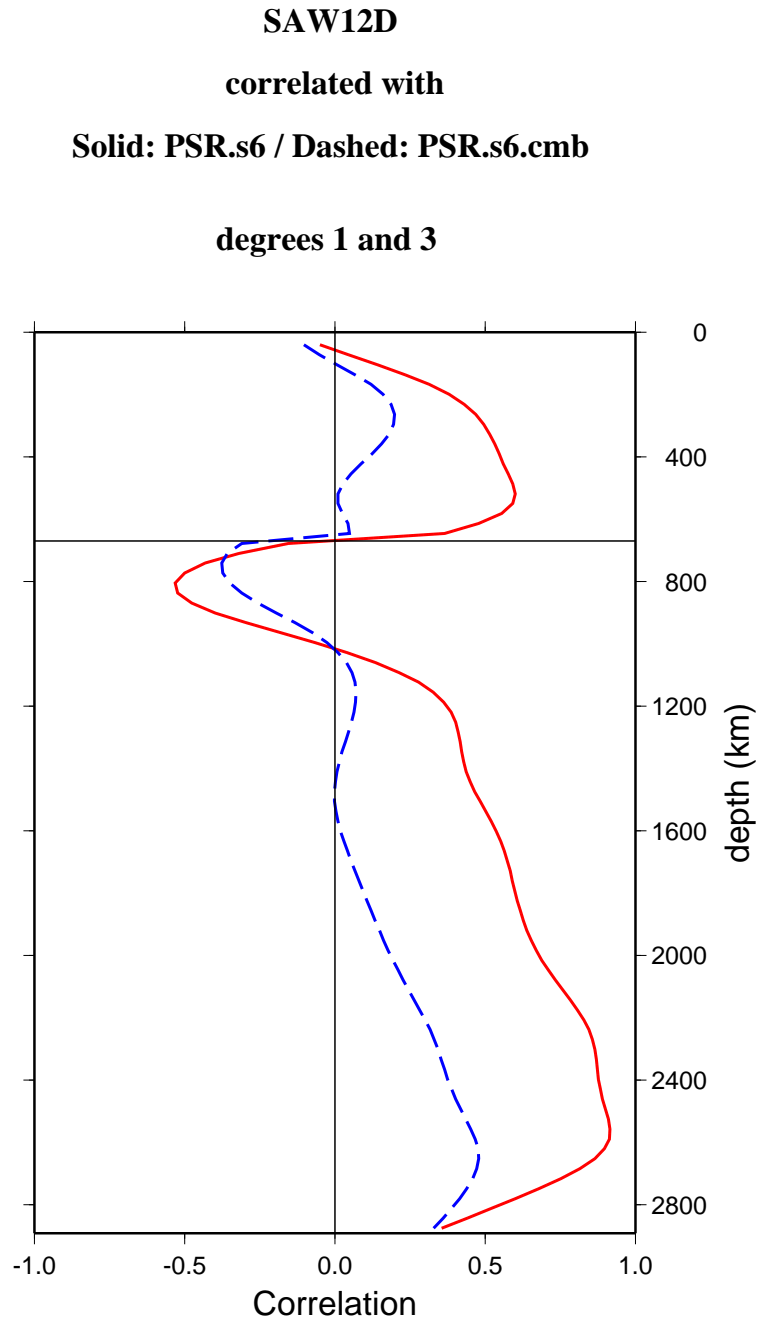


Figure 5.20: For  $V_s$  structure in odd degrees 1 and 3, the correlation between SAW12D and PSR.s6 in solid line, and the correlation between SAW12D and PSR.s6.cmb in dashed line. The CMB topography in PSR.s6.cmb is strong in odd degrees.

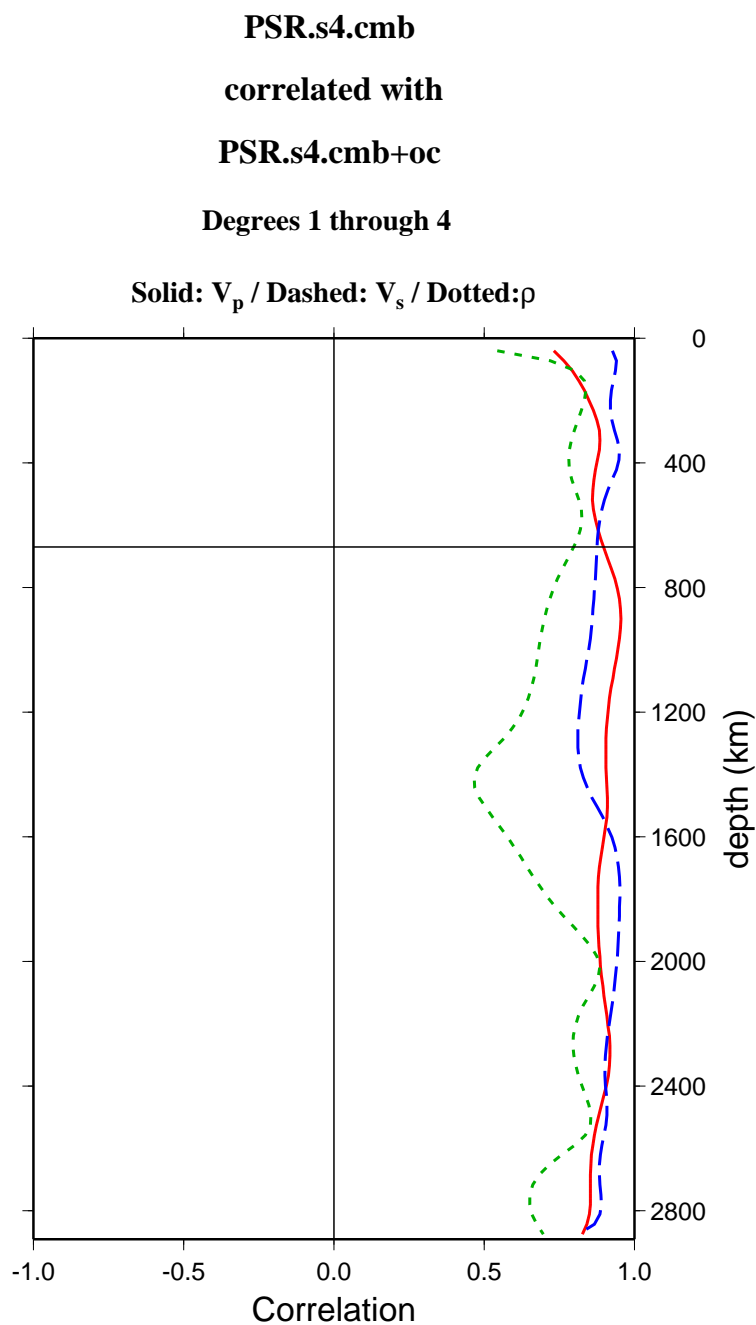


Figure 5.21: The correlation of mantle structure between a mantle model (*PSR.s4.cmb*) and a mantle model which includes outer core parameterization (*PSR.s4.cmb+oc*) for degrees 1 through 4. The solid line is the correlation in  $V_p$ , dashed line: in  $V_s$ , and dotted line: in  $\rho$ .



we have parameterized our models to include a layer , specifically parameterized by a zero order polynomial, in the outer core extending to  $\sim 200$  km below the core mantle boundary. By comparing the  $V_p$ ,  $V_s$ , and  $\rho$  models with and without the outer core parameterization, we find that the mantle structure is very stable for the seismic velocity perturbations, and that there exists a slight trade-off in density structure (Figure 5.21). The structure which is mapped into the outer core layer will be the subject of a future article.

## 5.8 Conclusions

We have shown that our data set of mode spectra has sensitivity to not only  $V_s$  structure, but to  $V_p$  structure as well. Inverting for structure using either only  $V_s$  or  $V_p$  sensitive modes confirms that the  $V_p$  structure obtained by jointly and independently inverting for  $V_s$ ,  $V_p$ , and  $\rho$  has more information than the 'noise' of  $V_s$  structure. We have presented our models of large scale  $V_p$ ,  $V_s$ , and density structure. The density models are stable throughout the inversion experiments. The final models are parameterized to degree 6 harmonics laterally and degree 7 Legendre polynomials radially, and include odd degree structure.

We find that the assumption that  $V_p$  and density variations scale uniformly with those of  $V_s$  introduces notable contamination into the  $V_s$  modeling, when compared to SAW12D. Our models of  $V_s$  are improved, in this sense, when solutions to  $V_s$ ,  $V_p$  and  $\rho$  inhomogeneities are found independently. The stabil-

ity of the resulting  $V_p$  tomographic model is demonstrated through its strong correlation with  $V_p$  structure inverted by using a subset of P-wave velocity sensitive modes with low S-wave velocity sensitivity. While it is difficult to perform the same type of comparison for the density models, as the amplitudes of  $V_s$  and/or  $V_p$  sensitivity dominate that of  $\rho$  for the modes used in this study ( ${}_0S$ ,  ${}_1S$ ,  ${}_2S$ ,  ${}_4S$ ,  ${}_5S$  branches), the density models remain stable throughout the numerous inversion experiments, and display features related to subducting slabs in the circum-Pacific.

Our density structure in the mantle does not agree with that of *Ishii and Tromp, 1999*, particularly at the depths immediately above the core-mantle boundary, although the topography of the CMB is parameterized in the model space in both our analysis and theirs. The anomalous high density structures at lowermost depths in the central Pacific and under Africa displayed in the *Ishii and Tromp, 1999* model is not prominent in our model. Although some of our models display similar features, we do not find that these features are stable. They disappear with the inclusion of CMB topography in model parameterization, and with our choice of damping values.

Our model of CMB structure agrees with the results of PcP travel time studies of *Obayashi and Fukao, 1997* and *Rodgers and Wahr, 1993*. We find that there is a dominant degree 2 zonal pattern in which polar regions are elevated, and this observation may indicate influences of outer core fluid flow

on the core mantle boundary topography, as suggested by *Obayashi and Fukao, 1997*. Regions of depression on the core mantle boundary are located beneath the Philippine Sea, where a junction of three trenches merge at the Earth's surface, and South America, in the dipping direction of the Peru-Chile Trench. Two other large regions of depressions, west of North America and over Africa, can not be explained by surface tectonics. The differences in pattern between the CMB structure retrieved in our model PSR.s6.cmb and in SAT of *Li et al., 1991b* for which type of data and inversion technique are essentially the same, may be due to a contaminant signal in the model SAT. We find that the degree 2 and 4 coefficients of our CMB topography structure to be very stable throughout a number of model parameterizations. The issue of uncertainties in the final density models due to *a priori* assumptions imposed on inversions for density structure from normal mode splitting coefficients, as performed by *Ishii and Tromp, 1999*, has been addressed by *Resovsky and Ritzwoller, 1999a*. The problems induced from *a priori* assumptions have further impact on the inversions for structure from splitting coefficients, as the regularization schemes used to solve for splitting coefficients from normal mode spectra are unaccounted for in this type of analysis, whereas the method of direct inversion from normal mode spectra to Earth structure, as we have used, allows us to better understand the trade-offs associated with our *a priori* assumptions. In the next chapter, we will address the issues of *a priori* assumptions and their impact on resolvable

model parameters.

Table 5.4: For each mode in column 1, the residual variance of predicted spectra to the data spectra, computed from model *PSR.s6.cmb*, is reported in column 3. The total residual variance for this model is 0.227. The central reference frequency of each mode, with respect to PREM, is listed in the 2nd column.

Mode	Reference Frequency (mHz)	Data misfit
${}_0S_3$	0.469	0.448
${}_0S_4$	0.647	0.283
${}_0S_5$	0.840	0.182
${}_0S_6$	1.038	0.217
${}_0S_9$	1.578	0.103
${}_0S_{27}$	3.544	0.227
${}_1S_2$	0.680	0.418
${}_1S_4$	1.173	0.106
${}_1S_7$	1.656	0.202
${}_1S_8$	1.799	0.177
${}_1S_9$	1.964	0.180
${}_2S_6$	1.681	0.161
${}_2S_{12}$	2.737	0.153
${}_2S_{13}$	2.900	0.215
${}_4S_2$	1.722	0.375
${}_4S_4$	2.280	0.164
${}_4S_9$	3.709	0.257
${}_4S_{11}$	4.010	0.764
${}_5S_3$	2.170	0.115
${}_5S_4$	2.380	0.089
${}_5S_5$	2.703	0.051
${}_5S_6$	3.011	0.159
${}_5S_7$	3.291	0.150
${}_5S_8$	3.526	0.195

Table 5.4 continued

Mode(s)	Reference Frequency (mHz)	Data misfit
${}_5S_{12}$	4.696	0.239
${}_6S_{10}$	4.211	0.298
${}_7S_4$	3.413	0.353
${}_7S_5$	3.660	0.308
${}_8S_7$	4.650	0.355
${}_9S_{14}$	6.768	0.108
${}_3S_1 - {}_1S_3$	0.944, 0.940	0.184
${}_2S_4 - {}_1S_5$	1.379, 1.370	0.141
${}_2S_5 - {}_1S_6$	1.515, 1.522	0.134
${}_4S_3 - {}_2S_8$	2.049, 2.049	0.080
${}_6S_3 - {}_3S_8$	2.822, 2.820	0.269
${}_0S_7 - {}_2S_3$	1.232, 1.242	0.200
${}_2S_{10} - {}_4S_5$	2.403, 2.411	0.091

## Chapter 6

### The resolution of density anomalies in the Earth's mantle using normal mode data

#### 6.1 Introduction

The issue of whether lateral variations in density in the mantle can be resolved from normal mode data has recently received renewed attention, in particular with the work of *Ishii and Tromp, 1998, 1999*. In their recently published paper, these authors present a degree 6 model of density throughout the mantle, derived from inversion of normal mode splitting coefficients. This model presents unexpected features in the lowermost mantle, namely two large "blobs" of high density material centered in the Pacific and under Africa, that, if real, would have important consequences for the dynamics of the mantle. *Ishii and Tromp, 1999* argue for the robustness of their model, on the basis of numerous experiments, including checkerboard resolution tests and exploration of different parameterization schemes.

Whether lateral variations in density can be resolved from normal mode

data has long been the subject of debate. *Resovsky and Ritzwoller, 1999* have recently presented the results of tests which show that the retrieved density structure is very sensitive to the regularization scheme used in the inversion. Imposed *a priori* constraints on the location and size of density heterogeneity have a strong effect on the resulting models, which, while providing equal fit to the data, can be significantly different. *Ishii and Tromp, 1999* however, argue that their density model is weakly dependent on their starting model.

In what follows, we present the results of a series of tests in which we have explored more fully the structure of the resolution matrix than can be done with checkerboard tests. Because in the case of non-linear inversions, the resolution matrix approach only allows us to investigate the problem approximately, we also present results of tests in which we compute synthetic seismograms for realistic Earth models and invert them under the same conditions as the real data.

## 6.2 Tests with resolution matrices

### 6.2.1 Resolution matrix

The resolution matrix is a useful tool to assess the leakage between model parameters in a generalized inversion framework. Indeed, the solution  $\mathbf{m}_{est}$  to the inverse problem  $\mathbf{d}_{obs} = \mathbf{A}\mathbf{m}$ , where  $\mathbf{A}$  is a linearized data kernel,  $\mathbf{d}_{obs}$  is the data vector, and  $\mathbf{m}$  the model vector, can be written as:



$$\mathbf{m}_{est} = (\mathbf{A}^T \mathbf{A} + \mathbf{C}_m^{-1})^{-1} \mathbf{A}^T \mathbf{d}_{obs} \quad (6.1)$$

where  $\mathbf{C}_m^{-1}$  is the matrix of damping parameters. The relation between the vector of estimated model parameters  $\mathbf{m}_{est}$  and the true model  $\mathbf{m}_{true}$ , for a given parameterization and underlying theory, is then:

$$\mathbf{m}_{est} = (\mathbf{A}^T \mathbf{A} + \mathbf{C}_m^{-1})^{-1} \mathbf{A}^T \mathbf{A} \mathbf{m}_{true}. \quad (6.2)$$

The  $M \times M$  model resolution matrix  $\mathbf{R}$ , where  $M$  is the number of unknown parameters, is defined as

$$\mathbf{R} = (\mathbf{A}^T \mathbf{A} + \mathbf{C}_m^{-1})^{-1} \mathbf{A}^T \mathbf{A} \quad (6.3)$$

so that

$$\mathbf{m}_{est} = \mathbf{R} \mathbf{m}_{true}. \quad (6.4)$$

If  $\mathbf{R} = \mathbf{I}$ , where  $\mathbf{I}$  is the identity matrix, then each model parameter is perfectly resolved. In practice,  $\mathbf{R} = \mathbf{I}$  has non zero off-diagonal terms, and their size relative to each other and to the diagonal terms indicates the amount of contamination (or "covariance") between the different parameters as determined by inversion.

In our particular problem, we invert simultaneously for structure in  $V_P$ ,  $V_S$  and  $\rho$ , and wish to investigate the level of contamination between these parameters. The model vector is arranged as follows:

$$\mathbf{m} = [{}_pV_{Ps}^t, {}_pV_{Ss}^t, {}_p\rho_s^t], \quad (6.5)$$

where the indices  $s, t, p$  refer to the parameterization of the model. In our studies, we have chosen spherical harmonics laterally, and Legendre polynomials vertically. The maximum degree ( $s_{max} = 6$ ) of the spherical harmonics expansion is chosen in view of the sensitivity of the particular mode data set we are considering, given that a particular mode of angular order  $l$  is sensitive to at most lateral heterogeneity of degree  $2l$ . The maximum order of the radial polynomial expansion is commensurate with the maximum radial order  $n$  of the modes in our data set ( $p_{max} = 7$ ). We will compare results for  $p_{max} = 7$  and  $p_{max} = 10$ , as it has been argued (e.g. *Ishii and Tromp, 1999*) that more stable results can be obtained by overparameterizing the model and then damping more strongly.

The resolution equation is then:

$$\begin{bmatrix} {}_pV_{Ps}^t \\ {}_pV_{Ss}^t \\ {}_p\rho_s^t \end{bmatrix}_{est} = \begin{bmatrix} R_P & \emptyset_{SP} & \emptyset_{RP} \\ \emptyset_{PS} & R_S & \emptyset_{RS} \\ \emptyset_{PR} & \emptyset_{SR} & R_R \end{bmatrix} \begin{bmatrix} {}_pV_{Ps}^t \\ {}_pV_{Ss}^t \\ {}_p\rho_s^t \end{bmatrix}_{true} \quad (6.6)$$

where  $R_P, R_S$ , and  $R_R$  are resolution submatrices for  ${}_pV_{Ps}^t$ ,  ${}_pV_{Ss}^t$ , and  ${}_p\rho_s^t$  respectively, and non-zero values in  $\emptyset_{PS}$  are the covariances which would map  $V_P$  structure into  $V_S$  structure, and so on. Of course, the  $\emptyset$ 's are zero in an ideal resolution matrix.

### Imposing *a priori* distributions

Since the resolution matrix is a function of both the data kernels and the *a priori* model covariance matrix,  $C_m^{-1}$ , it is important to carefully choose the *a priori* damping parameters so as to obtain, inasmuch as possible,  $\mathbf{R} \approx \mathbf{I}$ .

To do so, we consider a "realistic" synthetic model, for which we choose S velocity ( $V_S$ ) to be that of model SAW12D (*Li and Romanowicz, 1996*), P velocity ( $V_P$ ) to be that of P16B30 (*Masters et al., 1996*). A mock density model ( $\rho$ ) is constructed so that the root-mean-square amplitudes are about 25% of  $V_S$ , a common assumption in low-frequency seismology (e.g. *Li et al., 1991*) that is in agreement with laboratory measurements at shallow mantle pressure and temperatures. The mock density perturbations are constructed by permuting and scaling (to 25%) coefficients of  $V_s$  model SAW12D so that the actual patterns of heterogeneity are not correlated with SAW12D, and we name this model R25. As mentioned previously, we consider two different spatial parameterizations: 1)  $s_{max} = 6, p_{max} = 7$  (Experiment A), and 2)  $s_{max} = 6, p_{max} = 10$  (Experiment B). The resolution matrix is computed using the data kernels corresponding to our data set of 44 spheroidal mode spectra.

Damping parameters are defined separately for  $\delta V_P, \delta V_S$ , and  $\delta \rho$  and chosen in such a fashion as to best recover the rms amplitudes of the true model for even degrees (2,4,6) after applying the resolution matrix. We only consider norm damping ( $\eta_1$  in equation (4.8)) and we find that values of  $\eta_1^P = \eta_1^S = \eta_1^R = 1$  are

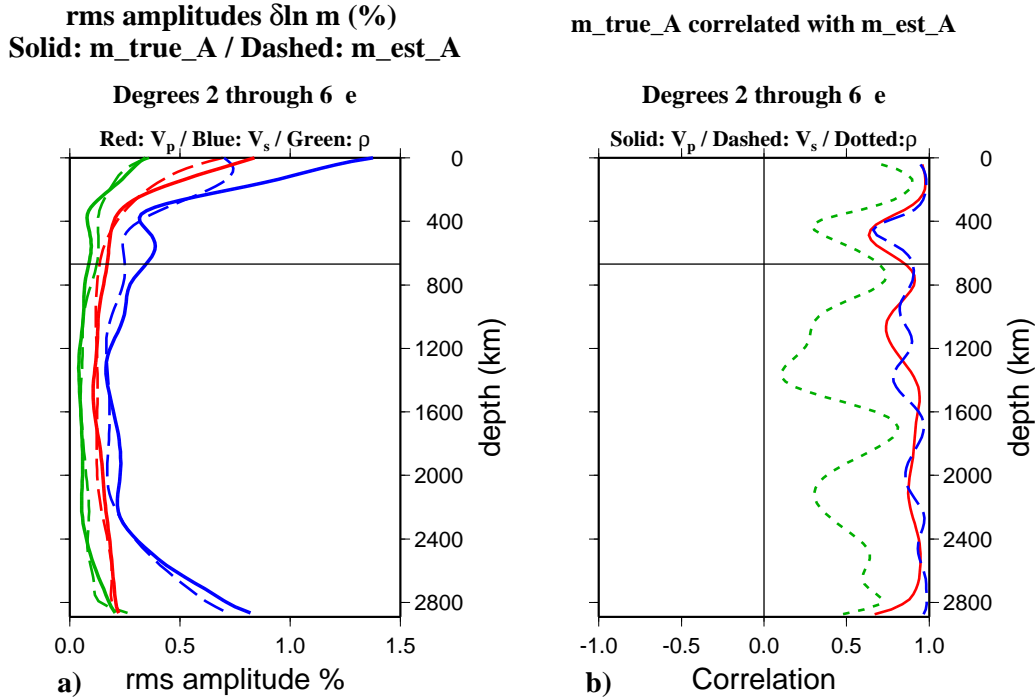


Figure 6.1: a) For Experiment A, the root mean squared amplitudes of an input model  $m_{true}$  in solid lines, and output model  $m_{est}$  from a resolution matrix test, in dashed lines. The blue lines are  $\delta V_s$ , the red lines are  $\delta V_p$ , and the green lines are  $\delta \rho$  rms amplitudes. See Table ?? for description of input models. b) The correlation of  $m_{true}$  with  $m_{est}$ . The blue dashed line is the correlation of  $\delta V_s$  between the input and output models, red solid line is for  $\delta V_p$ , and the green dotted line is for  $\delta \rho$ .

adequate for both spatial parameterizations (Figures ??a and ??a). The odd degree structure amplitudes are slightly overestimated due to the inadequate constraints from only two mode pairs ( $_1S_4 - _2S_5$  and  $_1S_5 - _2S_6$  for degrees 1, 3, and 5, and three mode pairs ( $_4S_3 - _2S_8$ ,  $_6S_3 - _3S_8$ , and  $_2S_{10} - _4S_5$ ) for degree 5. It is interesting to note that in the depth ranges in which the rms amplitudes in  $\delta V_P$  and  $\delta V_S$  are decreased, the amplitudes in  $\delta \rho$  are increased (400-1200 km, and 1600-2400 km depth), potentially indicating leakage from the

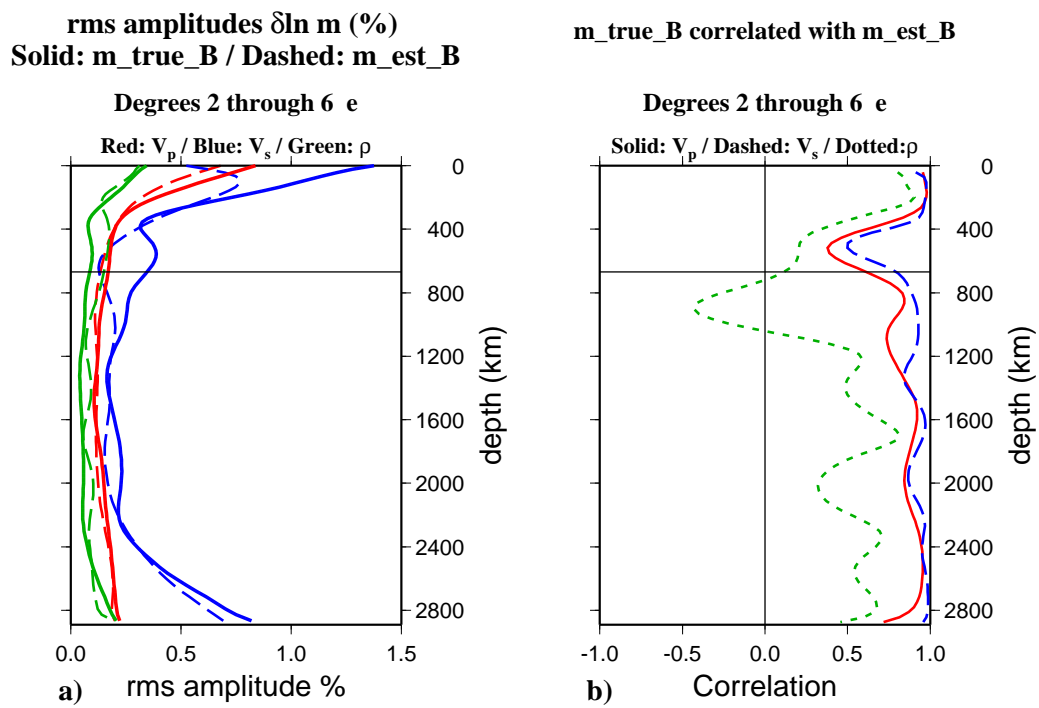


Figure 6.2: For Experiment B, the same as in Figure ??.

former to the latter. In Figures ??b and ??b, the correlations between  $\mathbf{m}_{true}$  and  $\mathbf{m}_{est}$  are plotted for spatial parameterizations  $s_{max} = 6, p_{max} = 7$ , and  $s_{max} = 6, p_{max} = 10$  respectively. We recover perturbations in  $V_P$  and  $V_S$  well for the spatial parameterization  $s_{max} = 6, p_{max} = 7$ , (correlation coefficients of 75%-99%), and perturbations in  $\rho$  are recovered with  $\sim 60\%$  correlation. For the spatial parameterization  $s_{max} = 6, p_{max} = 10$ , we can still recover perturbations in  $V_P$  and  $V_S$  sufficiently, although in the depth range 400-670 km, the correlation drops to  $\sim 50\%$ . Perturbations in  $\rho$  in the upper half of the mantle are poorly recovered in this parameterization. Clearly, adding vertical smoothing is necessary to compensate for overparameterization in the vertical direction.

If the perturbations in  $\rho$  in our input model  $\mathbf{m}_{true}$ , are scaled exactly to those of our input  $\delta V_S$  model, a resolution experiment on such an  $\mathbf{m}_{true}$  is insufficient to assess the leakage of  $V_S$  and  $V_P$  structure into  $\rho$ . However, it gives us an opportunity to examine the structure of the resolution matrix, which is independent of the input model coefficients. The resolution matrix is presented in Figure ??, which shows that the part of the matrix corresponding to  $V_S$  and  $V_P$  has a structure close to that of an identity matrix, with strongest values on the diagonal, and generally weak cross-terms  $\emptyset_{SP}$  and  $\emptyset_{PS}$ . On the other hand, the density sub-matrix shows both much smaller values on the diagonal, compared to  $V_S$  and  $V_P$ , and off-diagonal terms  $\emptyset_{RP}$ ,  $\emptyset_{RS}...$  which are small but commensurate with the diagonal terms. The structure of the resolution

matrix indicates that density cannot be resolved as well as velocity structure. Choosing the relative level of damping for velocities and density will therefore have a strong effect on the level of contamination present in the retrieved density structure.

Many authors perform checkerboard tests to assess the resolution of their models. In this kind of test, the model vector  $\mathbf{m}_{true}$  is sparsely populated by non zero coefficients  ${}_pm_s^t$ . For example, a checkerboard model of  $s = 4$ ,  $t = 4$ , and  $p = 7$  will consist of non-zero values for  ${}_pm_4^4$  and  ${}_pm_4^{-4}$  for  $0 \leq p \leq 7$ . This gives 16 non-zero elements in  $\mathbf{m}_{true}$ , of dimension  $M = 200$  ( $M = (s+1)^2(p+1)$ ). The remaining 184 elements of  $\mathbf{m}_{true}$  are zero. Then, many non-zero off-diagonal elements in  $\mathbf{R}$  can be neutralized by the product with zero elements in  $\mathbf{m}_{true}$ , and the covariances in  $\mathbf{R}$  may not be found by this type of test, even if it is performed at several degrees  $s$ .

Also, one may introduce a checkerboard model for  $\delta V_P$  only, where  $\delta V_S = 0$  and  $\delta \rho = 0$  in  $\mathbf{m}_{true}$ , to analyze the possible mapping of  $V_P$  structure into  $V_S$  and  $\rho$  structure, or introduce a checkerboard pattern for  $\delta V_S$  only to analyze the possible mapping of  $V_S$  structure into  $V_P$  and  $\rho$  structure, and so on (*Ishii and Tromp, 1999*). Then, for a checkerboard pattern  $s = 4$ ,  $t = 4$ , and  $p = 7$  in only one physical parameter vector, there are 16 non-zero values populating  $\mathbf{m}_{true}$  of dimension  $M = 600$  ( $M = (s+1)^2(p+1) \times 3$ ). Off-diagonal elements in  $\mathbf{R}$  can be missed, unless checkerboard tests are run for each model coefficient, which is

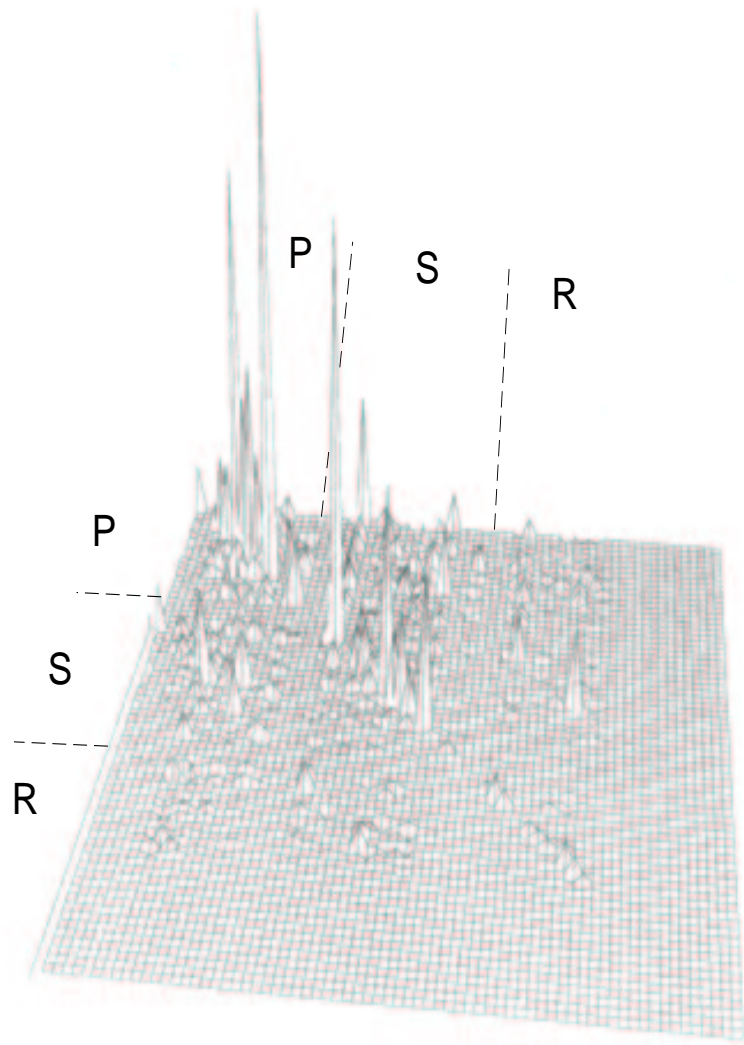


Figure 6.3: A visualization of a resolution matrix for 44 spheroidal modes used in this study.



not generally done. In other words, the mapping between physical parameters is not fully explored.

Instead of using a checkerboard model, in a first set of experiments, we choose to fully populate  $\delta V_P$  (respectively  $\delta V_S$  and  $\delta \rho$ ) with coefficients of an aspherical model, keeping the other parameters zero. We can thus test how well we can resolve each parameter, independently of the others, and how much is mapped into the others. Our input models are therefore, respectively  $\mathbf{m}_{true}^P = [\delta V_P, \emptyset, \emptyset]$ ,  $\mathbf{m}_{true}^S = [\emptyset, \delta V_S, \emptyset]$  and  $\mathbf{m}_{true}^R = [\emptyset, \emptyset, \delta \rho]$ . The same model of heterogeneity is used in all three cases, but the amplitudes are scaled according to  $V_P = 0.5 V_S$ , and  $\rho = 0.25 V_S$ , to achieve realistic rms levels in the respective parameters being tested. Resolution experiments with parameterizations A and B, as defined above, are performed in each case.

In Figures ??– ??, we plot the results of the three resolution tests using  $\mathbf{m}_{true}^P$ ,  $\mathbf{m}_{true}^S$ , and  $\mathbf{m}_{true}^R$  respectively for  $s_{max} = 6, p_{max} = 7$ . The legend scale for heterogeneity for  $\delta \ln V_P$  is  $\pm 1\%$ , for  $\delta V_S$  is  $\pm 1.5\%$ , and for  $\delta \rho$  is  $\pm 0.5\%$ . The color scale is chosen so as to correspond to expected amplitudes for each physical parameter. Figure ?? shows that  $\delta V_P$  is well recovered, but there is some contamination into  $\delta V_{S_{est}}$  and  $\delta \rho_{est}$ , as expected from the visualization of **R**. The amplitude of contamination into  $\delta V_{S_{est}}$  is very small, and is well below the level of signal obtained in real data inversions, so it should not be a problem. The amplitude of contamination into  $\delta \rho_{est}$  is also not very large, but patterns

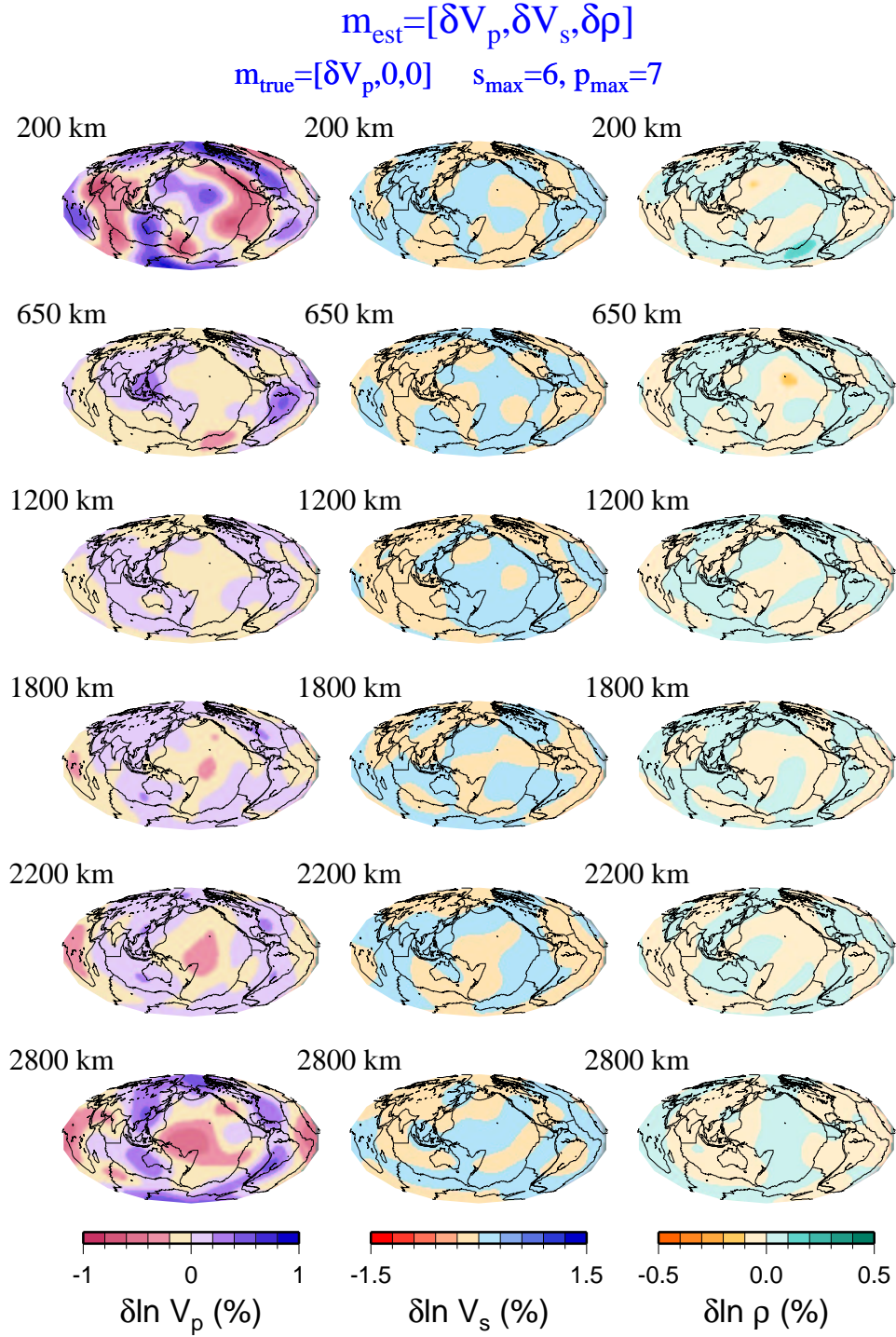


Figure 6.4: The output model of perturbations in  $V_p$ , left column,  $V_s$ , middle column, and  $\rho$ , right column, for an input model  $\mathbf{m}_{\text{true}} = [\delta V_p, 0, 0]$ , where  $\delta V_p$  is 0.5\*SAW12D (*Li and Romanowicz, 1996*). The spatial parameterization for the resolution matrix is  $s_{\text{max}} = 6, p_{\text{max}} = 7$ .

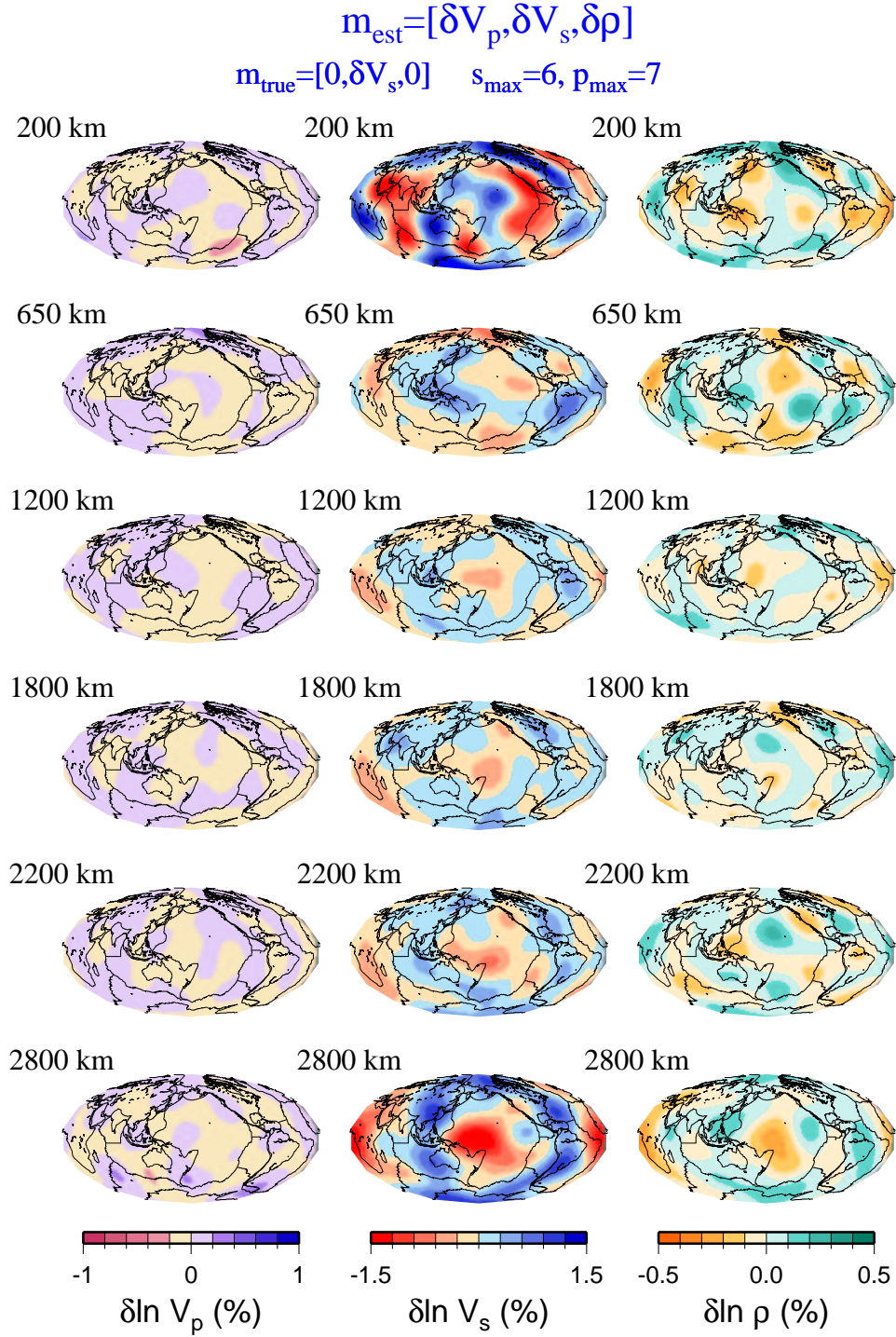


Figure 6.5: The output model of perturbations in  $V_p$ , left column,  $V_s$ , middle column, and  $\rho$ , right column, for an input model  $\mathbf{m}_{\text{true}} = [0, \delta V_s, 0]$ , where  $\delta V_s$  is SAW12D (*Li and Romanowicz, 1996*). The spatial parameterization for the resolution matrix is  $s_{\text{max}} = 6, p_{\text{max}} = 7$ .

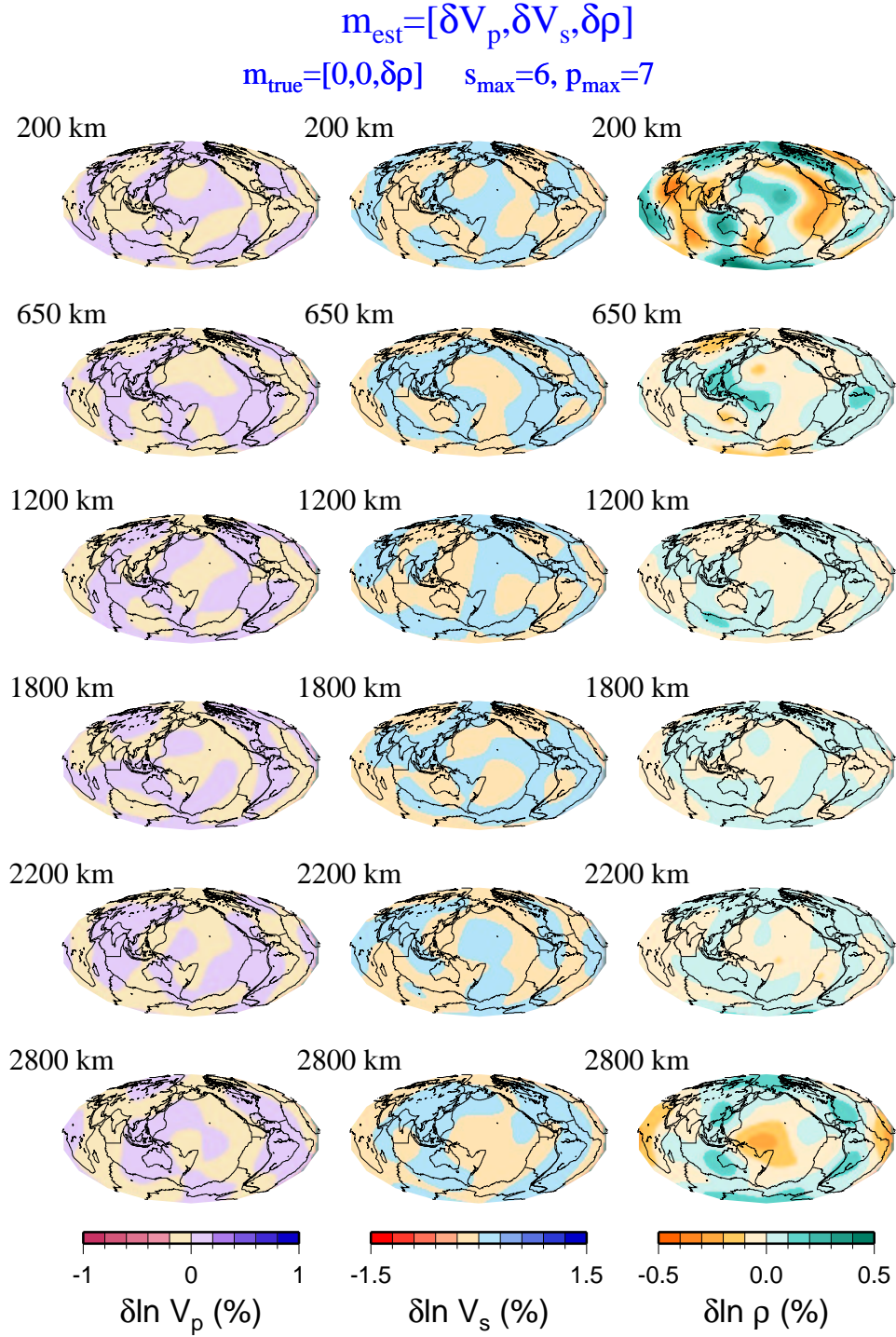


Figure 6.6: The output model of perturbations in  $V_p$ , left column,  $V_s$ , middle column, and  $\rho$ , right column, for an input model  $\mathbf{m}_{\text{true}} = [0, 0, \delta \rho]$ , where  $\delta \rho$  is 0.25\*SAW12D (*Li and Romanowicz, 1996*). The spatial parameterization for the resolution matrix is  $s_{\text{max}} = 6$ , and  $p_{\text{max}} = 7$ .



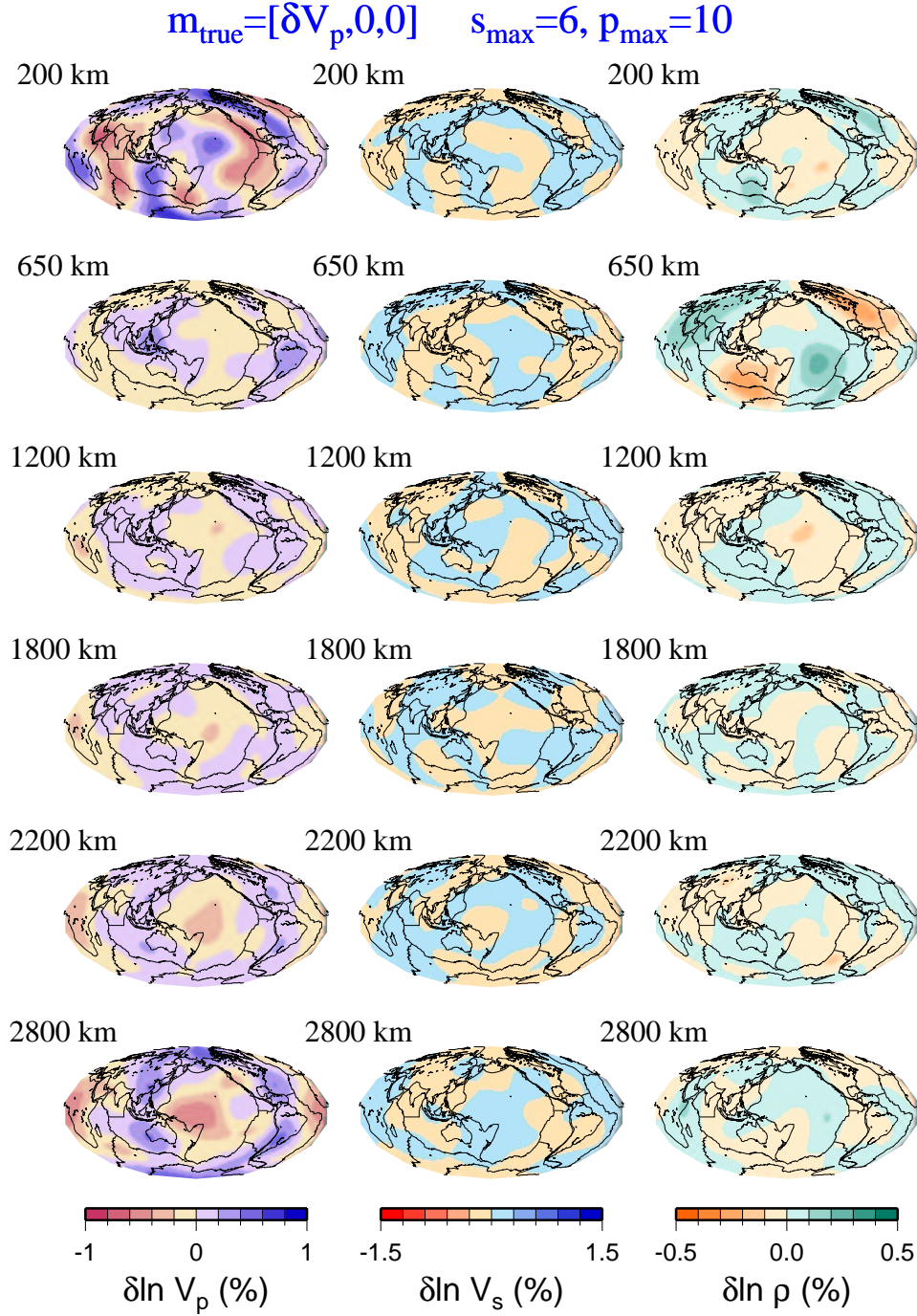


Figure 6.7: The output model of perturbations in  $V_p$ , left column,  $V_s$ , middle column, and  $\rho$ , right column, for an input model  $\mathbf{m}_{\text{true}} = [\delta V_p, 0, 0]$ , where  $\delta V_p$  is 0.5\*SAW12D (*Li and Romanowicz, 1996*). The spatial parameterization for the resolution matrix is  $s_{\text{max}} = 6, p_{\text{max}} = 10$ .

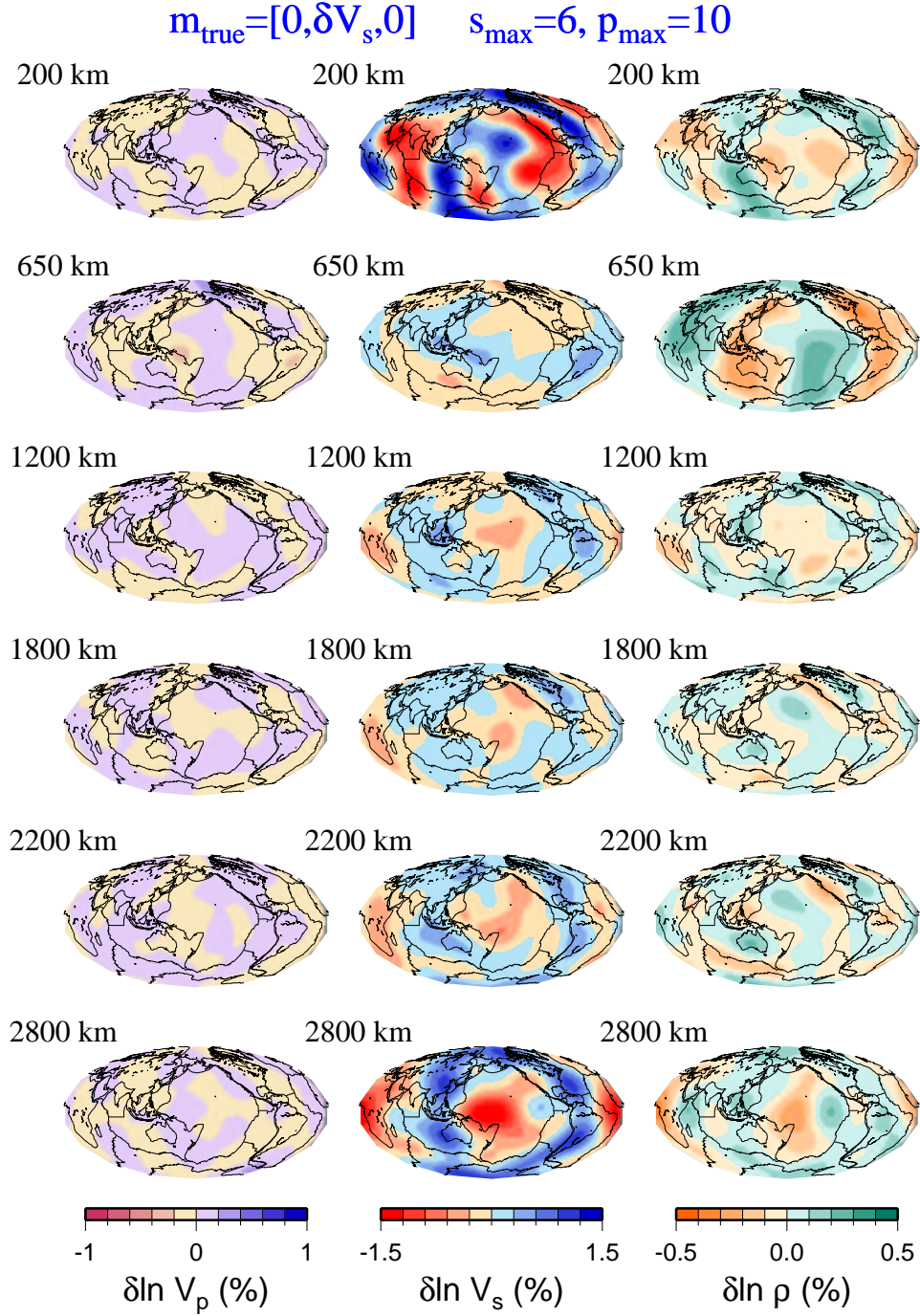


Figure 6.8: The output model of perturbations in  $V_p$ , left column,  $V_s$ , middle column, and  $\rho$ , right column, for an input model  $\mathbf{m}_{\text{true}} = [0, \delta V_s, 0]$ , where  $\delta V_s$  is SAW12D (*Li and Romanowicz, 1996*). The spatial parameterization for the resolution matrix is  $s_{\text{max}} = 6, p_{\text{max}} = 10$ .

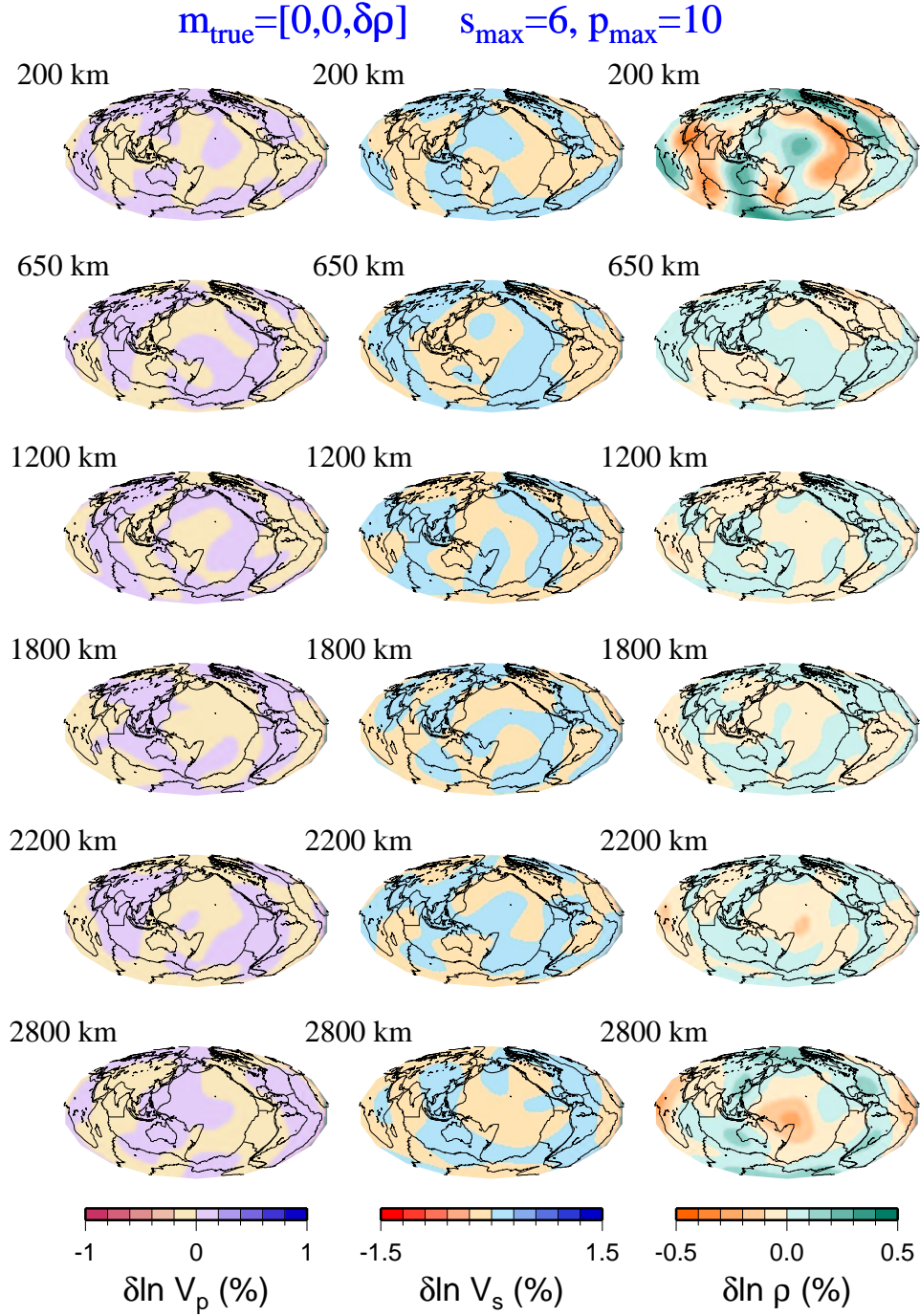


Figure 6.9: The output model of perturbations in  $V_p$ , left column,  $V_s$ , middle column, and  $\rho$ , right column, for an input model  $\mathbf{m}_{\text{true}} = [0, 0, \delta\rho]$ , where  $\delta\rho$  is 0.25\*SAW12D (*Li and Romanowicz, 1996*). The spatial parameterization for the resolution matrix is  $s_{\text{max}} = 6, p_{\text{max}} = 10$ .

at certain depths, particularly at 2800 km, are reminiscent of patterns from recent density models inverted from normal mode splitting coefficients (*Ishii and Tromp, 1999*), where high density features are located over Africa, and the Pacific basin region. In the upper mantle, there is significant contamination of  $\delta V_P$  patterns into  $\delta\rho$ . In Figure ??,  $\delta V_S$  is well resolved, with insignificant contamination into  $\delta V_{P_{est}}$ . The contamination amplitude into  $\delta\rho_{est}$  is somewhat higher, and the patterns mapped into the density model appear as high densities in areas of slab subduction in the circum-Pacific regions, especially at the bottom of the mantle. In the upper mantle, the same patterns of contamination in  $\delta\rho$  from  $\delta V_S$  appear as in Figure ??, but at somewhat stronger amplitudes. Finally, in Figure ??, we see that  $\delta\rho$  can be recovered in the absence of  $\delta V_S$  and  $\delta V_P$  structure, and there is not significant contamination into  $\delta V_{P_{est}}$  and  $\delta V_{S_{est}}$  in amplitude and pattern.

The results of an analogous experiment are shown in Figures ??-?? for spatial parameterization  $s_{max} = 6, p_{max} = 10$ , and the contamination effects are similar to the effects for spatial parameterization  $s_{max} = 6, p_{max} = 7$ .

### 6.2.2 Cumulative contamination

As seismic velocity structure in the Earth is well-documented (*Su et al., 1994; Li and Romanowicz, 1996; Masters et al., 1996; Dziewonski et al., 1997; Vasco and Johnson, 1997; van der Hilst et al., 1997*), the study of cumulative



Experi- ment	Spatial Para- meterization		$\delta V_p^{true}$ model	$\delta V_s^{true}$ model		$\delta \rho^{true}$ model		
	$s = 6$ $p = 7$	$s = 6$ $p = 10$	P16B30 <sup>1</sup>	SAW12D <sup>2</sup>	SH12- WM13 <sup>3</sup>	0	R25	R50
Resolution matrix tests								
A	★		★	★			★	
B		★	★	★			★	
C	★		★	★		★		
D		★	★	★		★		
E	★		★		★	★		
F		★	★		★	★		
H	★		★	★				★
I		★	★	★				★
Inversions w/ synthetic seismograms								
J	★		★		★	★		
K		★	★		★	★		

Table 6.1: Experiments of input  $m_{true} = [\delta V_p, \delta V_s, \delta \rho]$  are tabulated. For all experiments, the same norm damping is used for  $\delta V_p, \delta V_s, \delta \rho$  in the determination of  $m_{est}$ . The  $\delta V_p$  and  $\delta V_s$  models are from <sup>1</sup>*G. Masters and G. Laske, personal communication*, <sup>2</sup>*Li and Romanowicz, 1996*, <sup>3</sup>*Su and Dziewonski, 1994*.

contamination of  $\delta V_P$  and  $\delta V_S$  into  $\delta \rho$  can be particularly informative. To investigate the latter, we have performed a series of tests (labeled C-J), in which we vary the depth parameterization ( $p_{max} = 7$  versus  $p_{max} = 10$ ), the input  $\delta V_S$  model, keeping the input model in  $\rho$  to be zero. Table ?? describes the details of each experiment.

The comparison of the models obtained in experiments C,D (same initial models, different depth parameterization) with those of experiments A and B respectively, indicates that the velocity structures are well recovered, but a spurious density structure is introduced in C,D. This density structure is well correlated with that obtained in A, B, where the starting model was a realistic

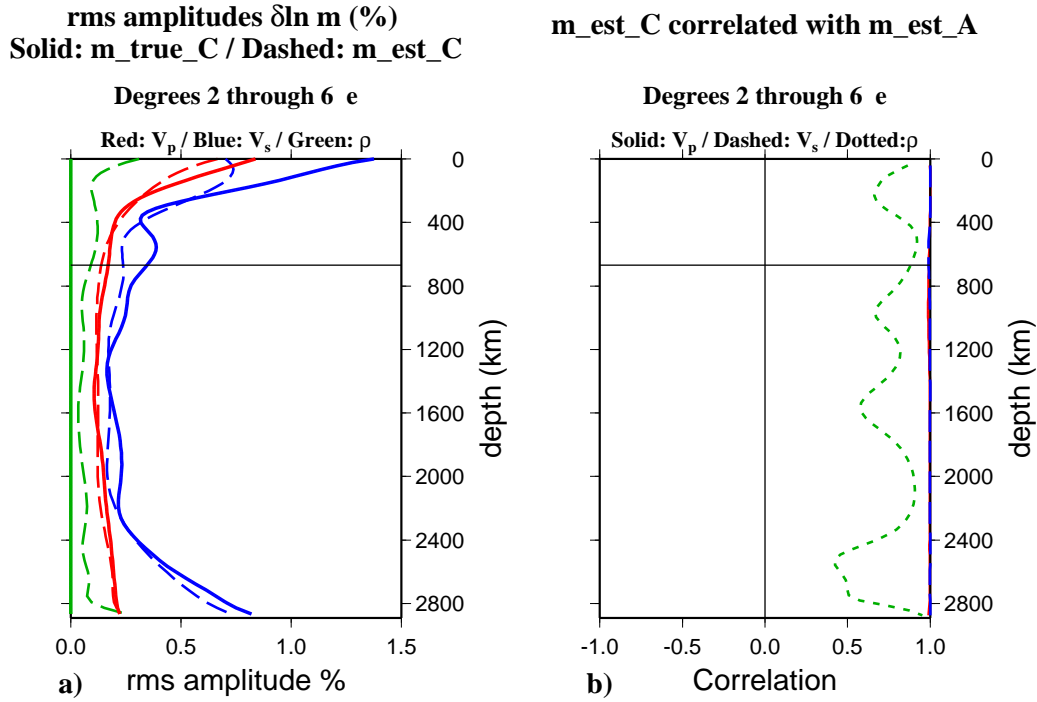


Figure 6.10: a) For Experiment C, the root mean squared amplitudes of an input model  $\mathbf{m}_{true}$  in solid lines, and output model  $\mathbf{m}_{est}$  from a resolution matrix test, in dashed lines. The blue lines are  $\delta V_s$ , the red lines are  $\delta V_p$ , and the green lines are  $\delta \rho$  rms amplitudes. See Table ?? for description of input models. The input  $\delta \rho_{true} = 0$  (solid green line). The retrieved  $\delta \rho_{est}$  has rms amplitudes  $> 0$ . b) The retrieved model  $\mathbf{m}_{est}^C$  correlated with the retrieved model  $\mathbf{m}_{est}^A$ . The blue dashed line is the correlation of  $\delta V_s$  between the two models, red solid line is for  $\delta V_p$ , and the green dotted line is for  $\delta \rho$ .

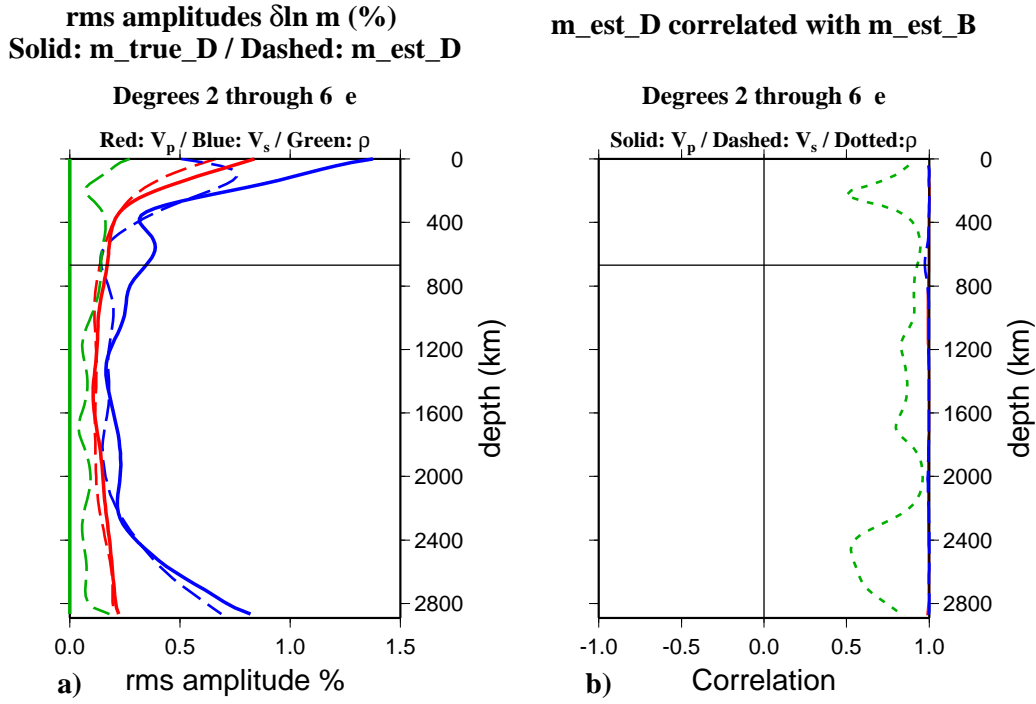


Figure 6.11: For Experiment D, the root mean squared amplitudes of an input model  $\mathbf{m}_{true}$  in solid lines, and output model  $\mathbf{m}_{est}$  from a resolution matrix test, in dashed lines. The blue lines are  $\delta V_s$ , the red lines are  $\delta V_p$ , and the green lines are  $\delta \rho$  rms amplitudes. See Table ?? for description of input models. The input  $\delta \rho_{true} = 0$  (solid green line). The retrieved  $\delta \rho_{est}$  has rms amplitudes  $> 0$ . b) The retrieved model  $\mathbf{m}_{est}^D$  correlated with the retrieved model  $\mathbf{m}_{est}^B$ . The blue dashed line is the correlation of  $\delta V_s$  between the two models, red solid line is for  $\delta V_p$ , and the green dotted line is for  $\delta \rho$ .

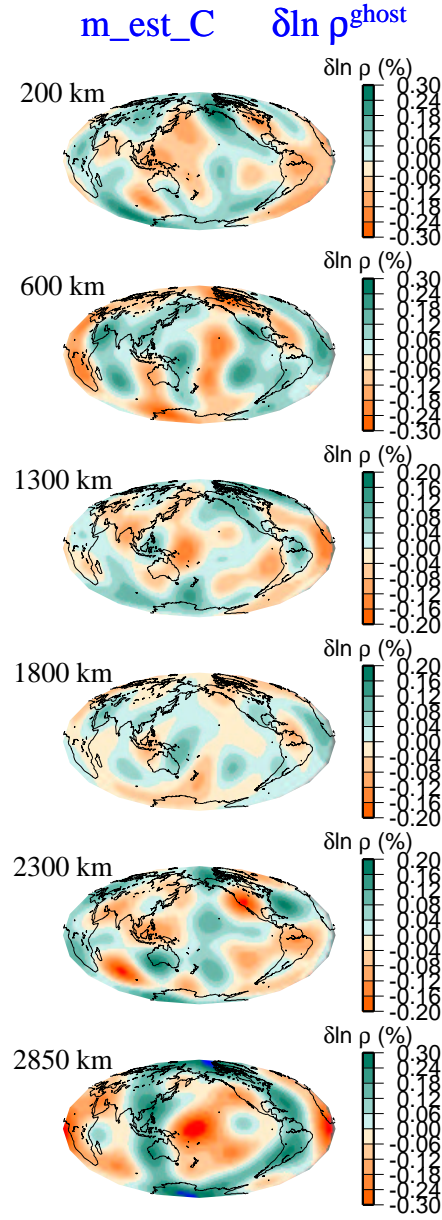


Figure 6.12: Even degrees 2, 4, and 6 of retrieved model  $\delta \rho_{est}^C$  are shown for six depths in the mantle. We name  $\delta \rho_{est}^C$  a 'ghost' density model because the input model is  $m_{true} = [P16B30, SAW12D, 0]$  for  $s_{max} = 6, p_{max} = 7$ .

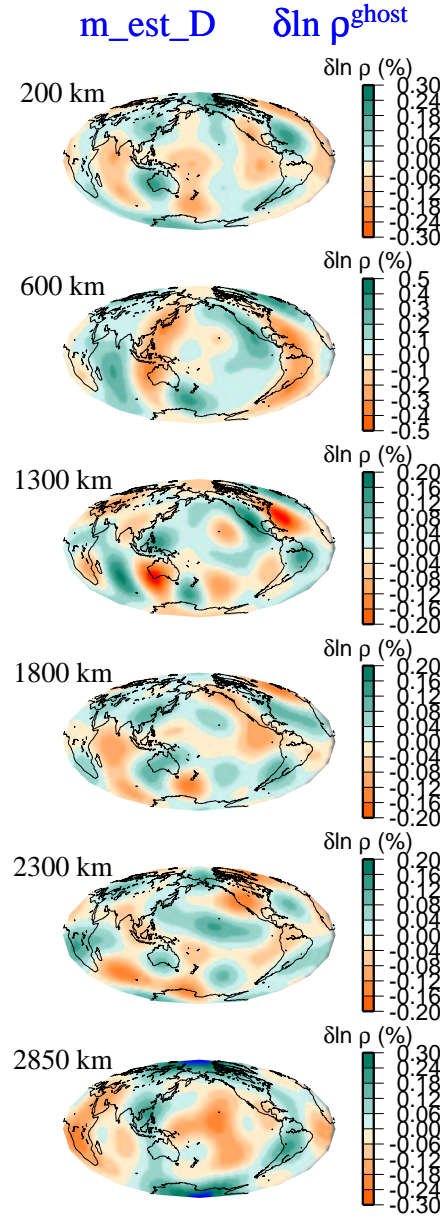


Figure 6.13: Even degrees 2, 4, and 6 of retrieved model  $\delta \rho_{est}^D$  are shown for six depths in the mantle. We name  $\delta \rho_{est}^D$  a 'ghost' density model because the input model is  $m_{true} = [P16B30, SAW12D, 0]$  for  $s_{max} = 6, p_{max} = 10$ .

density model (Figures ?? and ??). The maps of 'ghost' density patterns for degrees 2, 4, and 6 are shown in Figures ?? and ?? for Experiments C and D. Only the even degrees are displayed to compare directly with published density models, even though the odd degree model parameters are not very large and do not have much of an impact on the displayed images. High density regions corresponding to regions of slab subduction exist at many depths. In fact, the patterns of  $\delta\rho_{est}^C$  and  $\delta\rho_{est}^C$  are similar to density models obtained from inversions of spectral data, which we call R\_NMSPEC (Figure ??)(*Kuo et al., 1998; Kuo and Romanowicz, 1999a, 1999b*). The model R\_NMSPEC is spatially parameterized to  $s_{max} = 6$  and  $p_{max} = 7$ , and no *a priori* assumptions are imposed for the inversion of observed spectral data. The correspondence between Figures ?? and ?? shows that if P16B30 and SAW12D are representative of the seismic velocity perturbations in the real Earth, the artifact density models puts into question the confidence we have in the density models obtained from the inversions of the normal mode spectra.

If we use SH12WM13 (*Su and Dziewonski, 1994*), as a starting model for  $\delta V_S$ , (experiments E-F), the ghost density model retrieved is somewhat different. In Experiment F, the resulting ghost density model for a  $s_{max} = 6, p_{max} = 10$  parameterization yields patterns (Figure ??) which are strongly reminiscent of the published density model SPRD6 of *Ishii and Tromp, 1999*, particularly the high density feature in the Pacific basin and over Africa at 2800 km. There

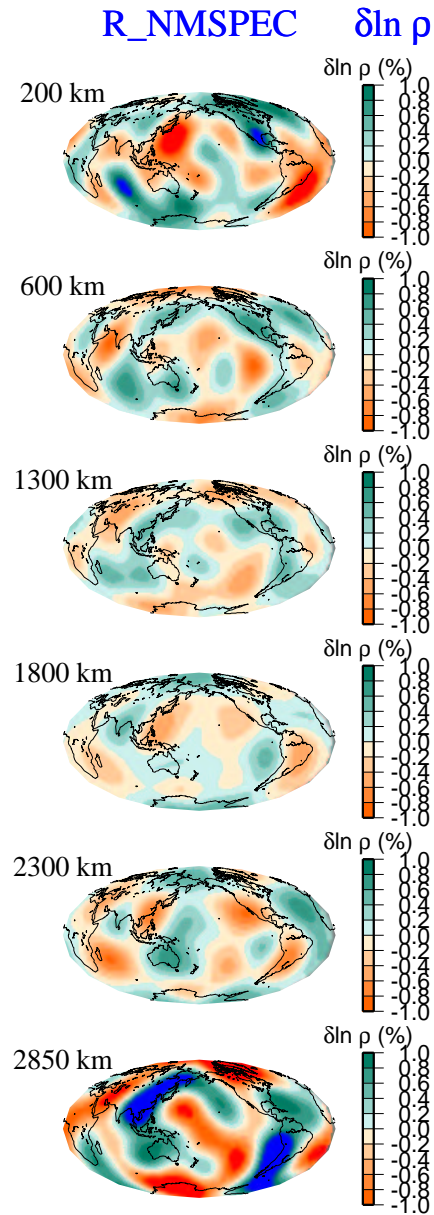


Figure 6.14: The even degrees 2, 4, and 6 of a density model (*Kuo and Romanowicz, 1998, 1999*) retrieved from normal mode spectra is shown here for six mantle depths, for comparison with Figures ?? and ??.

are, however, lateral shifts in the distribution of the patterns between Figure ?? and Figure 3 in *Ishii and Tromp, 1999*. In Figure ??, the density patterns from SPRD6 *Ishii and Tromp, 1999* and  $\delta\rho_{est}^F$  are directly compared for six depths in the mantle. The resemblance is striking, although the amplitudes of  $\delta\rho_{est}^F$  are much smaller in the lower mantle. However, amplitudes retrieved from inversions are dependent on the choice of damping parameter values. There is not so much resemblance to the SPRD6 density model for the  $p_{max} = 7$  parameterization in Experiment E (Figure ??), but high density ghost features also appear in the Pacific Basin at 2800 km. The source of this contamination could be attributed to  $\delta V_P$  (Figures ?? and ??, if one assumes that  $V_p$  is highly correlated with  $V_s$ ).

While regularization schemes used in resolution tests are not directly applicable to the inversion of observed data (*Resovsky and Ritzwoller, 1999*) due to the effects of noise, the damping scheme which we use is quite simplistic in  $\mathbf{C}_m^{-1}$  and is imposed in the absence of noise. Despite this simplistic damping scheme, we can retrieve ghost density models which mimic density models inverted from data. Tests of model robustness by considering random noise in the data (*Ishii and Tromp, 1999*) can still stably produce density models given by Figure ?? since the contamination in the density model parameter space is due to coherent rather than random noise.

Of course, the contamination effect is more important for a low level of signal



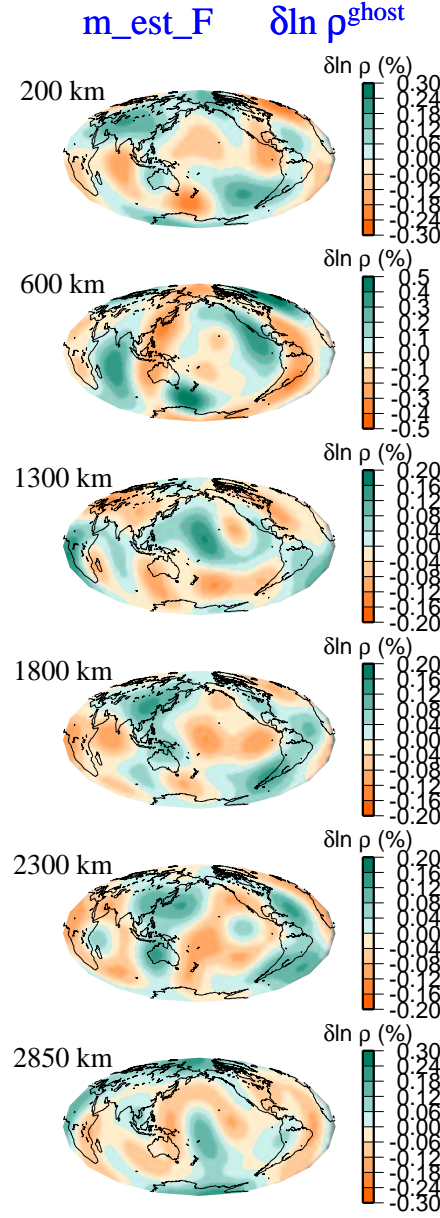


Figure 6.15: Even degrees 2, 4, and 6 of retrieved model  $\delta \rho_{est}^F$  are shown for six depths in the mantle. We name  $\delta \rho_{est}^F$  a 'ghost' density model because the input model is  $m_{true} = [P16B30, SH12WM13, 0]$  for  $s_{max} = 6, p_{max} = 10$ .

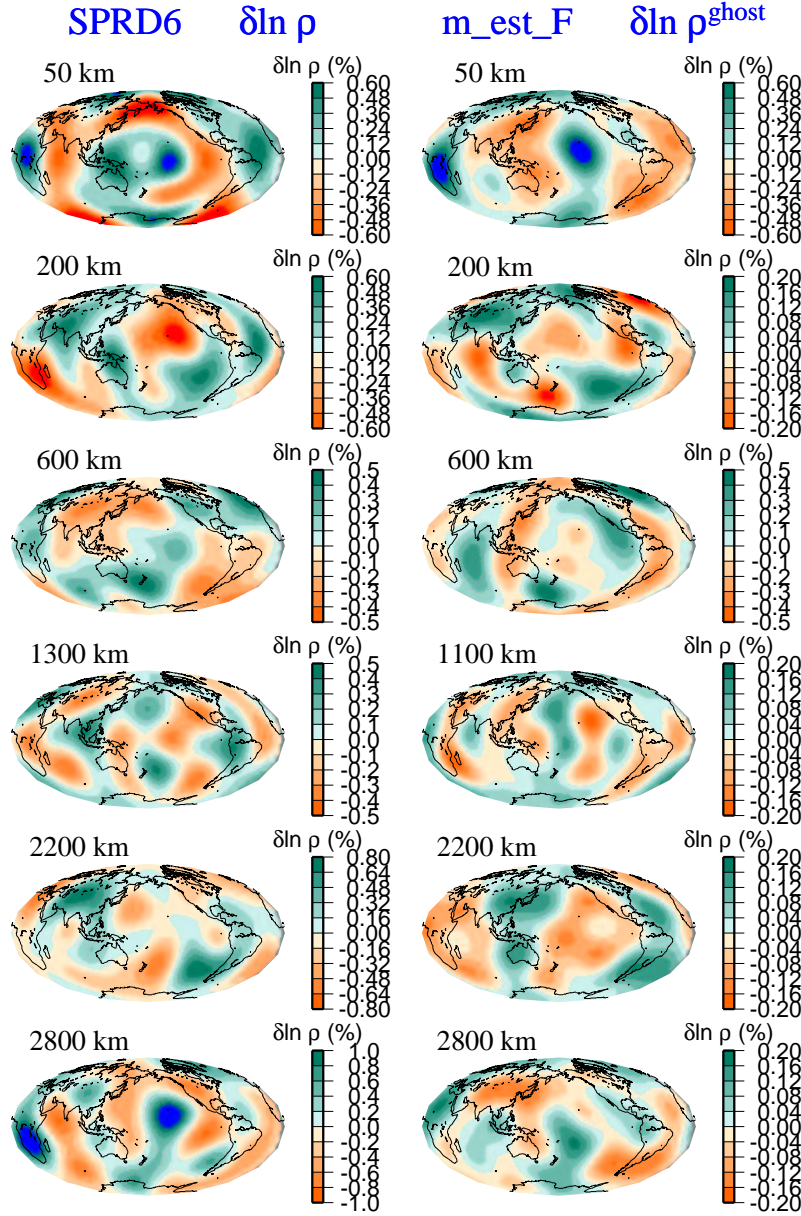


Figure 6.16: Comparison of the density model of SPRD6 (*Ishii and Tromp, 1999*), left column, and ghost density model  $\delta \rho_{est}^F$ , right column, at six mantle depths, for even degrees 2, 4, and 6. SPRD6 is inverted from normal mode splitting coefficients.

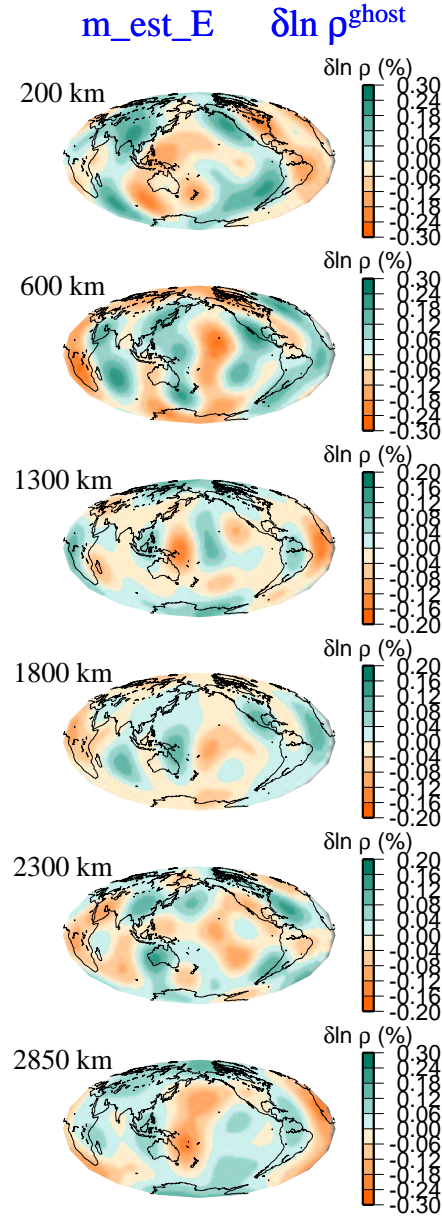


Figure 6.17: Even degrees 2, 4, and 6 of retrieved model  $\delta \rho_{est}^E$  are shown for six depths in the mantle. We name  $\delta \rho_{est}^E$  a 'ghost' density model because the input model is  $m_{true} = [P16B30, SH12WM13, 0]$  for  $s_{max} = 6, p_{max} = 7$ .

in  $\delta\rho_{true}$ , and for larger levels of signal in  $\rho$ , it may still be possible to retrieve some information, especially by applying an appropriate damping scheme. However, the confidence in the resulting model will always be marginal, and will have to be supplemented by independent information, such as constraints provided by fits to the observed geoid.

### 6.2.3 Tests with $\rho$ input models of different amplitudes

Experiments A-F have demonstrated that density perturbation amplitudes which are about 25% of  $\delta V_s$  cannot be retrieved with confidence. The estimated models of density in Experiments A and B, in which a mock input density model is used, are highly correlated with the estimated densities of Experiments C and D, for which no input density was used. The high correlation demonstrates that contamination from seismic velocity signal swamps out the density signal in Experiments A and B. The level of density perturbation signal in the Earth which can be detected needs to be investigated. To do so we refer to experiments A,B and H,I (Table ??) in which we respectively consider two input density models which differ only by an amplitude scaling factor. The mock density perturbations in model R50 have twice the amplitudes as in model R25.

At the level of density signal in R50, Figure ?? shows that  $\delta\rho_{true}^H$  is correlated with  $\delta\rho_{est}^H$  much better than when the density signal is that of R25 (Figure ??). Overall, this is true for the correlation of  $\delta\rho_{true}^I$  and  $\delta\rho_{est}^I$  in comparison with the

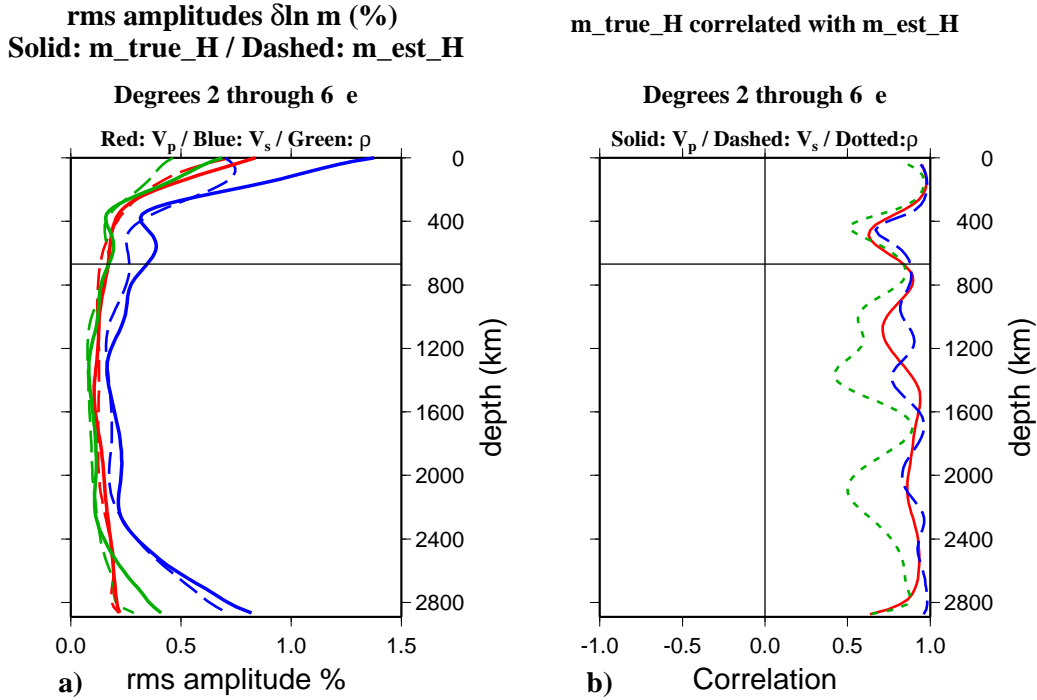


Figure 6.18: For Experiment H, the same as in Figure ??

correlation of  $\delta \rho_{true}^B$  and  $\delta \rho_{est}^B$  (Figures ?? and ??), but for this radial parameterization,  $p_{max} = 10$ , the density correlation in Experiment I is poor below the transition zones down to 1200 km depth. This indicates that Experiment I is overparameterized, leading to deficiencies in resolution.

Next, we correlate the  $\delta \rho_{est}$ 's in Experiments H and I with ghost density estimates from Experiments C and D. Correlation of  $\delta \rho_{est}^H$  with the ghost density model  $\delta \rho_{est}^C$  is decreased in comparison with Figure ??, demonstrated by the left plot in Figure ?. However,  $\delta \rho_{est}^I$  correlates above 50% with the ghost density model  $\delta \rho_{est}^D$  in over three-fourths of the mantle, shown in right plot of Figure

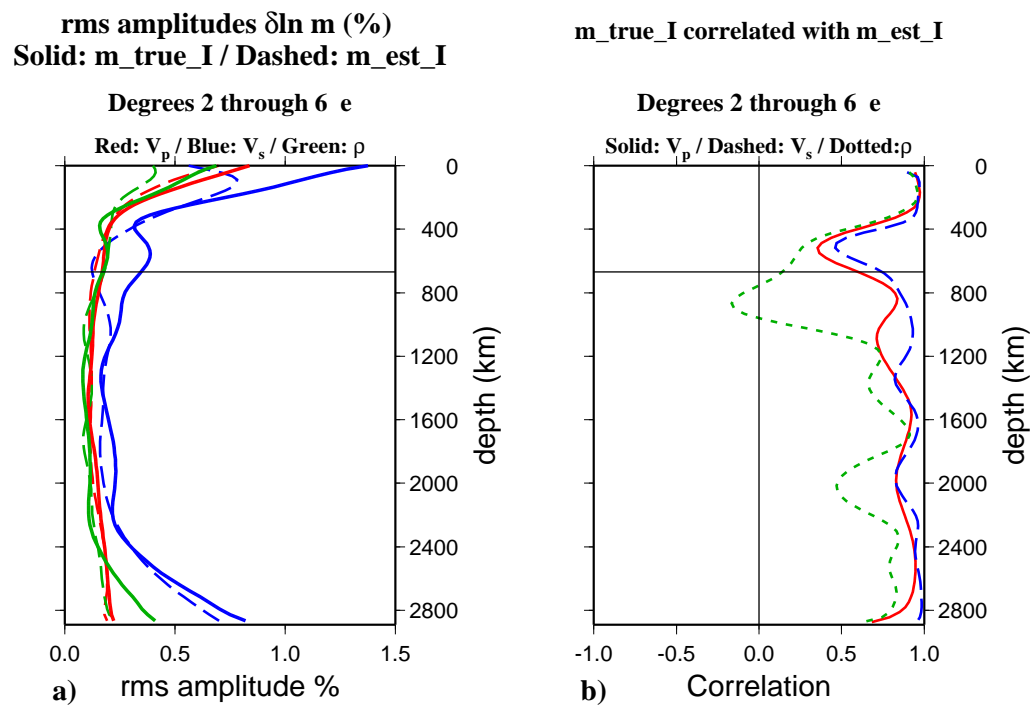


Figure 6.19: For Experiment I, the same as in Figure ??

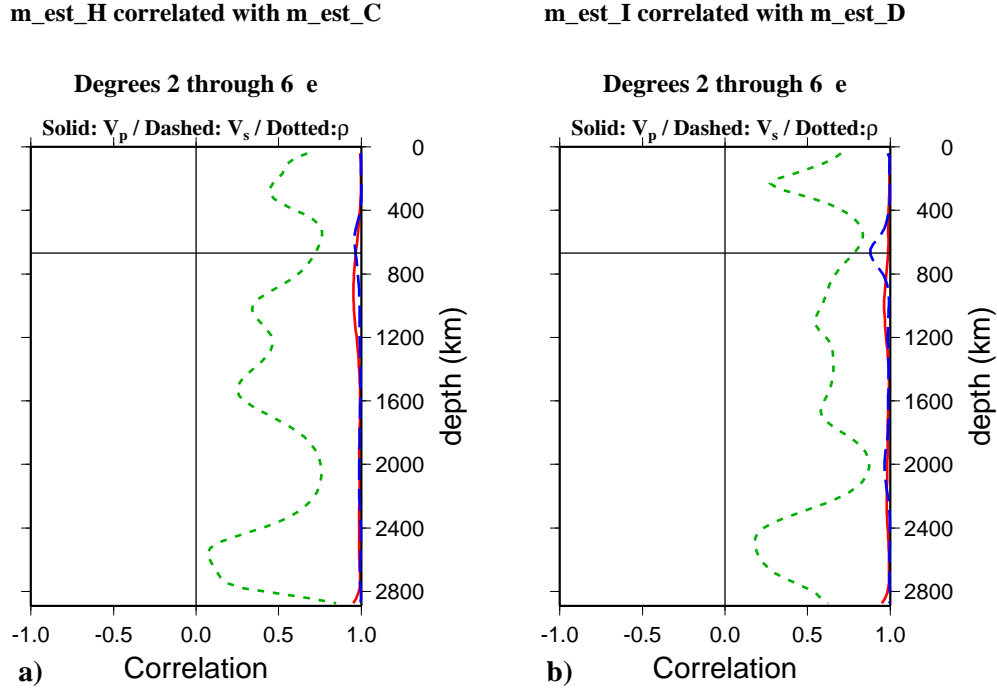


Figure 6.20: Correlations of estimated models for which input density is zero (Experiments C and D) with estimated models for which input density is a mock model R50 (Experiments H and I). a) Correlation between  $\mathbf{m}_{est}^C$  and  $\mathbf{m}_{est}^H$ ,  $s_{max} = 6, p_{max} = 7$ , and b) correlation between  $\mathbf{m}_{est}^D$  and  $\mathbf{m}_{est}^I$ ,  $s_{max} = 6, p_{max} = 10$ .

??.

These tests demonstrate that for the 44 spheroidal modes which we use in our data set, the radial parameterization  $p_{max} = 7$  can begin to retrieve density patterns over the contamination signal if the amplitudes of density perturbations are about half of  $V_s$  perturbation amplitudes, that is, a little less than 1% for  $\delta\rho/\rho$  in the shallow mantle. Models parameterized to higher orders, such as  $p_{max} = 10$ , suffer in resolving power if not sufficiently damped.

Although the density models obtained from normal mode data (*Ishii and*

*Tromp, 1999; Kuo and Romanowicz, 1999*) currently resemble the ghost density patterns from Experiments C-F, we do not suggest that the Earth's density perturbations are not resolvable. The expected amplitudes of density perturbations due to slabs at high pressures and temperatures (*Panero and Jeanloz, in preparation*) is 1-2%. Therefore, the density signal may be at the limit of being resolvable. If there is real signal in the density models derived from data, it may very likely be overwhelmed by contamination. The plots on the left in Figures ?? and ?? show that the contaminant density amplitudes can be commensurate with the amplitudes in R50 (left plot in Figure ??). Inversions with real data can yield density amplitudes greater than those in R50, but before assuming that the amplitudes are an indication of large signal, one must ensure that the amplitudes are not due to coherent errors from contamination producing such an amplified signal. It will be necessary to find appropriate damping parameters to reduce the effect of the covariant elements between physical model parameters in the resolution matrix.

### 6.3 Tests with synthetic seismograms

So far, we have only considered simple tests, to illustrate the sensitivity of the retrieved density models to assumptions on damping, resulting from the structure of the resolution matrix. However, our particular inversion scheme is non-linear, and therefore involves several iterations, whose results may not



be completely represented by the resolution matrix corresponding to the first iteration only. In what follows, we present more complete tests involving the computation of synthetic seismograms and their iterative inversion, more accurately simulating the inversion process corresponding to real spectral data.

Specifically, we are interested in the contaminant signal in density resulting from our iterative inversion scheme. The spatial parameterization and input models of Experiments E and F are revisited in Experiments J and K (Table ??) whereby the estimated models  $\mathbf{m}_{est}^J$  and  $\mathbf{m}_{est}^K$  are now obtained from inversions of synthetic seismograms computed from input models  $\mathbf{m}_{true}^J = \mathbf{m}_{true}^K$ .  $\mathbf{m}_{true}^J$  and  $\mathbf{m}_{true}^K$  are composed of models P16B30 for  $\delta V_p$  and SH12WM13 for  $\delta V_s$ , and there are no density perturbations. Aspherical structure up to harmonic degree 12 and radial order 13 are included in the computation of synthetic seismograms. We start the inversions from PREM (*Anderson and Dziewonski, 1981*), and damp the second radial derivative ( $\eta_3$  in equation(4.8)) to ensure radial smoothness.  $\eta_3$  for  $V_p$  was required to be twice as strong as for either  $V_s$  or  $\rho$  to produce a radially smooth model. After 4 iterations, the models  $\mathbf{m}_{est}^J$  and  $\mathbf{m}_{est}^K$  converge to give 99.6% and 99.5% fits to the synthetic data respectively.

The two models  $\mathbf{m}_{est}^J$  and  $\mathbf{m}_{est}^K$  are extremely similar and we believe that this is due to the choice of damping to smooth the radial models. At present, the radial damping  $\eta_3$  applied for  $V_p$  is insufficient and stronger damping should be applied. The root-mean-squared profile for  $\delta V_{p\ est}$  shows a large augmented

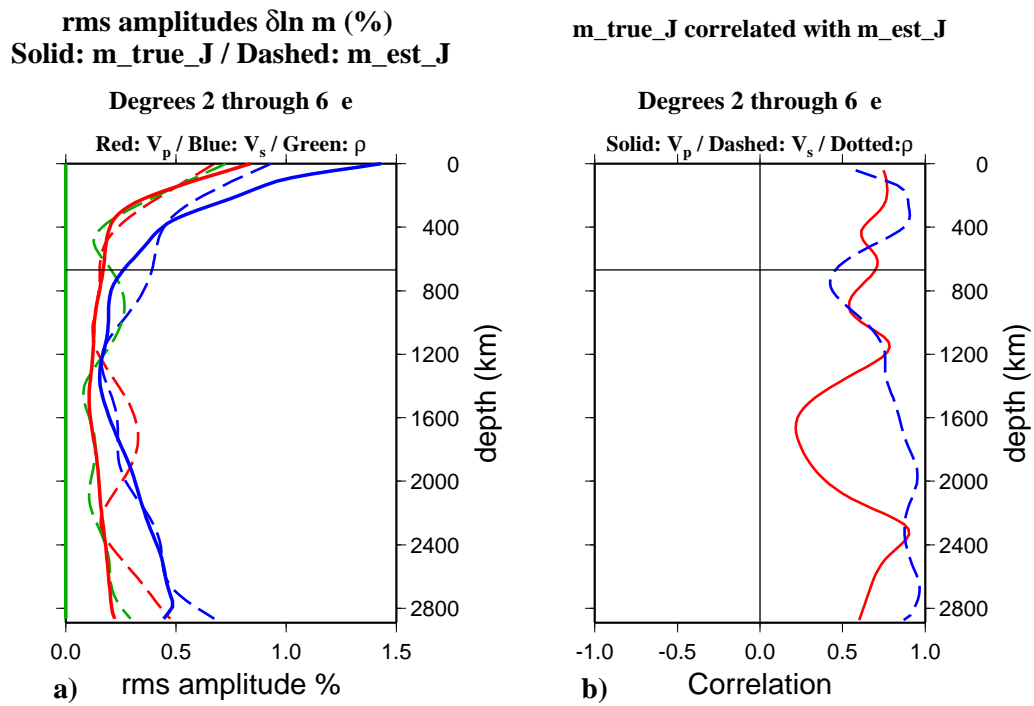


Figure 6.21: For Experiment J, the same as in Figure ??

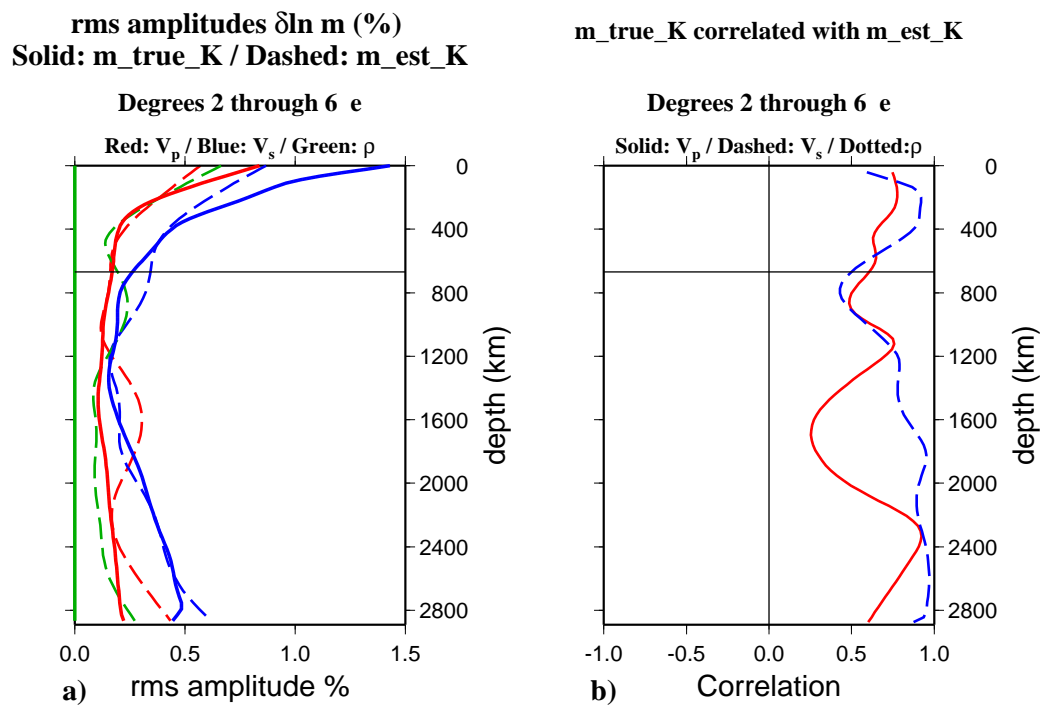


Figure 6.22: For Experiment K, the same as in Figure ??

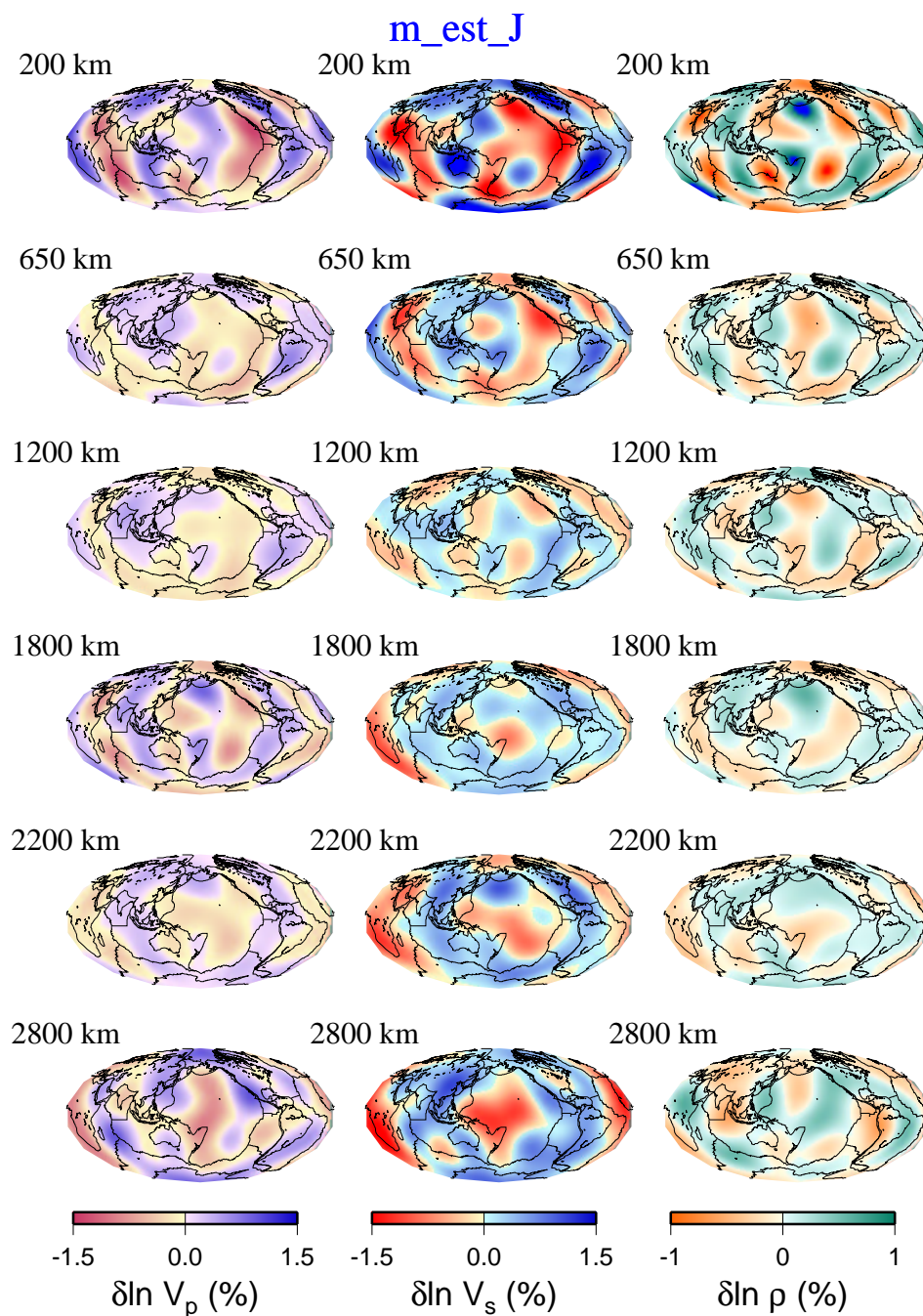


Figure 6.23: From resolution tests inverting synthetic seismograms, the output model of perturbations in  $V_p$ , left column,  $V_s$ , middle column, and  $\rho$ , right column, for an input model  $\mathbf{m}_{true}^J$ . The spatial parameterization for this estimated model is  $s_{max} = 6, p_{max} = 7$ , whereas  $s_{max} = 12, p_{max} = 13$  for the input model were used in the synthetic seismogram computations.

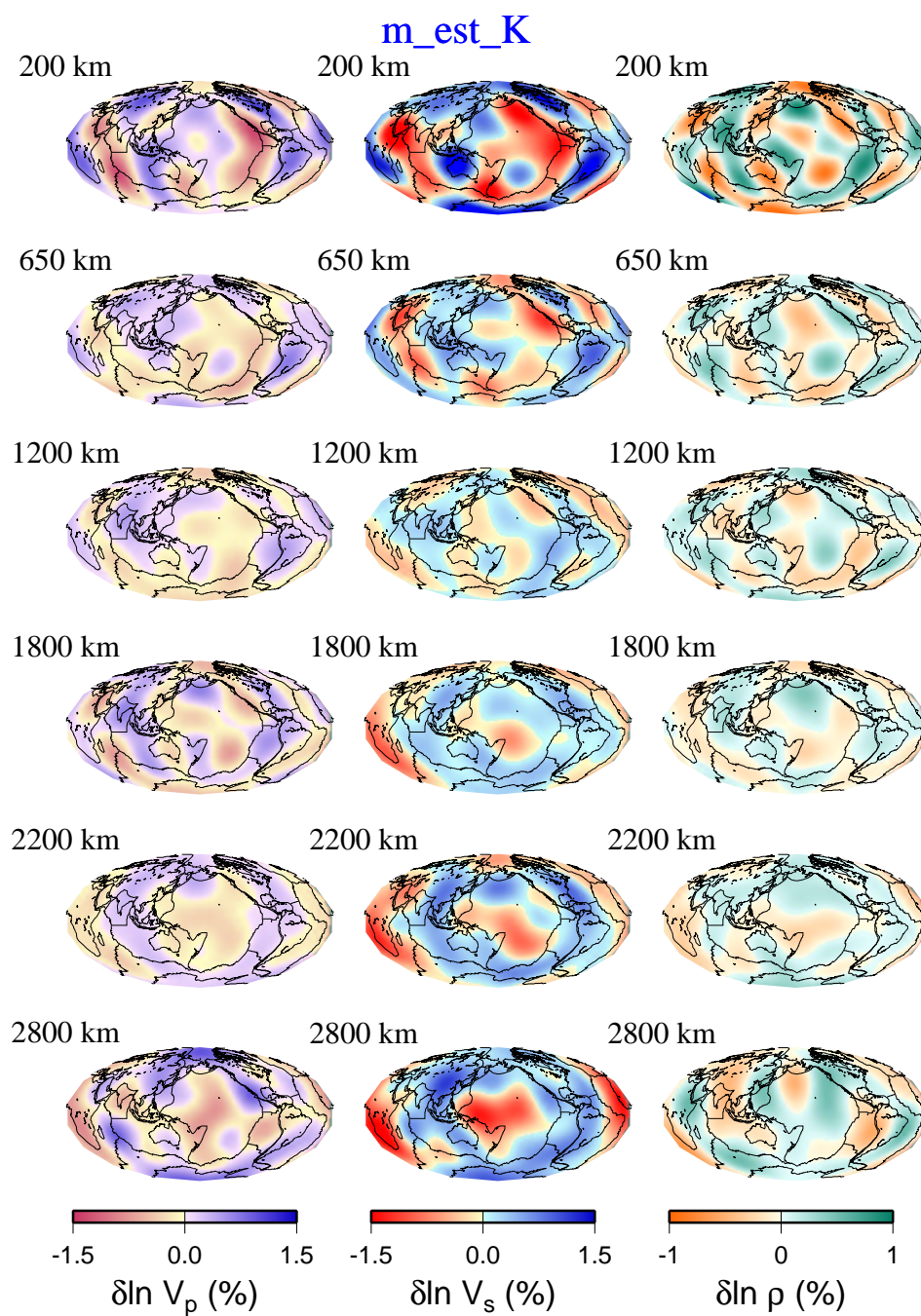


Figure 6.24: The same as in Figure ??, for an input model  $\mathbf{m}_{true}^K(=\mathbf{m}_{true}^J)$ . The spatial parameterization for this estimated model is  $s_{max} = 6, p_{max} = 10$ , whereas  $s_{max} = 12, p_{max} = 13$  for the input model were used in the synthetic seismogram computations.

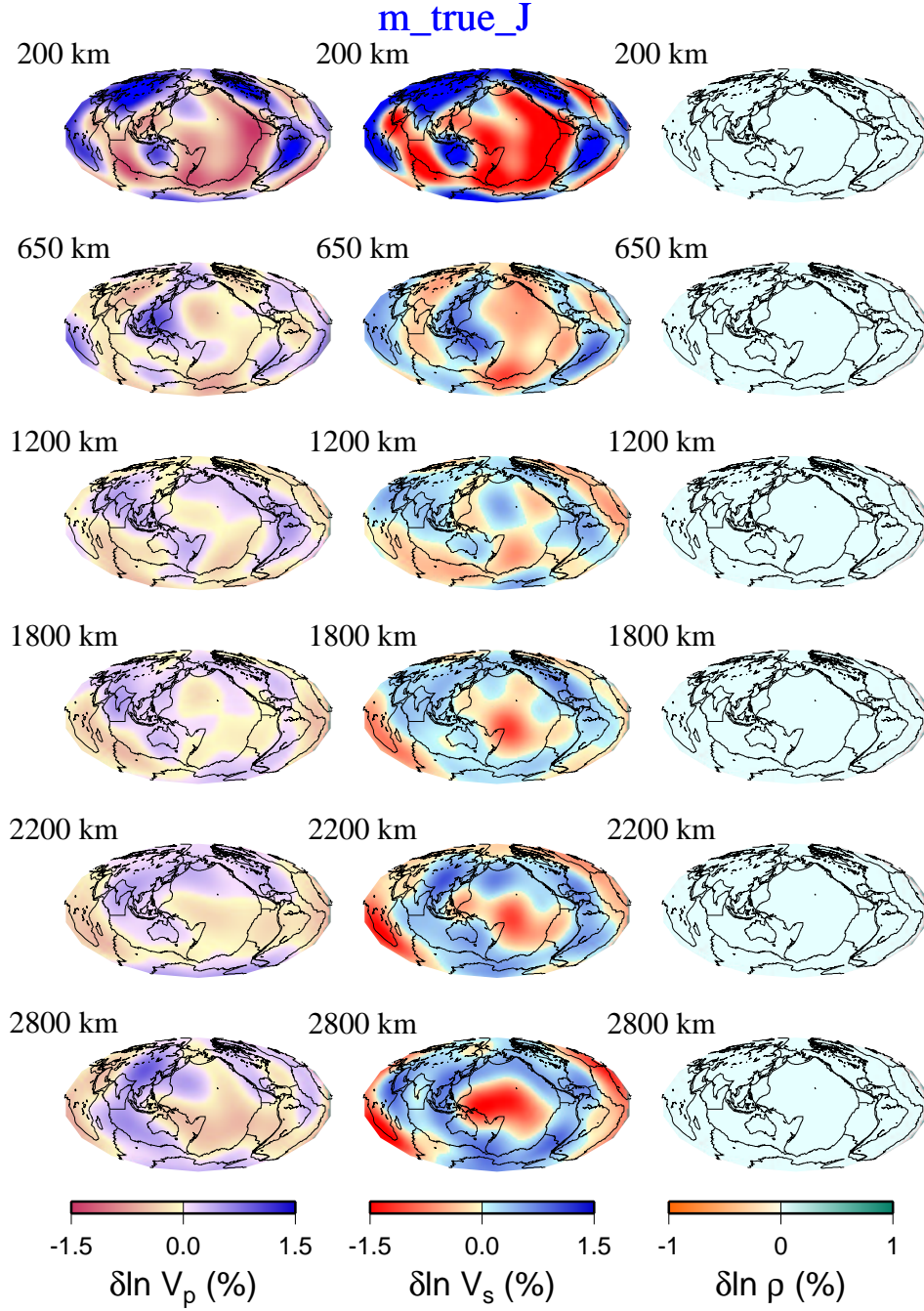


Figure 6.25: For Experiments J and K (also E and F), the input model  $\mathbf{m}_{true} = [\delta V_p, \delta V_s, 0]$  where  $\delta V_p$ =P16B30 (*Masters and Laske, personal communication*), and  $\delta V_s$ =SH12WM13 (*Su and Dziewonski, 1994*). There are no density perturbations in  $\mathbf{m}_{true}$ .

bump in the lower mantle which corresponds to a decreased correlation between the input and output  $V_p$  models at the same depths (Figures ?? and ??).

The patterns of  $\mathbf{m}_{est}^J$  and  $\mathbf{m}_{est}^K$  are shown in Figures ?? and ?? for degrees 1 through 6. The input model for  $\mathbf{m}_{true}^J = \mathbf{m}_{true}^K$  is shown in Figure ?? for comparison. Assessment of our inversions with real data, (Figure 5.12) can be made by comparing  $\mathbf{m}_{est}^J$  with  $\mathbf{m}_{true}^J$ . In particular, we can compare the density model obtained from normal mode spectral data (third column in Figure 5.12), with the ghost density patterns in the third columns in Figures ?? and ?? and find that most of the high density features from our density models can be explained by features in the ghost density model.

## 6.4 Discussion and Conclusions

Current methods of retrieving three-dimensional mantle density structure from normal mode spectra (*Kuo and Romanowicz, 1999b*) and normal mode splitting coefficients (*Ishii and Tromp, 1999*) do not appear to yield reliable density models. The mantle density models are affected by the contamination of  $V_P$  and  $V_S$  structure into the density model space.

*Resovsky and Ritzwoller, 1999* have documented the instability of  $\rho$  models derived from normal mode splitting coefficients when using a sweep of *a priori* constraints. They have shown that it is not possible to determine correlation and/or decorrelation of  $\delta\rho$  with seismic velocity as a function of depth. Our work



supports their conclusions that current methods and data sets are not sufficient to uniquely determine the density structure of the Earth. We have shown that it is possible to retrieve models of  $\rho$  perturbations purely due to contamination from  $V_S$  and  $V_P$  structure, and that these ghost  $\rho$  models are consistent in pattern and amplitude with published  $\rho$  models inverted from splitting coefficients (*Ishii and Tromp, 1999*), and with  $\rho$  models which we determine from normal model spectral data. When using a spatial parameterization of  $s=6$ ,  $w=7$  for Earth structure, the ghost density model exhibits high density features surrounding the Pacific, much like the features which we have found in our  $\rho$  models inverted from data. The density model SPRD6 of *Ishii and Tromp, 1999*, retrieved from linear inversions of normal mode splitting coefficients, is different from density models from our non-linear inversions of normal mode spectral data. We have found that resolution tests involving linear products of resolution matrices with input Earth models devoid of a density perturbations ( $\mathbf{m}_{true} = [V_p, V_s, 0]$ ) produce ghost density models which closely resemble the density structure of SPRD6. From our performance of non-linear inversions of synthetic spectra computed from the same input model  $\mathbf{m}_{true} = [V_p, V_s, 0]$ , a ghost density pattern is produced which resembles density models estimated from normal mode spectral data (*Kuo and Romanowicz, 1999*).

Since  $\delta\rho$  might be correlated with  $\delta V_S$  throughout parts of the mantle, this signal may be buried in the noise. Based on our tests of contamination, how-



ever, no conclusions may be drawn on the correlation of  $\delta\rho$  with  $\delta V_S$ . Damping the covariant elements between physical model parameters may aid in reducing contamination in  $\delta\rho$  from the seismic velocities. Perhaps resolution of density feature size should be addressed. If normal modes have little sensitivity to density perturbations to harmonic degree 6, then we propose to invert for  $V_P$ ,  $V_S$ , and  $\rho$  perturbations in a spatial parameterization scheme for which we may solve for  $\rho$  parameterized to smaller degrees  $s$  than for  $V_P$  and  $V_S$ . The cumulative contamination of covariant elements in the resolution matrix for spatial parameterizations must be addressed.

## Chapter 7

### Outlook

Based on the astrophysical and seismological methods analysed in this dissertation research, we have found that reliable measurements of the Earth's deep interior three-dimensional density structure continue to elude the geophysics community. Most recent theoretical calculations of very high energy neutrino data count rates which would be measured at current detectors are prohibitively low (*Douglas Lowder, personal communication*), and would require a couple of decades' worth of data to distinguish features such as the core from the mantle. We have shown that the current methods used in normal mode seismology, which takes advantage of split spectra, do not produce credible density models. A combination of modes to include in the data set which could amplify the density kernel sensitivity may be a useful strategy in the future, although it may be impossible to decrease the seismic velocity kernel sensitivities. It would be imperative to inspect resolution matrices with diagonal elements normalized by covariant elements to understand thoroughly the tradeoffs between model

parameters. Perhaps with future instrumentation in which the noise floor due to barometric pressure is reduced, even cleaner signals may allow us to extract perturbations in density from normal model spectral splitting.

The common assumption that density perturbations scale with velocity perturbations is reasonable at least down to the mid-lower mantle. This assumption can be used as an additional constraint to solve, for a scaling relationship as a function of depth, between density and shear velocity. It is conceivable that this approach could offer some information on the three-dimensional density structure of the Earth's interior.

## References

- Askar'yan, G. A., Investigation of the Earth by means of neutrinos, Neutrino geology, *Sov. Phys. Usp.* , **27**, 896-900, 1984.
- Barwick, S. et al., AMANDA South Pole neutrino detector, in: 26th International Conference on High Energy Physics , American Institute of Physics Conf. Proc. No. 272, pp. 1250-1253, 1992.
- Bassani, L. and A.J. Dean, Absorption of  $\gamma$ -rays in active galaxies as a test for the jet hypothesis, *Nature*, **294**, 332-333, 1981.
- Becker-Szendy, R.A., Study of Upward-going muons with the IMB detector, University of Hawaii at Manoa High Energy Physics Report UH-511-729-91, Honolulu, Hawaii, 1991 (Ph.D. Thesis).
- Belolaptikov, I.A. et al., The lake Baikal underwater telescope NT-36: first months of operation, in: Third Int'l Workshop on Theoretical and Phenomenological Aspects of Underground Physics, *Nucl. Phys. B Proc. Suppl.* , **35**, pp. 290-293, 1994.

- Berezinski'i, V.S., A.Z. Gazizov, G.T. Zatsepin, and I.L. Rozental, The passage of high energy neutrinos through the Earth and the possibility of detecting them by means of extensive air showers, *Sov. J. Nucl. Phys.* , **43**, 406-413, 1986.
- Berezinsky, V.S. and J.G. Learned, Upper bounds on Diffuse High Energy Neutrino Fluxes, in: High Energy Neutrino Astrophysics, V.J. Stenger, J.G. Learned, S. Pakvasa and X. Tata, eds., pp. 43-57, World Scientific, Singapore, 1992.
- Bohn, T., Time-Lapse Analysis of Core-Sensitive Free Oscillations, Master's thesis, University of California, Berkeley, 1994.
- Bolt, B.A. and R. Uhrhammer, Resolution techniques for density and heterogeneity in the Earth, *Geophys. J. R. Astr. Soc.*, **42**, 419-35, 1975.
- Borisov, A. B., B.A. Dolgoshein, and A.N. Kalinovski'i, direct method of determining the differential distribution of the density of the Earth by means of high-energy neutrino scattering, *Sov. J. Nucl. Phys.* , **44**, 442-447, 1986.
- Clévéde, E. and P. Lognonné, Frechet derivatives of coupled seismograms with respect to an anelastic rotating Earth. *Geophys. J. Int.*, **124**, 456-82, 1996.
- Cronin, J.W., High Energy Astrophysics, in: 1989 Int'l Symposium on Lepton and Photon Interactions at High Energies, M. Riordan, ed., pp. 403-419,

World Scientific, Singapore, 1990.

Dahlen, F.A., The effect of data windows on the estimation of free oscillation parameters, *Geophys. J. R. Astr. Soc.*, **69**, 537-49, 1982.

Dahlen, F.A., Reply, *J. Geophys. Res.*, **81**, 491, 1976.

Dahlen, F.A., The normal modes of a rotating, elliptical earth. II. near-resonance multiplet coupling, *Geophys. J. R. Astr. Soc.*, **18**, 397-436, 1969.

Dahlen, F.A., The normal modes of a rotating, elliptical earth, *Geophys. J. R. Astr. Soc.*, **16**, 329-367, 1968.

De Rújula, A., S. L. Glashow, R. R. Wilson and G. Charpak, Neutrino Exploration of the Earth, *Phys. Rep.*, **99**, 341-396, 1983.

Durek, J. and B. Romanowicz, Inner core anisotropy inferred by direct inversion of normal mode spectra, In press, *Geophys. J. Int.*, 1999.

Dziewonski, A.M., X.-F. Liu, and W.-J. Su, in *Earth's Deep Interior: the Doornbos memorial volume*, D. J. Crossley, ed., pp. 11-50, Gordon and Breach Science, Newark, N.J., 1997.

Dziewonski, A.M., G. Ekstrom, and M.P. Salganik, Centroid-moment tensor solutions for April-June 1994. *Physics of the Earth and Planetary Interiors*, **88**, 69-78, 1995.

Dziewonski, A.M. and D.L Anderson, Preliminary reference Earth model, *Phys. Earth Planet. Inter.*, **25**, 297-356, 1981.

Dziewonski, A.M. and F. Gilbert, Solidity of the inner core of the Earth inferred

- from normal mode observations, *Nature*, **234**, 465-6, 1971.
- Edmonds, A.R., *Angular Momentum in Quantum Mechanics*, Princeton University Press, Princeton, N.J., 1960.
- Fichtel, C.E. et al., The first Energetic Gamma-Ray Experiment Telescope (EGRET) Source Catalog, *Astrophys. J. Suppl. Ser.* , **94**, 551-581, 1994.
- Flatté, S.M., R.J. Decoster, M.L. Stevenson, W.T. Toner and T.F. Zipf, Zenith-angle Distribution of Atmospheric Muons above 1 TeV, *Phys. Lett.* , **35B**, 345-350, 1971.
- Frichter, G.M., D.W. McKay and J.P. Ralston, Small-X Quarks from HERA Predict the Ultra-High Energy Neutrino-Nucleon Scattering Cross Section, *Phys. Rev. Lett.*, **74**, 1508-1511, 1995.
- Giardini, D., X.-D. Li and J.H. Woodhouse, Splitting functions of long-period normal modes of the Earth, *J. Geophys. Res.*, **93**, 13716-42, 1988.
- Giardini, D., X.-D. Li, and J.H. Woodhouse, Three-dimensional structure of the Earth from splitting in free-oscillation spectra, *Nature*, **325**, 405-11, 1987.
- Gilbert, F., A. Dziewonski and J. Brune, An Informative Solution to a Seismological Inverse Problem, *Proc. Nat. Acad. Sci. USA*, **70**, 1410-1413, 1973.
- Gubbins, D., T.G. Masters and J.A. Jacobs, Thermal evolution of the Earth's

- core, *Geophys. J. R. Astr. Soc.*, **59**, 57-99, 1979.
- He, X. and J. Tromp, Normal-mode constraints on the structure of the Earth, *J. Geophys. Res.*, **101**, 20053-82, 1996.
- Ishii, M. and J. Tromp, Normal-Mode and Free-Air Gravity Constraints on Lateral Variations in Velocity and Density of Earth's Mantle *Science*, **285**, 1231-6, 1999.
- Ishii, M. and J. Tromp, Three-dimensional modeling of mantle heterogeneity and their implications for petrology, *Eos Trans. AGU*, **79**, F656, 1998.
- Ishii, M. and J. Tromp, Three-dimensional modeling of mantle heterogeneity using normal-mode splitting function coefficients, *Eos Trans. AGU*, **78**, F460, 1997.
- Jelley, J.V., Absorption of High-energy Gamma-rays within Quasars and Other Radio Sources, *Nature*, **221**, 472-475, 1966.
- Karato, S., Importance of anelasticity in the interpretation of seismic tomography, *Geophys. Research Letters*, **20**, 1623-6, 1993.
- Kennett, B.L.N., On the density distribution within the Earth. *Geophys. J. Int.*, **132**, 374-82, 1998.
- Kuo,C and B. Romanowicz, Three-dimensional Density Structure Obtained by Normal Mode Spectral Measurements, *Proceedings, IUGG XXII General Assembly*, A62, 1999a.
- Kuo, C. and B. Romanowicz, Density and Seismic Velocity Variations Deter-



- mined from Normal Mode Spectra, *Eos Trans., AGU*, **80**, S14, 1999b.
- Kuo, C., J. Durek and B. Romanowicz, Mantle heterogeneity inferred from normal mode spectra, *Eos, Trans. AGU*, **79**, F627, 1998.
- Kuo, C., J. Durek and B. Romanowicz, Direct inversion of normal mode spectra for mantle heterogeneity, *Eos, Trans. AGU*, **78**, F460, 1997.
- Li, X.-D. and B. Romanowicz, Global mantle shear velocity model developed using nonlinear asymptotic coupling theory. *J. Geophys. Res.*, **101**, 22245-72, 1996.
- Li, X.-D., D. Giardini, and J.H. Woodhouse, Large-scale three-dimensional even-degree structure of the Earth from splitting of long-period normal modes, *J. Geophys. Res.*, **96**, 551-77, 1991a.
- Li, X.-D., D. Giardini, and J.H. Woodhouse, The relative amplitudes of mantle heterogeneity in P velocity, S velocity and density from free-oscillation data, *Geophys. J. Int.*, **105**, 649-57, 1991b.
- Lithgow-Bertelloni, C. and M.A. Richards, The dynamics of Cenozoic and Mesozoic plate motions. *Rev. Geophys.*, **36**, 27-78, 1998.
- Lognonne, P. and B. Romanowicz, Modelling of coupled normal modes of the Earth: the spectral method. *Geophysical Journal International*, **102**, 365-95, 1990.
- Luh, P.C., Free oscillations of the laterally inhomogeneous Earth: Quasi - degenerate multiplet coupling, *Geophys. J. R. Astr. Soc.*, **32**, 187-202,

1973.

Masters, G., S. Johnson, G. Laske, and H. Bolton, A shear-velocity model of the mantle. *Philos. Trans. R. Soc. London A*, **354**, 1385-411, 1996.

Mégnin, C. and B. Romanowicz, A 3d model of shear velocity in the mantle from the inversion of body, surface and higher mode waveforms, *submitted to Geophys. J. Int.*, 1999.

Mégnin, C. and B. Romanowicz, Estimation of inner core mode splitting functions combining a genetic algorithm with a direct iterative inversion scheme, *Eos, Trans. AGU*, **76**, F355, 1995.

Menke, W., *Geophysical Data Analysis: Discrete Inverse Theory*, Academic Press, Inc, San Diego, CA, 1989.

Morelli, A., A.M. Dziewonski, Topography of the core-mantle boundary and lateral homogeneity of the liquid core, *Nature*, **325**, 678-83, 1987.

Nicolaidis, A., M. Jannane and A. Tarantola, Neutrino Tomography of the Earth, *J. Geophys. Res.*, **96**, 21811-21817, 1991.

Obayashi, M. and Y. Fukao, P and PcP travel time tomography for the core-mantle boundary, *J. Geophys. Res.*, **102**, 17825-41, 1997.

Panero W. and R. Jeanloz, Mineral phases and density of oceanic crust subducted into the Earth's lower mantle, *in preparation*, 1999.

Phinney, R.A. and R. Burridge, Representation of the elastic-gravitational excitation of a spherical earth model by generalized spherical harmonics,

- Geophys. J. R. Astr. Soc.*, **34**, 451-87, 1973.
- Quigg, C., M.H. Reno and T.P. Walker, Interactions of Ultrahigh-Energy Neutrinos, *Phys. Rev. Lett.*, **57**, 774-777, 1986.
- Resovsky, J.S. and M.H. Ritzwoller, Regularization uncertainty in density models estimated from normal mode data, *Geophys. Res. Lett.*, **26**, 2319-22, 1999a.
- Resovsky, J.S. and M.H. Ritzwoller, A degree 8 mantle shear velocity model from normal mode observations below 3 mHz, *J. Geophys. Res.*, **104**, 993-1014, 1999b.
- Resovsky, J.S. and M.H. Ritzwoller, New and refined constraints on three-dimensional Earth structure from normal modes below 3 mHz, *J. Geophys. Res.*, **103**, 783-810, 1998.
- Resovsky, J.S. and M.H. Ritzwoller, Constraining odd-degree Earth structure with coupled free-oscillations, *Geophys. Res. Lett.*, **22**, 2301-4, 1995.
- Resvanis, L.K. et al., NESTOR: A neutrino particle astrophysics underwater laboratory for the Mediterranean, in: High Energy Neutrino Astrophysics, V.J. Stenger, J.G. Learned, S. Pakvasa and X. Tata, eds., pp. 325-353, World Scientific, Singapore, 1992.
- Ritzwoller, M., G. Masters, and F. Gilbert, Constraining aspherical structure with low-degree interaction coefficients: application to uncoupled multiplets, *J. Geophys. Res.*, **93**, 6369-96, 1988.

- Ritzwoller, M., G. Masters, and F. Gilbert, Observations of anomalous splitting and their interpretation in terms of aspherical structure, *J. Geophys. Res.*, **91**, 10203-28, 1986.
- Roberts, A., The birth of high-energy neutrino astronomy: A personal history of the DUMAND project, *Rev. Mod. Phys.*, **64**, 259-312, 1992.
- Robertson, G.S. and J.H. Woodhouse, Evidence for proportionality of P and S heterogeneity in the lower mantle, *Geophys. J. Int.*, **123**, 85-116, 1995.
- Robertson, G.S. and J.H. Woodhouse, Ratio of relative S to P velocity heterogeneity in the lower mantle, *J. Geophys. Res.*, **101**, 20041-52, 1996.
- Rodgers, A., J. Wahr, Inference of core-mantle boundary topography from ISC PcP and PKP traveltimes, *Geophys. J. Int.*, **115**, 991-1011, 1993.
- Romanowicz, B., X.-D. Li, and J. Durek, Anisotropy in the inner core: could it be due to low-order convection?, *Science*, **274**, 963-6, 1996.
- Romanowicz, B., G. Roullet, and T. Kohl, The upper mantle degree two pattern: constraints from Geoscope fundamental spheroidal mode eigenfrequency and attenuation measurements, *Geophys. Res. Lett.*, **14**, 1219-22, 1987.
- Rose, M.E., *Elementary Theory of Angular Momentum*, John Wiley and Sons, Inc., New York, 1957.
- Stecker, F. W. , C. Done, M. H. Salamon and P. Sommers, High-energy neutrinos from active galactic nuclei, *Phys. Rev. Lett.* , **66**, 2697-2700, 1991.
- Erratum, *Phys. Rev. Lett.* , **69**, 2738, 1992.

- Stecker, F. W. , and M. H. Salamon, High-energy diffuse cosmic gamma-ray background radiation from blazars, *Astrophys. J. Lett.* , **410**, L71-74, 1993.
- V.J. Stenger, High Energy Neutrino Astrophysics: Potential Sources and their Underwater Detection, in: Proc. of the 2nd NESTOR International Workshop, L.K. Resvanis, ed., pp. 79-100, University of Athens, Athens, 1992.
- Stevenson, D.J., Limits on lateral density and velocity variations in the Earth's outer core, *Geophys. J. R. Astr. Soc.*, **88**, 311-319, 1987.
- Su, W.-J. and A.M. Dziewonski, Simultaneous inversion for 3-D variations in shear and bulk velocity in the mantle, *Phys. Earth Planet. Inter.*, **100**, 135-156, 1997.
- Su, W.-J., R.L. Woodward, and A.M. Dziewonski, Degree 12 model of shear velocity heterogeneity in the mantle, *J. Geophys. Res.*, **99**, 6945-80, 1994.
- Tarantola, A. and B. Valette, Generalized nonlinear inverse problems solved using the least squares criterion, *Rev. Geophys.*, **20**, 219-32, 1982.
- Tsarev, V. A., and V. A. Chechin, "Long-distance" neutrinos. Physical bases and geophysical applications, *Sov. J. Part. Nucl.*, **17**, 167-185, 1986.
- Tromp, J., Normal-mode splitting due to inner-core anisotropy. *Geophys. J. Int.*, **121**, 963-8, 1995.

- Van Der Hilst, R.D., S. Widiyantoro, and E.R. Engdahl, Evidence for deep mantle circulation from global tomography, *Nature*, **386**, 578-84, 1997.
- Vasco, D.W. and L.R. Johnson, Whole Earth structure estimated from seismic arrival times, *J. Geophys. Res.*, **103**, 2633-71, 1998.
- Wahr, J. and D. de Vries, The possibility of lateral structure inside the core and its implications for nutation and Earth tide observations. *Geophys. J. Int.*, **99**, 511-19, 1989.
- Wilson, T.L., Neutrino tomography: Tevatron mapping versus the neutrino sky, *Nature*, **309**, 38-42, 1984.
- Woodhouse, J.H. The joint inversion of seismic wave forms for lateral variations in Earth structure and earthquake source parameters. IN: Proceedings of the International School of Physics 'Enrico Fermi'. Course LXXXV, H. Kanamori and E. Boschi, eds., North-Holland, Netherlands, p. 366-97, 1983.
- Woodhouse, J.H., The coupling and attenuation of nearly resonant multiplets in the Earth's free oscillation spectrum, *Geophys. J. R. Astr. Soc.*, **61**, 261-83, 1980.
- Woodhouse, J.H. and F.A. Dahlen, The effect of a general aspherical perturbation on the free oscillations of the Earth, *Geophys. J. R. Astr. Soc.*, **53**, 335-54, 1978.
- Woodhouse, J.H. and A.M. Dziewonski, Mapping the upper mantle: three-

dimensional modeling of Earth structure by inversion of seismic waveforms, *J. Geophys. Res.*, **89**, 5953-86, 1984.

Woodhouse, J.H., D. Giardini, and X.-D. Li, Evidence for inner core anisotropy from free oscillations, *Geophys. Res. Lett.*, **13**, 1549-52, 1986.

Woodhouse, J.H. and T.P. Girnius, Surface waves and free oscillations in a regionalized Earth model, *Geophys. J. R. Astr. Soc.*, **68**, 653-73, 1982.